Optimization of fast charging method based on a reduced order electrochemical model for lithium ion batteries

by

Yilin Yin

A dissertation submitted to the Graduate Faculty of
Auburn University
in partial fulfillment of the
requirements for the Degree of
Doctor of Philosophy

Auburn, Alabama
May 14, 2020

Key words: Lithium ion batteries, Reduced order model, Side reaction, Lithium plating, Lithium stripping, Optimal fast charging.

Copyright 2020 by Yilin Yin

Approved by

Song-Yul Choe, Chair, Professor of Mechanical Engineering
Jeffrey Fergus, Professor of Materials Engineering
Roy Knight, Professor of Mechanical Engineering
John Hung, Professor of Electrical Engineering

Abstract

Long charging time is one of the technical barriers that should be overcvome for wide acceptance of electric vehicles (EVs) in the market. The charging time can be simply reduced using increased charging current that adversely reduces lifespan and deteriorates safety of batteries. Therefore, design of an appropriate charging protocol is a challenging issue.

I propose a fast charging method designed based on a reduced order electrochemical model (ROM) considering degradation effects predominantly caused by side reaction. Different charging protocols were generated by considering different limiting factors such as surface ion concentrations, state of charge, cutoff voltage, and side reaction rate, which were tested in real time using a Battery-In-the-Loop (BIL) system. Experimental results have shown that the proposed charging method considering the limitations of side reaction rate and ion concentration yields the best performances among others, where the charging time is reduced more than 40% compared with normal charging method while the degradation is comparable.

On the other hand, lithium plating is another cause for degradation, specifically in the working conditions of high charging currents and low temperatures, which is considered for design of an optimal charging method. Since the model is strongly nonlinear, a nonlinear model predictive control (NMPC) was employed to optimize the charging protocols. The objectives are to reduce charging time and at the same time minimize degradation speed. The charging time and degradation speed are traded off and optimized by varying the weighting factors. In addition, the charging protocol is constructed with not only constant currents, but also pulse discharging currents that promotes lithium stripping, so lithium ions can be recovered out of the plated lithium.

Firstly, the proposed protocol was determined at a constant temperature and implemented into a real time capable BIL test station and compared with constant current constant voltage (CC/CV) charging method. Experimental results have shown that the proposed charging method significantly reduces the charging time while the cycle life is extended. Then, the effects of varying temperature on side reaction and lithium plating were considered in the optimal design of charging method. In fact, the side reaction and lithium plating rates are strongly affected by C-rates and temperatures, which is numerically analyzed using the validated degradation model. This analysis allows for determination of optimal temperatures with the longest cycling life at different C-rates. The last method was verified in the BIL system, where the temperature was controlled by a designed thermostat system to track the optimal temperatures. The experimental results have shown that the designed protocol can further reduce the capacity fade while the charging time can be kept.

Acknowledgments

I would like to express my deep appreciation to my advisor, Dr. Song-Yul Choe, for giving me the research opportunity. With his assistance and generous guidance, I can finish my study. Without his valuable suggestions and detailed corrections to my papers and dissertation, I would hardly finish my research program. I would also like to acknowledge my committee members, Dr. Roy Knight, Dr. John Hung and Dr. Jeffrey Fergus, for their continuous instructions and encouragement, which enabled me to develop a deep understanding in the research area.

Sincere thanks to my colleagues for their assistance in my research work.

Last but not least, I would like to express my gratitude to my parents, elder brother, parents in law, for their unselfish support of my academic endeavor. Special thanks to my dear wife, Dr. Guyu Qin, for her love, support and encouragement.

Table of Contents

List of Tables

List of Figures

List of symbols

A	sandwich area of the cell (cm^2)
a_s	specific surface area of electrode (cm^{-1})
c	ion concentration (mol L^{-1})
$C_{ionloss}$	amount of ion loss caused by the side reaction (A h)
D	diffusion coefficient in electrode (cm^2 s^{-1})
F	Faraday constant (96,487 C mol^{-1})
I	current of the cell (A)
i_0	exchange current density (A cm^{-2})
j	reaction rate (A cm^{-3})
L	thickness of micro cell (cm)
l	coordinate along the thickness of micro cell
Q	capacity of the cell (A h)
R	resistance (Ω cm^2) or universal gas constant (8.3143 J mol^{-1} K^{-1})
R_s	radius of spherical electrode particle (cm)
r	coordinate along the radius of electrode particle (cm)
T	cell temperature (K)
t	time (s)
U_{eq}	equilibrium potential (V)
V_t	terminal voltage of cell (V)
x	stoichiometric number of the anode
y	stoichiometric number of the cathode

Greek symbols

α	transfer coefficient of reaction
δ	thickness (mm)
ε	volume fraction of a porous medium or strain
φ	electric potential (V)

η	surface overpotential of electrode reaction (V)
κ	ionic conductivity (S cm^{-1})
σ	conductivity (S cm^{-1})
τ	total time (s)

Subscripts and Superscripts

a	anodic
aged	aged cell
ave	average value
c	cathodic
e	electrolyte phase
eff	effective
eq	equilibrium
fresh	fresh cell
ion loss	caused by loss of lithium ion
Li	lithium ion
max	maximum
s	solid phase
side	the side reaction
surf	electrode particle surface
-	negative electrode (anode)
+	positive electrode (cathode)

List of Abbreviations

BIL	Battery-In-the-Loop
BOL	Beginning of life
B-V	Bulter-Volmer
CC	Constant Current
CV	Constant Voltage
CP	Constant Power
EC	Ethylene Carbonate
EECM	Electric Equivalent Circuit Model
EIS	Electrochemical Impedance Spectroscopy
EKF	Extended Kalman Filter
EV	Electric Vehicle
FC	Fast Charging
FOM	Full Order Model
LCO	Lithium Cobalt Oxide
LFP	Lithium Iron Phosphate
LiB	Lithium ion battery
LP	Lithium plating
NMPC	Nonlinear Model Predictive Control
NMC	Nickel Manganese Cobalt
OCV	Open Circuit Voltage

OFCPD	Optimal Fast Charging with Pulse Discharging Current
OFC-T	Optimal fast charging under varying temperatures
P2D	Pseudo two dimensions
PDE	Partial Differential equation
ROM	Reduced Order Model
SOC	State of Charge
SEI	Solid Electrolyte Interphase
SPKF	Sigma-Point Kalman Filter
SPM	Single Particle Model
SQP	Sequential Quadratic Programming
SR	Side Reaction
TEM	Thermal electric module

Chapter 1 Introduction

1.1 Background

Electric vehicles (EVs) are increasingly attractive due to their increased range, lower battery costs and government subsidies. In 2018, the sales of EVs in United States of America is 361307, which is up 81% over 2017 [1]. It is anticipated again that EVs, including hybrid, all-electric, and plug-in hybrid EVs reach a highest record in sales.

The most important component of the EVs is the battery, which should satisfy requirements such as balance between energy and power, thermal and mechanical specifications, and manufacturing costs, etc. Currently, lithium ion batteries (LiBs) are among the most promising energy storage devices used for EVs because of their high power and energy density. The battery can be manufactured into different types dependent upon ways of packaging, which include cylindrical, coin, prismatic and pouch type, as shown in Figure 1. Compared to the other three types of cell packaging, the pouch cells have high efficiency in the use of space and packaging and also eliminate the metal enclosure in order to increase the energy density. By folding electrodes, electrolytes, and separators together, the pouch cells are the most preferred in new applications such as EVs that require high power and energy density.

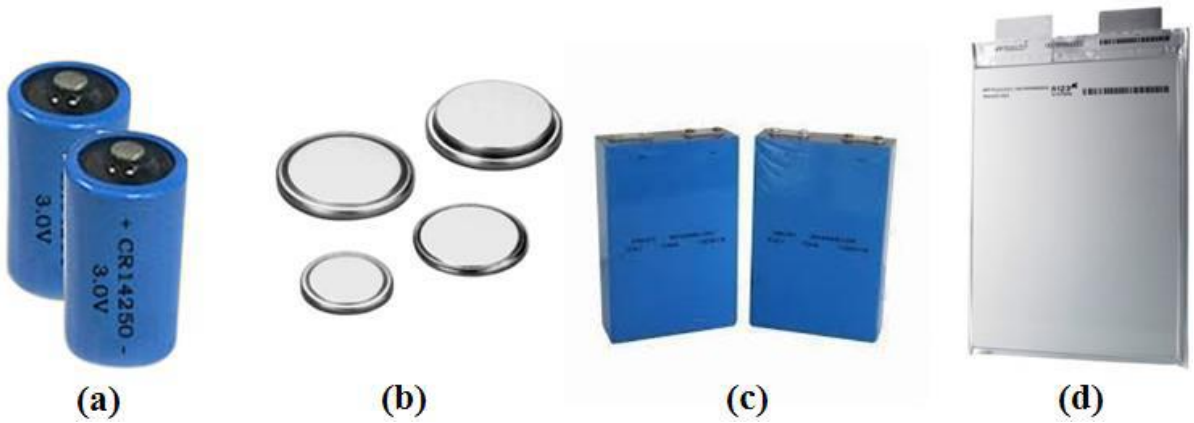

Figure 1. Ways of packaging: (a) cylindrical; (b) coin; (c) prismatic and (d) pouch [2].

A pouch-type lithium ion battery (LiB) is made of stacked microcells that are connected in parallel by current collectors. The microcell has a sandwich structure in the thickness direction that is composed of composite electrodes and a separator in between. In order to have a large reaction area, the electrodes in LiB are made porous, which allows the electrolyte to soak into them. So, the composite electrodes are made of active materials, electrolytes and binders. A schematic diagram for this cell is shown in Figure 2, where the active material on the anode is graphite and that on the cathode is metal oxides. When discharging or charging cells, lithium ions deintercalate, diffuse in the electrode particles, and then transporte through the electrolyte and the separator. Then they chemically reacte with electrons and active materials at the interface of the electrode particles, then diffuse and intercalate into the particles. The electrons flow through an external circuit and complete the redox process.

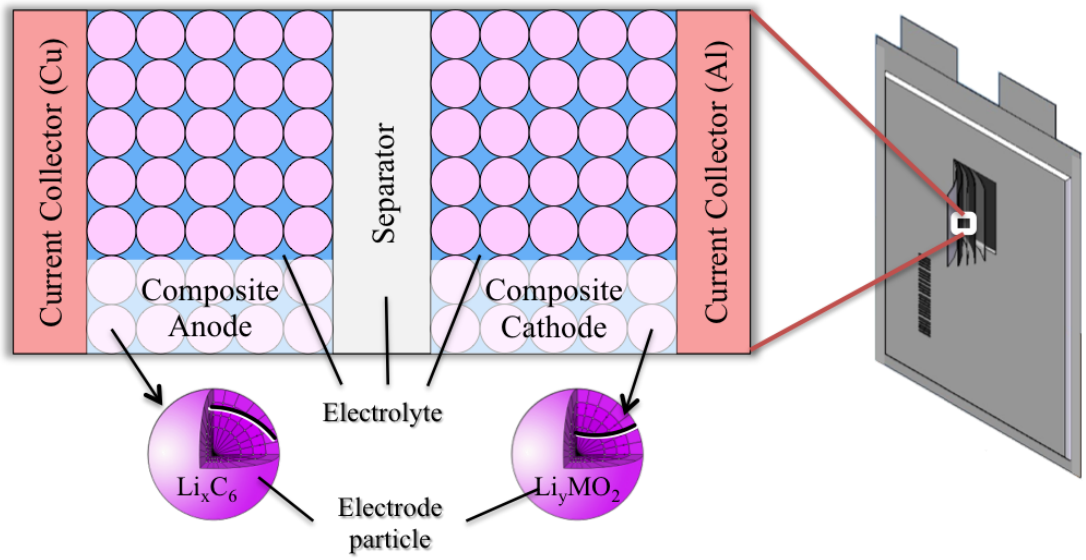

Figure 2. Schematic diagram of a microcell and a single cell [3].

In recent years, the most commonly used material for negative electrode is carbon, which has the combined properties of low cost, abundant availability, high diffusivity, high electrical conductivity and low volume change during intercalation/deintercalations [4]. The most common materials for positive electrode are lithium cobalt oxide (LCO), lithium manganese oxide (LMO), nickel manganese cobalt oxide (NMC), nickel cobalt aluminum oxide (NCA), lithium cobalt phosphate (LCP), lithium iron phosphate (LFP), lithium iron fluorosulfate (LFSF) and lithium titanium sulfide (LTS) [4]. LCO is a very attractive cathode material because of its relatively high theoretical specific and volumetric capacity, low self-discharge, high discharge voltage, and good cycling performance [5]. The major limitations of LCO are high cost, low thermal stability, and fast capacity fade at high charging currents or during deep cycling [6]. LMO can also be promising because Mn is much cheaper and less toxic than Co and Ni. However, the cycling performance of LMO is still not satisfactory [7]. NCA is widely used in Panasonic batteries for Tesla EVs because of high usable discharge capacity and long storage calendar life, but capacity fade is severe at

elevated temperatures due to side reaction and micro-crack at the grain boundaries [8]. LFP has good thermal stability and high power capability. The major weakness of LFP cathode is relatively low average potential and low electrical and ionic conductivity [9]. NMC could be attractive material because of enhanced structure stability, higher achievable specific capacity and lower cost. The cost is reduced by using lower cost transition metals (Co). The presence of Ni allows higher Li extraction capacity to be achieved without structure deterioration and the presence of Mn and Co for better cycle life and safety [10].

In the active materials, there is an intrinsic equilibrium potential against electrolyte that is a function of stoichiometric number determined by the ratio between the current and maximum lithium ion concentration in the electrode. At the equilibrium state, no macroscopic current flows across the surface of particles and the potential difference between the electrode and electrolyte is equal to the equilibrium potential. The difference between the equilibrium potentials of cathode and anode is same as the open circuit voltage (OCV).

The state of charge (SOC) of a battery is defined as a ratio between the total number of ions present in the particles and that of the maximum acceptable ions, where the number of ions at any instant can be calculated based on average concentration. At 100% SOC, the ion concentration in the anode is the highest while that in the cathode is the lowest. At 0% SOC, the ion concentration is reversed as shown in Figure 3 [11]. Changing of SOC implies moving around the lithium ions between the anode and cathode.

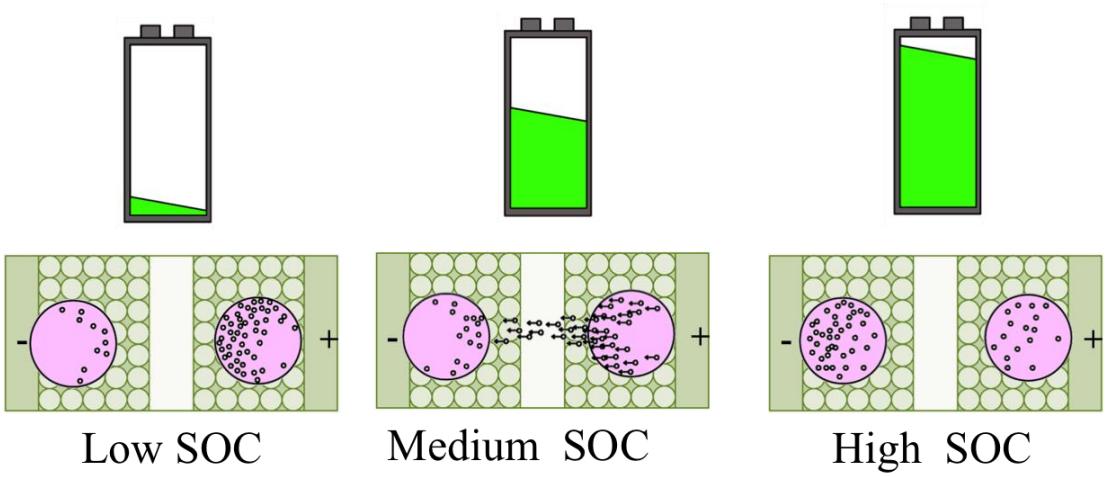

Figure 3. SOC and lithium ion concentration in solid phase [11].

The battery is charged from different power sources such as an AC grid or electric motors driven by an engine or in regenerative mode. Currently, there are two technical barriers to be overcome for rapid and wide acceptance of EVs in markets. These are a relatively short driving range and a long charging time. The driving range can be extended by installation of more batteries, but this adversely leads to an increase of charging time.

There have been several attempts to reduce the charging time with high power chargers such as DC fast charging (50kW), a supercharger (140kW), or extreme fast charging (350kW) [12]. The resulting increased charging current accelerates degradation, which significantly reduces the lifespan of batteries. Thus, the challenging issues of developing a fast charging (FC) method are not only to reduce the charging time but also to keep the degradation rate as low as possible.

1.2 Motivation and objectives

Usually, the battery is charged using constant current constant voltage (CC/CV) charging method, in which the current is limited by the cutoff voltage. The charging time can be reduced by increasing the charging C-rates. However, CC/CV charging method does not consider the degradation effects based on fundamental mechanisms, which presents a barrier to optimize the charging protocol to minimize charging time and degradation. Therefore, it is crucial to find an optimal FC method considering the fundamental mechanisms of ion transport, chemical reactions, intercalation process and degradation.

The objective for my dissertation is to propose a new FC method with several objective functions that include minimization of the charging time and degradation. The ROM, degradation model will be used to estimate the internal states of battery and the change of battery parameters, respectively. Side reaction and lithium plating, which are the two major causes of degradation of battery, are considered and suppressed using different methods in the design of FC protocols.

1.3 Dissertation structure

The basic structure of the dissertation is shown as follows.

1. Introduction

   This chapter introduces the research background, motivation and objectives.

2. New fast method for beginning of life (BOL) considering side reaction.

   This chapter introduces the first designed FC method at constant temperature in order to minimize degradation rate and reduce charging time simultaneously, which

considers different limiting factors such as surface ion concentrations, state of charge, cutoff voltage, and side reaction rate.

3. Optimal FC method considering side reaction and lithium plating at a constant temperature.

   This chapter introduces the second designed online FC method using the technique of optimal control, which considers side reaction and lithium plating at a constant temperature.

4. Optimal FC method considering side reaction and lithium plating at varying temperatures.

   This chapter introduces the third designed online FC method using the technique of optimal control, which considers the effects of temperature on the side reaction and lithium plating.

5. Conclusion and future work

   This chapter summaries the designed charging method and their charging performances. The future work will include the further optimization of charging methods considering the battery pack with heating and cooling function. In addition. the mechanisms between the frequecncy and amplitude of pulse discharging current and the associated lithium stripping should be explored.

Chapter 2 New FC method for beginning of life considering side reaction

2.1 Literature review

2.1.1 Review of charging methods

Design of charging methods for LiBs should consider various operation aspects given in the battery specification such as capacity, cutoff voltage, maximum temperature, and maximum charging current.

There are three basic charging methods: constant current (CC), constant power (CP) and constant voltage (CV). The CC charging method uses a constant current, which enables reduction of the charging time, but might overcharge a battery even using a small current. When charged with CP, the current at the beginning is relatively high, which can reduce the charging time, but also cause overcharging. The CV charging can prevent a battery from overcharging but has a substantially lower charging rate on average. Like CC charging, the charging current at a low SOC becomes high, which induces a high temperature rise and a high degradation rate. Combinations of CC with CV or CP with CV charging prevent the overcharging, temperature rise, and high degradation rate, resulting in a constant current constant voltage (CC/CV) charging method or constant power constant voltage (CP/CV) charging method [13]. Both charging methods use CC or CP to charge the battery until a cutoff voltage is reached and then use CV mode to fully charge it. In fact, charging currents in the CP/CV method at low SOC is higher than that in the CC/CV method due to the spike in charging current. Therefore, the CC/CV charging method is widely preferred because it prevents the overcharging and limitation of the high charging current at the beginning, which assures safe operation and a lower degradation rate [14].

There are many suggestions for optimization of the CC/CV charging method with respect to the charging time, degradation, heat generation, safety, use of electric equivalent circuit models (EECM), or electrochemical models. The EECM is used to estimate SOC, impedances, and heat generation. The estimated SOC is used to determine the proper transition time from CC to CV mode, which can reduce the total charging time due to the extension of the CC mode [14]. Additionally, in different SOC ranges, different charging C-rates are used to charge the battery, which reduces the charging time while maintaining the degradation speed [15][16]. The inaccuracy of estimated SOC caused by hysteresis can be corrected by restricting the hysteresis [17]. The temperature rise induced by high charging currents is limited by combining a thermal model with the EECM to limit the high degradation rate [18][19].

These charging methods enable reduction of the charging time but do not consider the degradation effects from fundamental mechanisms. As a matter of fact, the EECM does not describe the internal mechanisms taking place during the charging processes such as ion transport, electrochemical reaction, intercalation/deintercalation, and ion diffusion. As a result, it is impossible to perfectly optimize the charging currents while minimizing the aging speed. The internal processes of a battery can be accurately described using electrochemical principles [20].

A large format pouch-type LiB with multiple layers is simplified to a microcell under assumptions that there are no thermal and ion gradients in lateral direction and that the current collectors on each layer have the same potential. The microcell is a sandwich structure that consists of a current collector, a composite anode and cathode, and a separator. It is assumed that electrodes are composed of spherical particles with the same radius, which are in contact with each other. Ions are transported through the plane and are diffused in these particles. The model considering this structure is called a “full order model with pseudo-two-dimensions” or “FOM-P2D”. The

FOM-P2D can estimate SOC and anode potentials, which are used in the design of FC methods to reduce the charging currents and prevent lithium plating [21]. However, side reaction that represents the main cause of degradation are not considered. In addition, FOM-P2D is inadequate for FC due to the high computational time caused by complex governing equations. When the partial differential equations and nonlinear equations of the FOM-P2D are simplified to ordinary differential equations and linearized to linear equations, the FOM-P2D becomes a reduced order model (ROM-P2D) that can be better embedded in controllers like battery management systems [3][22]. If both electrodes are assumed to be composed of spherical particles of the same size, and current distribution is assumed to be uniform in both electrodes, all of the particles in both electrodes can be replaced with a single spherical particle, which is called "single particle reduced order model" or "ROM-SP" [23]. In order to maximize battery life while reducing charging time, ROM-SP was used where the charging current profile was optimized by considering limitations of SOC, terminal voltage, anode potential, and temperature [24]. The optimization was solved using a genetic algorithm as a function of cycle number. Similarly, SOC and anode potential derived from ROM-SP were used to prevent lithium plating at a high charging rate [25]. However, side reaction was not considered.

Even though calculation of ROM-SP is faster than that of ROM-P2D, the ROM-P2D has several advantages in accuracy and particularly in the calculation of the gradient of ion concentration in solid and current distributions. Some researchers suggest using the ROM-P2D to optimize a charging method by considering SOC, surface ion concentration, and temperature rise. Because of the limited temperature rise, battery life is extended [26]. Other researchers suggest limiting anode potential to prevent the formation of lithium plating [27]. However, these

researchers did not consider the side reaction dependent upon operating conditions such as SOC, anode potential and lithium ion concentration.

2.1.2 Effects of charging methods on side reaction

Charging time can be reduced simply by increasing the charging current. However, an increased charging current not only generates more heat but also accelerates the aging of the battery.

According to investigations on degradation mechanisms conducted with a large format lithium ion polymer battery with NMC/Carbon or LFP/Carbon chemistries, lithium plating and side reaction at the surface of the anode graphite particles are the two major causes for degradation [28][29].

Lithium plating, also known as lithium deposition reaction, is one of causes for degradation and predominantly occurs under extreme charging conditions, such as high currents[30], low temperatures[31], and overcharging[32]. For the cells with high power density, lithium plating is not a serious issue at high temperatures [33]. Since the charging current rate was less than 5C and the operating temperatrue was 25^{o}C, effects of lithium plating are not considered for the cells with high power density, which might cause some discrepancies in the capacity fade.

Side reaction is a reduction process between electrolyte solvent and lithium ions at the anode particle surface. The products of side reaction can form a very thin film that adheres to the surface of the anode particles, which is called a solid electrolyte interphase (SEI) layer. The side reaction takes place continuously throughout the battery life because the anode always operates at the potential that is outside the stability window of the electrolyte component; however, as the SEI

layer forms, the side reaction begins to slow down [34]. These deposits accumulate on the surface of anode particles and result in a continuous growth of the SEI layer. The layer at the particles located near the separator grows faster than other particles and forms an extra deposit layer [27]. As a result, the ionic resistance of the layers increases, and the accessible surface area and porosity decrease, with power fade being the result. SEI layers are electronic isolators that can completely isolate some particles from electrons if these particles are fully covered by SEI layers, which leads to a loss of active carbon material, finally resulting in capacity fade. In addition to the active carbon material loss, the consumed ions and electrolyte solvents caused by the side reaction are additional factors for capacity fade.

Side reaction is accelerated by operating conditions such as elevated temperatures and high SOC ranges. A high charging current also promotes the side reaction, which is analyzed later. When the temperature rises, the kinetics of lithium ions and electrolyte solvents are increased, resulting in more ions passing through the SEI layer to the interface [34]. Thus, the concentrations of both ions and solvents on the particles' surface increase, which results in a higher side reaction rate.

The effects of SOC ranges and charging C-rates on the side reaction can be better explained with help of the relationship of potentials at the interface between the anode electrode and the electrolyte. A schematic diagram of the potential relationship at the anode side during charging is depicted in Figure 1. At charging, two chemical reactions take place, the main and side reaction, with the total reaction rate, j_{total}^{Li}, expressed as a sum of both reaction rates

$$j_{total}^{Li} = j_{-}^{Li} + j_{side}^{Li}, \tag{1}$$

where j_{-}^{Li} and j_{side}^{Li} denote the reaction rates caused by the main and side reaction, respectively.

The reaction rate, j_{-}^{Li}, produced by the reaction at the interface between anode and electrolyte is a function of overpotential, denoted η_{-} and expressed by the Bulter-Volmer (B-V) equation

$$j_{-}^{Li} = a_s i_0 \left(\exp\left(\frac{\alpha_a nF}{RT} \eta_{-} \right) - \exp\left(-\frac{\alpha_c nF}{RT} \eta_{-} \right) \right), \tag{2}$$

where a_s is the specific reaction area; α_a and α_c are the anodic and cathodic transfer coefficient, which are both assumed to be 0.5; *n* is the number of ions participating in the main reaction, which is equal to 1; *R* is the universal gas constant (8.3143 J mol^{-1} K^{-1}); i_0 is the exchange current density; and *T* is the cell temperature. *F* is the Faraday constant (96487 C mol^{-1}).

The overpotential in the B-V equation above can be expressed as follows:

$$\eta_{-} = \varphi_{s-} - \varphi_{e-} - U_{eq-} - \frac{R_{SEI}}{a_s} j_{total}^{Li}, \tag{3}$$

where φ_{s-} and φ_{e-} are the electric potentials of the solid anode particle and electrolyte, respectively.

The equilibrium potential of the anode, U_{eq-}, is a function of the stoichiometric number that is the ratio between ion concentration in its solid phase and its maximum value. Here, R_{SEI} is the resistance of SEI that causes a potential drop across the SEI:

$$V_{SEI} = \frac{R_{SEI}}{a_s} j_{total}^{Li}. \tag{4}$$

The rate of side reaction, j_{side}^{Li}, is also calculated using the B-V equation:

$$j_{side}^{Li} = -i_{0,side} a_s \exp\left(-\frac{\alpha_{c,side} n_{side} F}{RT} \eta_{side} \right), \quad (5)$$

where n_{side} is the number of ions involved in the side reaction that is equal to 2. η_{side} is the overpotential of side reaction:

$$\eta_{side} = \phi_{s-} - \phi_{e-} - U_{eq,side} - \frac{R_{SEI}}{a_s} j_{total}^{Li}, \quad (6)$$

where $U_{eq,side}$ is the equilibrium potential of the side reaction, 0.4V [35][36][37][38]. The exchange current density of the side reaction, $i_{0,side}$ is a function of two reactants of the side reaction, lithium ions, and EC molecules [39][40]:

$$i_{0,side} = k_{side} \sqrt{c_{s,surf} c_{EC,R_s}}, \quad (7)$$

where k_{side} is the kinetic rate constant for the side reaction. $c_{s,surf}$ and c_{EC,R_s} are the concentrations of the lithium ions and the EC molecules at the surface of anode particles, respectively.

Electrolye potential, φ_{e-}, is regarded as the reference to analyze the relationship to other potentials. While the battery is charging, the overpotential, η_-, is negative because of the negative j_-^{Li} induced by ion transport from the electrolyte to the anode.

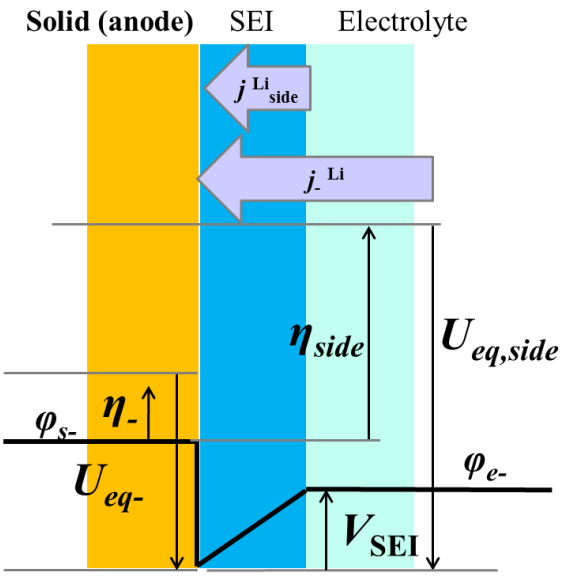

Figure 4. Schematic diagram of potential relationship at the anode side during charging [2].

When SOC is high, the ion concentration in the anode is high and the equilibrium potential, U_{eq-}, becomes small, then φ_{s-} also becomes small under the assumption that the overpotential, η_-, is constant. As shown in Figure 4, the overpotential for side reaction, η_{side}, decreases, which increases the magnitude of the side reaction rate. Consequently, charging a cell in a high SOC range leads to a high rate of side reaction, which eventually accelerates degradation.

When a high C-rate is used to charge, the magnitude of the overpotential, η_-, increases according to the B-V equation, which lowers the anode potential, φ_{s-}. Since the overpotential for side reaction, η_{side}, is the difference between the anode potential and equilibrium potential, the magnitude of the overpotential for the side reaction increases, which leads to a high side reaction rate.

2.2 Design of a FC method

Design of a FC method takes into account three parts: 1) development of a model that allows for estimation of physical variables such as the ion concentrations and anode potentials in real time and reduction of estimation errors caused by model state error and measurement noises; 2) analysis of the effects of CC/CV charging method on charging time and degradation speed; 3) determination of the magnitude of current rate and duration of pulses considering ion concentration, cutoff voltage, and side reaction rate.

2.2.1 ROM with EKF

The intercalation or deintercalation, diffusion, ion transport, chemical reactions, and the resulting change of potentials are described by a set of coupled nonlinear and partial differential equations (PDEs). Four variables of the governing equations can be solved numerically, which is called a full order model (FOM) listed in Table 1. The variables are the ion concentrations and potentials in both the electrodes and the electrolyte. Since the FOM is very computationally intensive[3], it is inappropriate for use in control purposes, and as such the nonlinearity of equations and the PDE are simplified by linearization and mathematical treatments respectively to a ROM. This ROM, which consists of linear ordinary differential equations (ODEs), can be derived as listed in Table 1. The major mathematical simplifications are carried out for ion concentrations in electrodes and the electrolyte by a polynomial equation and grouped eigenvalues in the state space domain respectively. In addition, if ion concentration in the electrolyte does not significantly affect the reaction current, the equation of phase potential can be also simplified because the second term becomes zero. Furthermore, the nonlinear characteristic of the B-V equation is

approximated by a linear equation. The detailed description of the model reduction approaches can be found in [3][22]. The model parameters used for the ROM are listed in Table 2.

Table 1. Summary of FOM and ROM.

Cell dynamics	FOM	ROM
Ion concentration in electrode	$\frac{\partial c_s}{\partial t}=\frac{D_s}{r^2}\frac{\partial}{\partial r}\left(r^2\frac{\partial c_s}{\partial r}\right)$ $\frac{1}{r}\frac{\partial c_s}{\partial r}\Big\vert_{r=0}=0 \ \ and \ \ D_s\frac{\partial c_s}{\partial r}\Big\vert_{r=R_s}=\frac{-j^{Li}}{a_sF}$	$\frac{d}{dt}c_{s,ave}+3\frac{j^{Li}}{R_s a_s F}=0$ $\frac{d}{dt}q_{ave}+30\frac{D_s}{R_s^2}q_{ave}+\frac{45}{2}\frac{j^{Li}}{R_s^2 a_s F}=0$ $35\frac{D_s}{R_s}\left(c_{s,surf}-c_{s,ave}\right)-8D_s q_{ave}=-\frac{j^{Li}}{a_sF}$
Ion concentration in electrolyte	$\frac{\partial(\varepsilon_e c_e)}{\partial t}=\frac{\partial}{\partial x}\left(D_e^{eff}\frac{\partial}{\partial x}c_e\right)+\frac{1-t_+^0}{F}j^{Li}$ $\frac{\partial c_e}{\partial x}\Big\vert_{x=0}=\frac{\partial c_e}{\partial x}\Big\vert_{x=L}=0$	$\dot{\mathbf{c}}_\mathbf{e}=\mathbf{A}^*\cdot\mathbf{c}_\mathbf{e}+\mathbf{B}^*\cdot I$ $\mathrm{y}=\mathbf{C}^*\cdot\mathbf{c}_\mathbf{e}+\mathbf{D}^*\cdot I$
Ohm's law in electrode	$\frac{\partial}{\partial x}\left(\sigma^{eff}\frac{\partial}{\partial x}\varphi_s\right)-j^{Li}=0$ $-\sigma^{eff}\frac{\partial}{\partial x}\varphi_s\Big\vert_{x=0}=-\sigma^{eff}\frac{\partial}{\partial x}\varphi_s\Big\vert_{x=L}=\frac{I}{A}$ $\frac{\partial}{\partial x}\varphi_s\Big\vert_{x=\delta_-}=\frac{\partial}{\partial x}\varphi_s\Big\vert_{x=\delta_-+\delta_{sep}}=0$	$\frac{\partial}{\partial x}\left(\frac{\partial}{\partial x}\varphi_s\right)=\frac{j^{Li}}{\sigma^{eff}}$ $-\sigma^{eff}\frac{\partial}{\partial x}\varphi_s\Big\vert_{x=0}=-\sigma^{eff}\frac{\partial}{\partial x}\varphi_s\Big\vert_{x=L}=\frac{I}{A}$ $\frac{\partial}{\partial x}\varphi_s\Big\vert_{x=\delta_-}=\frac{\partial}{\partial x}\varphi_s\Big\vert_{x=\delta_-+\delta_{sep}}=0$
Ohm's law in electrolyte	$\frac{\partial}{\partial x}\left(\kappa^{eff}\frac{\partial}{\partial x}\varphi_e\right)+\frac{\partial}{\partial x}\left(\kappa_D^{eff}\frac{\partial}{\partial x}\ln c_e\right)+j^{Li}=0$ $\frac{\partial}{\partial x}\varphi_e\Big\vert_{x=0}=\frac{\partial}{\partial x}\varphi_e\Big\vert_{x=L}=0$	$\frac{\partial}{\partial x}\left(\frac{\partial}{\partial x}\varphi_e\right)+\frac{j^{Li}}{\kappa^{eff}}=0$ $\frac{\partial}{\partial x}\varphi_e\Big\vert_{x=0}=\frac{\partial}{\partial x}\varphi_e\Big\vert_{x=L}=0$
Electrochemical kinetics	$j^{Li}=a_s i_0\left\{\exp\left[\frac{\alpha_a nF}{RT}\eta\right]-\exp\left[-\frac{\alpha_c nF}{RT}\eta\right]\right\}$	$j^{Li}=a_s i_0\frac{n(\alpha_a+\alpha_c)F}{RT}\eta$
SOC	$SOC=\frac{1}{\delta_-}\int_0^{\delta_-}\frac{\left(c_{s,ave}-c_{s,\max}Stoi_{100}\right)}{c_{s,\max}\left(Stoi_{100}-Stoi_0\right)}dx$	

SOC is defined as a ratio between the total number of ions present in the particles and that of the maximum acceptable ions, where the number of ions at any instant can be calculated based on the average concentration. The dynamic error of the average ion concentration and resulting SOC error given by the initial values are further improved by an extra closed-loop method with an extended Kalman filter (EKF) [41][42]. The ROM predicts states and the EKF is used to correct the predicted states and, at the same time, measurement errors.

Since the charging current affects the side reaction rate, it can be limited to suppress the side reaction rate. The ROM-EKF estimates the main chemical reaction rate, j_{-}^{Li}, anode potential, φ_{s-} and electrolyte potential, φ_{e-}, which are used to estimate the side reaction rate, j_{side}^{Li}, based on Equation (4), Equation (5) and Equation (6).

Table 2. Model parameters (a: manufacturers; b: tuning with the model; c: literature).

Category	Parameter	Negative electrode	Separator	Positive electrode	Source
Design specifications (geometry and volume fractions)	Thickness, δ (cm)	$50*10^{-4}$	$25.4*10^{-4}$	$36.4*10^{-4}$	a
	Particle radius, R_s (cm)	$1*10^{-4}$		$1*10^{-4}$	a
	Active material volume fraction, ε_s	0.58		0.5	a
	Polymer phase volume fraction, ε_p	0.048	0.5	0.11	a
	Conductive filler volume fraction, ε_f	0.04		0.06	a
	Porosity, ε_e	0.332	0.5	0.33	a
Lithium-ion concentration	Maximum solid phase concentration, $c_{s,\,max}$ (mol cm^{-3})	$16.1*10^{-3}$		$23.9*10^{-3}$	b
	Stoichiometry at 0% SOC: *Stoi*0	0.126		0.936	b
	Stoichiometry at 100% SOC: *Stoi*100	0.676		0.442	b
	Average electrolyte concentration, c_e (mol cm^{-3})	$1.2*10^{-3}$	$1.2*10^{-3}$	$1.2*10^{-3}$	a
Kinetic and transport properties	Exchange current density coefficient, k_{i0} (A cm^{-2})	12.9		6.28	c[43]
	Charge-transfer coefficient, α_a, α_c	0.5, 0.5		0.5, 0.5	c[22]
	Solid phase conductivity, σ (S cm^{-1})	1		0.1	c[22]
	Electrolyte phase Li^+ diffusion coefficient, D_e (cm^2 s^{-1})	$2.6*10^{-6}$	$2.6*10^{-6}$	$2.6*10^{-6}$	c[22]
	Solid phase Li^+ diffusion coefficient, $D_{s,0}$ (cm^2 s^{-1})	$3*10^{-12}$		$5.55*10^{-12}$	b

	Activation energy of D_s, $E_{a,D}$ (J mol^{-1})	$4.5*10^4$		$4.5*10^4$	b
	Film resistance of SEI layer, $R_{SEI,0}$(Ω cm^2)	1000			b
	Activation energy of R_{SEI}, $E_{a,R}$ (J mol^{-1})	$3.8*10^4$			b
	Bruggeman's porosity exponent, p	1.5	1.5	1.5	c[22]
	Electrolyte phase ionic conductivity, κ (S cm^{-1})	$15.8c_e*\exp(-13472c_e^{1.4})$			c[22]
	Li^+ transference number, t_+^0	0.363	0.363	0.363	c[22]
Equilibrium potential	Negative electrode (V)	$U_-(x) = 8.00229 + 5.0647x - 12.578x^{1/2} - 8.6322*10^{-4}x^{-1} + 2.1765*10^{-5}x^{3/2} - 0.46016*\exp(15*(0.06-x)) - 0.55364*\exp(-2.4326*(x-0.92))$ where $x = c_{s,surf}^- / c_{s,\max}^-$			c[22]
	Positive electrode (V)	The difference between OCV and the equilibrium potential of the negative electrode			
Side reaction	Equilibrium potential of side reaction, $U_{eq,\ side}$ (V)	0.4			c[39]
	Kinetic rate constant for side reaction, k_{side} (A cm mol^{-1})	$3.07*10^{-8}$			b
	Cathodic symmetric factor of side reaction, $\alpha_{c,side}$	0.7			c[33]

2.2.1.1 Validation of ROM-EKF

The battery used in this research is a pouch-type LiB with a capacity of 15.7Ah. The active material of the anode and cathode is carbon and NMC (Li[MnNiCo]O_2), respectively. ROM-EKF is validated against the experimental data at charging and discharging. The current rates are 1C, 2C, 3C, 4C, 5C, and 6C at 25^{o}C. Even at a high C-rate, the temperature is kept constant by a thermostat system designed in the laboratory that completely rejects the heat generated, so that the effects of the temperature on the charging and discharging characteristics are limited. Details on the thermostat system can be found in [44].

Simulated and experimental terminal voltages are plotted in Figure 5 and Figure 6 for comparison, where the starred and solid lines represent simulation and experimental data,

respectively. The results show that the terminal voltage of ROM is a fairly good match with those from experiments. Tracking performance of the EKF for the estimation of SOC is presented in two cases, with and without an initial SOC error, as shown in Figure 7 and Figure 8. If no initial error is present, the ROM-EKF can estimate the SOC with an absolute error that is less than 5%. Even with a 20% initial SOC error, the ROM-EKF can track the SOC within 100s, but with a little bit of overshoot that can be further optimized by proper selection of the error covariance matrices of the EKF.

The CC/CV charging method is the simplest and most widely used charging method. However, increasing the charging current alone cannot significantly reduce the charging time because of the extended duration of the CV charging. In addition, the increased charging current accelerates the degradation of the battery. Thus, before proposing a new charging method, effects of CC/CV charging on the charging time and degradation, specifically side reaction, are first analyzed.

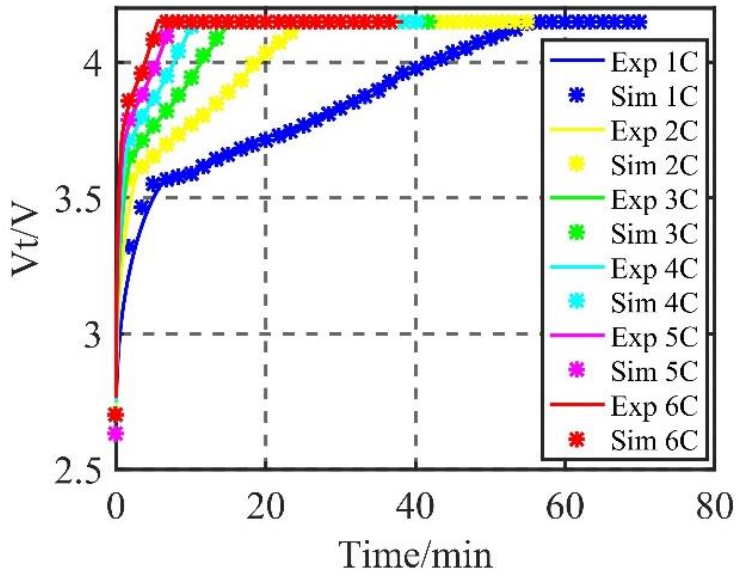

Figure 5. The simulated and experimental terminal voltages of charging at different current rates from 0-100% SOC.

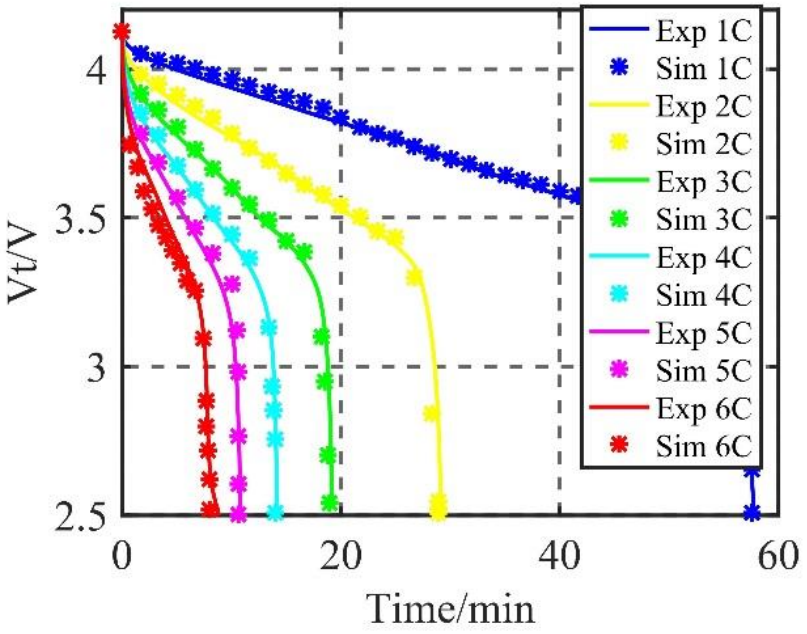

Figure 6. The simulated and experimental terminal voltages of discharging at different current rates from 100-0% SOC.

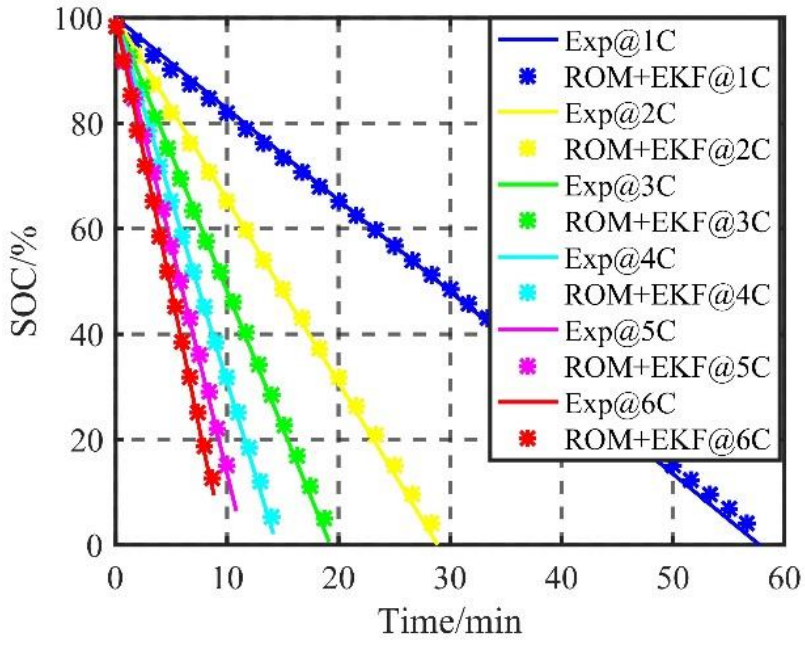

Figure 7. The simulated and experimental SOC without initial errors at different current rates.

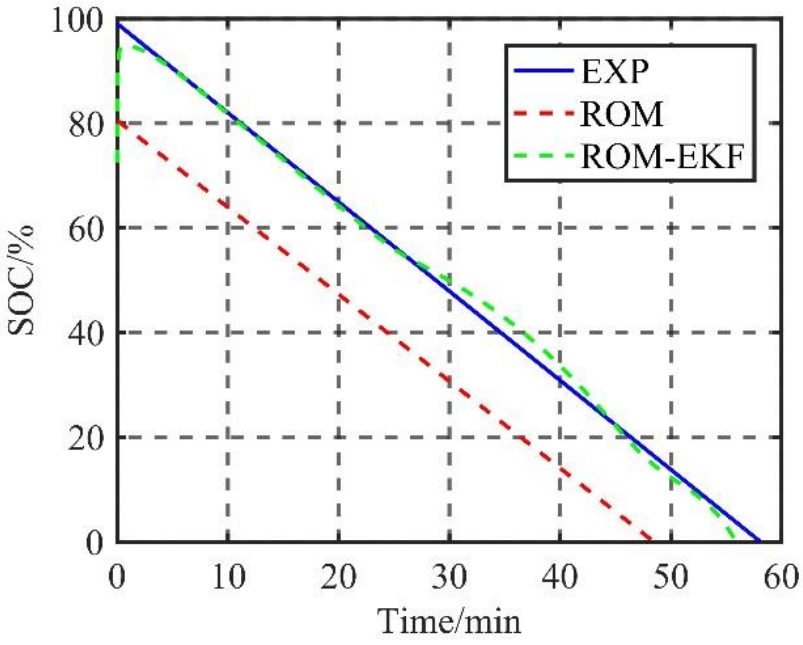

Figure 8. The simulated and experimental SOC with initial errors at different current rates.

2.2.2 Analysis of effects of CC/CV charging method on charging time

The charging time up to 100% SOC is determined by two factors: the C-rate applied during the CC range and the cutoff voltage during the CV range. Effects of C-rates on SOC and charging time in CC mode were studied experimentally using the pouch-type cell, as plotted in Figure 9 and Figure 10, where the cutoff voltage was set to be 4.15 V. As expected, a high charging C-rate reduces the charging time, but the terminal voltage reaches the cutoff voltage of 4.15V even at a lower SOC because of the high overpotential and the resulting limitation by the cutoff voltage. Thus, the maximum SOC to be charged at a given charging C-rate during CC mode is limited and their relationship is inversely proportional to the C-rate.

The effects of CC with the CV mode on charging time were also studied experimentally, where a cell is charged from 0% to 100% SOC. The C-rate was varied from 0.5 C to 7 C and the cutoff voltage was 4.15V. The charging time as a function of charging C-rates and the ratio between the charging time by CV and CC/CV are plotted in Figure 11 and Figure 12. If the C-rates are less than 1.5C, the charging time is significantly reduced even with a slight increase in the charging C-rate and is still reduced with C-rates between 1.5C and 4.5C, but no more, even with the higher C-rates. As shown in Figure 12, the ratio of charging time between CV and CC/CV increases as the charging C-rate is increased because the higher the charging current is, the larger the portion of the SOC in CV mode is. Consequently, the charging time in CV mode takes longer, which leads to a longer charging time.

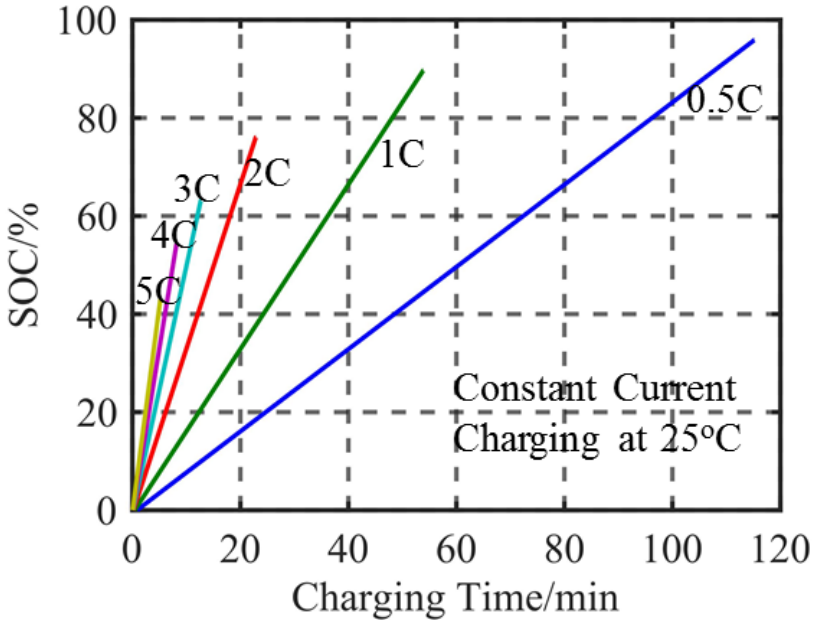

Figure 9. The SOC at different charging C-rates during CC charging (exp).

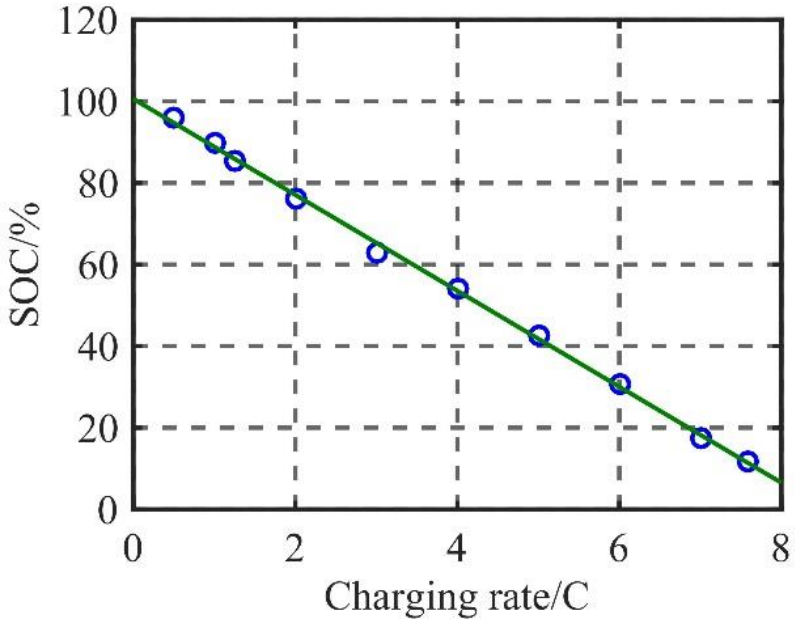

Figure 10. The SOC by end of CC charing at different charging C-rates (exp).

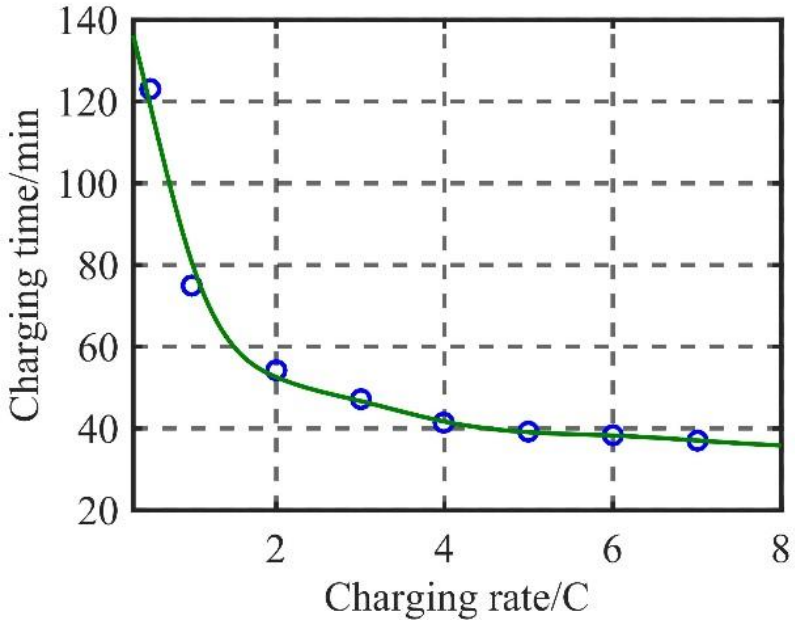

Figure 11. Charging time from 0% to 100% SOC at different charging C-rates (exp).

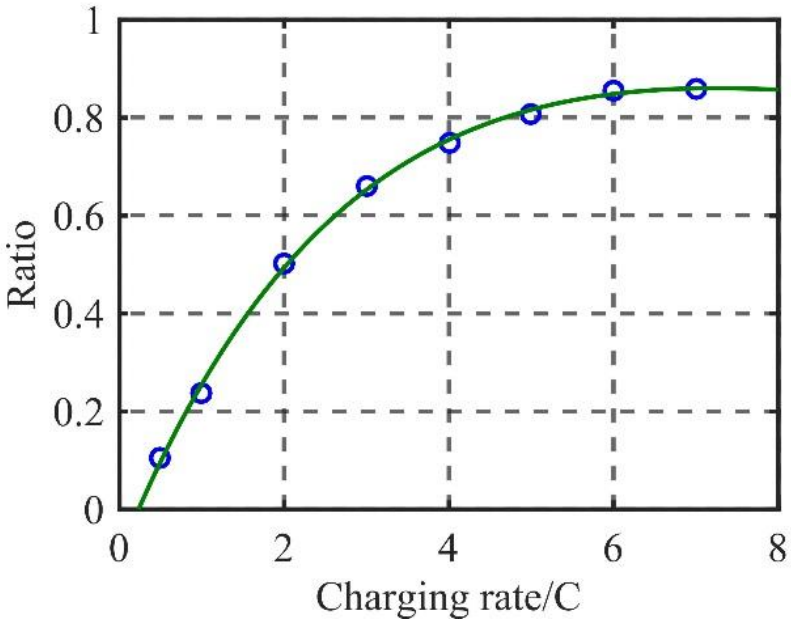

Figure 12. Ratio between CV and CC/CV charging time at different charging C-rates (exp).

2.2.3 Analysis of effects of CC/CV charging method on side reaction

Effects of CC/CV charging on side reaction are investigated, where SOC range and C-rates are varied. As discussed in the previous section, ion concentration heavily affects side reaction. The surface ion concentration of the solid particles is estimated by using the validated ROM as plotted in Figure 13, where the *x* axis represents the coordinate in the direction of through-plane of the anode. Each colored curve represents the surface ion concentration of different anode particles at a specific time. At the beginning of charging, the concentrations are uniformly distributed in the electrode (blue curve). As more ions are transported from the cathode, the ion concentration gradually forms a high gradient at different particles, reaches the maximum value after several minutes, and then becomes less and finally approaches zero around 2200 seconds.

The concentration at the interface between the composite anode and the separator at 301 seconds (end of CC charging) becomes higher than that at 2200s (end of CV charging).

The value of surface ion concentration of a particle is dependent upon the location of the particle due to the limitation of diffusion rate and the gradient of ions in the electrolyte of the composite anode. The closer the particle is to the separator, the higher the surface ion concentration.

The surface concentration of the particle adjacent to the separator in the time domain is plotted in Figure 14. There is an overshoot of the ion concentration during the transit until an equilibrium is reached, when the charging current is larger than 4C. The overshoot is decreased in the CV mode simply because of the decreased charging current. At the steady state when SOC reaches 100%, the concentration converges to a vicinity of a value, which implies that anode particles cannot accept more lithium ions and lithium-ion concentration reaches saturation. The concentration value is 0.035 mol/cm^3 at SOC=100%, which is chosen as the saturation concentration, c_s^*.

The high ion concentration caused by the overshoot leads to a low equilibrium potential, $U_{eq\text{-}}$, that increases the magnitude of activation overpotential for side reaction and consequently promotes the side reaction. In addition, the excessive ions also increase the exchange current density of side reaction, $i_{0,side}$, according to Eq. (7).

Actually, the side reaction rate is calculated using the B-V equation, as shown in Equation (5) . The amount of ion loss, q_{loss}^{SR}, that represents the ions consumed by the side reaction is the same as the integration of the side reaction rate, j_{side}^{Li}, over the volume of composite anode and time;

$$q_{loss}^{SR}(\tau) = \int_{x=0}^{\delta_-} \left(\int_{t=0}^{\tau} \left| j_{side}^{Li}(l,t) \right| dt \right) A dl \,, \tag{8}$$

where q_{loss}^{SR} has a unit of Ah, δ_- is then the thickness of the composite anode, τ is the total operating time, and A is the cross-section area of the cell [28].

Examining these equations, it becomes obvious that the side reaction rate is predominantly affected by the overpotential in the B-V equation, which is the function of the charging current and the range of SOC, as shown in Figure 15. In addition, the side reaction rate over time and the consumed ion loss versus SOC are plotted in Figure 16, Figure 17 and Figure 18. The magnitude of the overpotential increases with the increasing charging C-rate until the terminal voltage reaches the cutoff voltage and then decreases in the CV mode. Accordingly, the side reaction rate tends to follow the shape of the overpotential and the consumed ions calculated by Equation (8) increase faster at a higher C-rate. According to the calculation of the ion loss as a function of SOC shows, the ion loss is relatively negligible at a low SOC range, but increases as SOC increases.

When SOC is less than 40%, a high charging current increases the side reaction rate but reduces the charging time, the relationship between charging time and the side reaction rate being almost linear. Therefore, the contribution of the high charging current on degradation is not significant based on Equation (8) and Figure 18. In fact, the increased charging current at the low SOC range does not cause significantly more ion loss in comparison to other ranges but can contribute to a reduction of the charging time. This is only valid assuming a constant cell temperature as the side reaction rate becomes higher at an elevated temperature.

In the middle SOC range, the relationship between the charging time and overpotential of side reaction becomes nonlinear and the concentration overshoot appears, both of which accelerate the side reaction. Therefore, as the SOC increases, the relationship between charging time and the

side reaction rate becomes nonlinear and the magnitude of the slope increases with the increased charging C-rate. As a result, a high charging current largely accelerates the degradation, as shown in Figure 19.

In high SOC range, the side reaction rate is much lower than that of the middle SOC range because of the continuously reduced charging current in CV mode, but the charging time takes longer than in other SOC ranges. In addition, the equilibrium potential becomes lower because of the high ion concentration and then overpotential gets higher, which causes more ion loss, as shown in Figure 20. In this SOC range, the charging C-rate still has a significant effect on lithium-ion loss because of the longer charging time in a high SOC range and a higher side reaction rate caused by higher ion concentration.

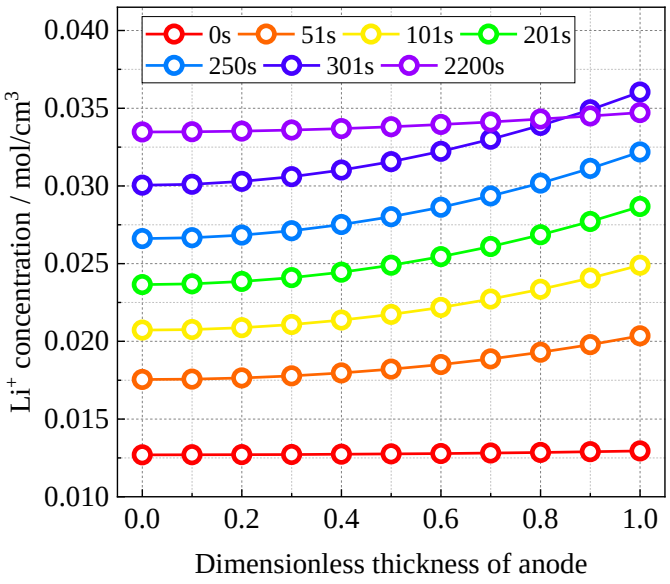

Figure 13. Distribution of surface ion concentration of different particles at different times with 6C rate charging (sim).

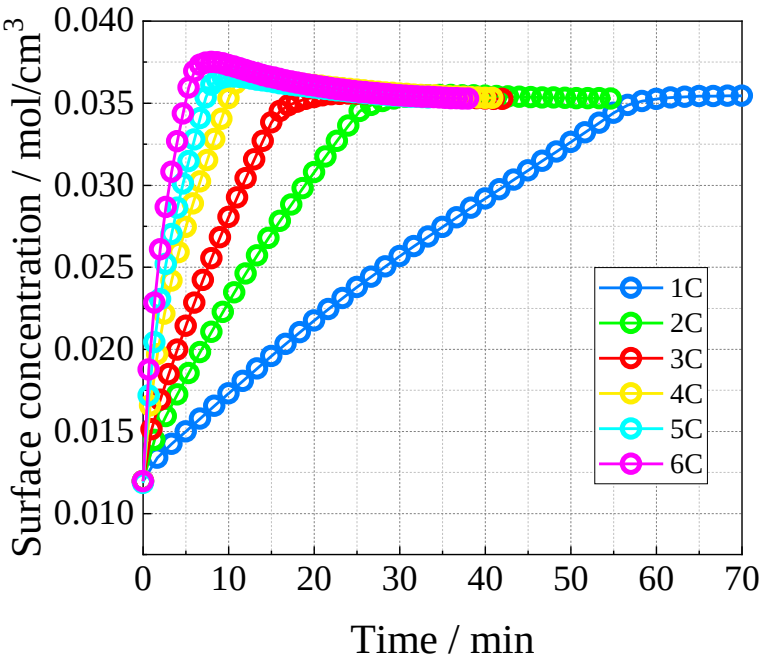

Figure 14. Surface ion concentration of the particles next to the separator (sim).

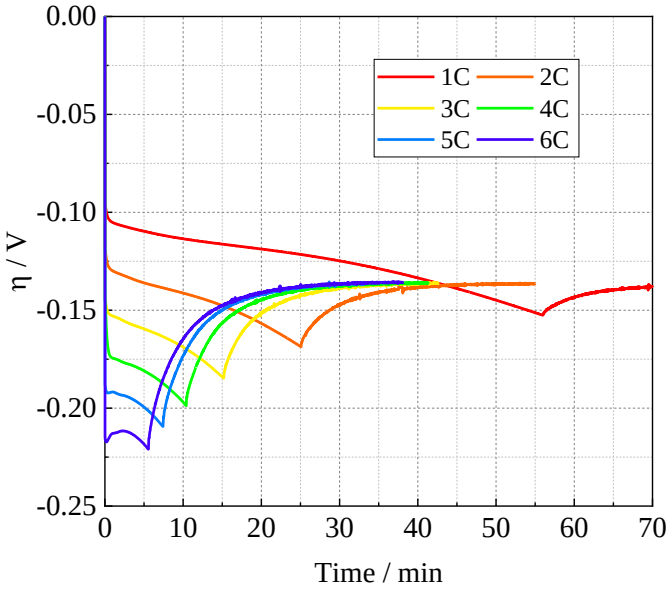

Figure 15. Side reaction overpotential of the particles next to the separator(sim).

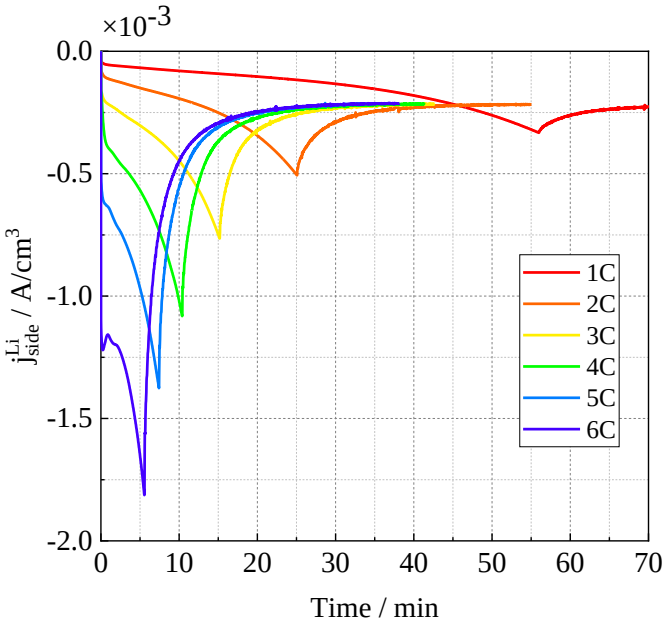

Figure 16. Side reaction rate of the particles next to the separator(sim).

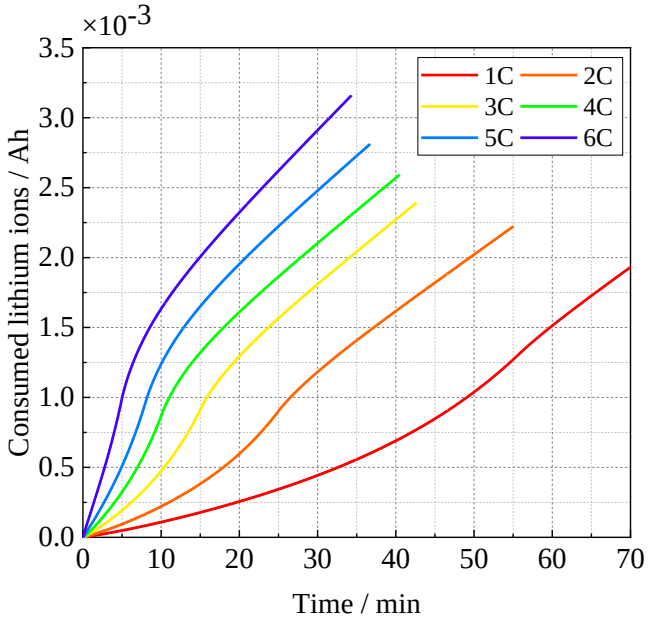

Figure 17. Consumed lithium-ion loss vs. time (sim).

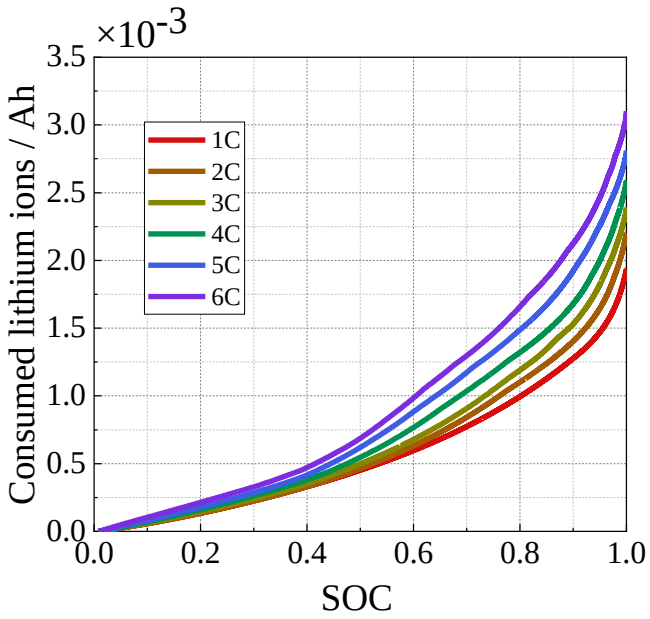

Figure 18. Consumed lithium-ion loss vs. SOC (sim).

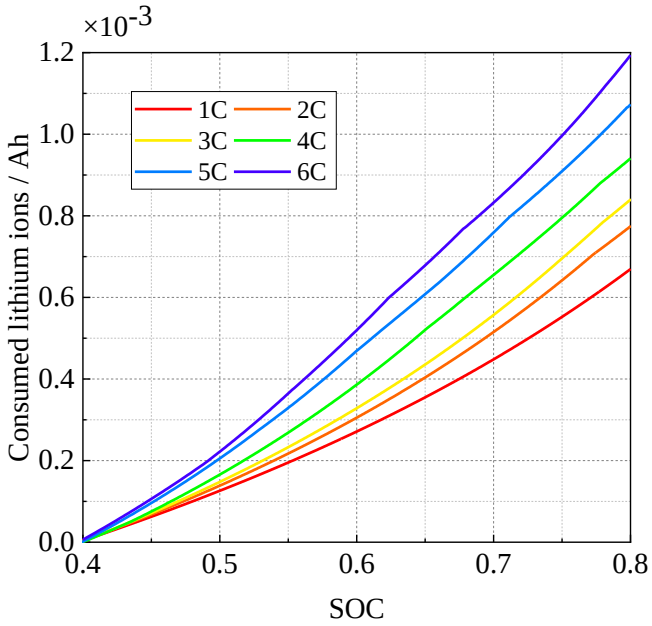

Figure 19. Consumed lithium-ion loss vs. SOC in middle SOC range (sim).

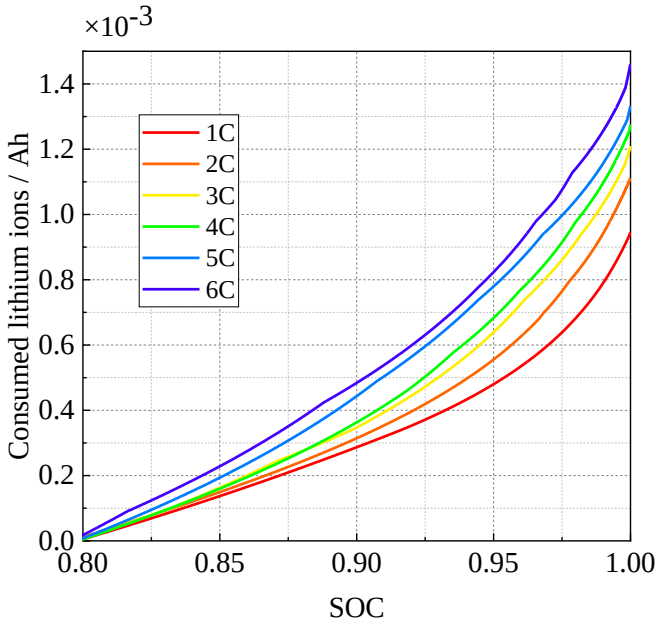

Figure 20. Consumed lithium-ion loss vs. SOC in high SOC range (sim).

2.2.4 Design of a new FC method

The design of the new charging method is based on the ROM-EKF that provides variables like average and surface ion concentrations of particles and anode potentials. The variables are used to estimate SOC and side reaction rate. In order to activate the cutoff voltage, the terminal voltage is measured. A block diagram of the proposed FC method is depicted in Figure 21. The inputs for the ROM-EKF are the charging current, terminal voltage, and the cell temperature. Once the reference values for a requested SOC, cutoff voltage, maximum surface ion concentration, and maximum side reaction rate are given, a charging protocol is generated by comparing the values with those of the estimated and measured and then used to control the charger to generate charging currents.

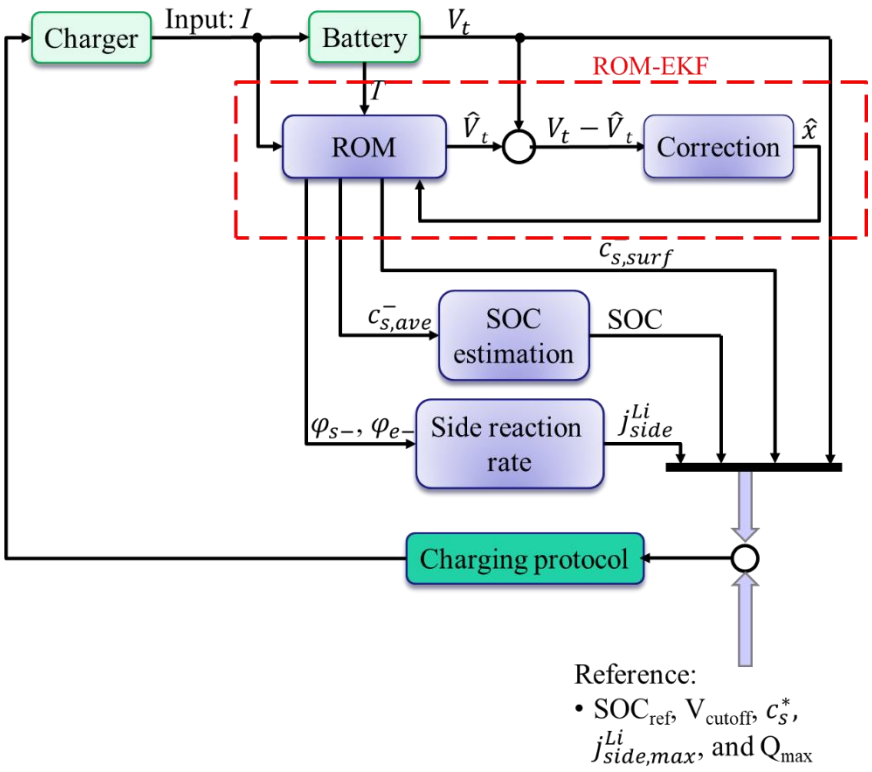

Figure 21. Schematic diagram of a proposed charging method.

When a battery is being charged, the requested SOC is one of conditions that stops charging, while other reference values are used to set the upper limitations related to degradation. A flowchart for the designed charging protocol is depicted in Figure 22. At the beginning, a maximum current C-rate is applied until one of the three variables reaches its upper limitation. Upon reaching the limitation, the charging C-rate is reduced and kept as a constant, according to a predefined ΔSOC, which is repeated until the conditions of stop charging are fulfilled.

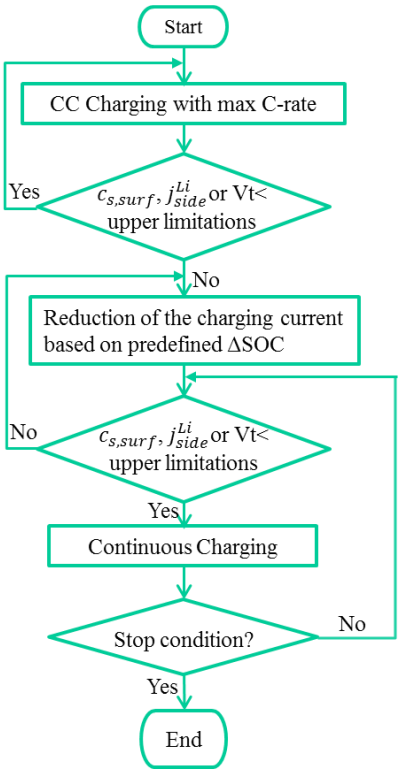

Figure 22. Flow chart for the proposing charging method.

As an example, experimental data between C-rate and SOC limited by the cutoff voltage of 4.15V is plotted in Figure 23, where the circles represent the experimental data. First, the requested SOC is determined as one of conditions that stops charging. Then the battery is charged with a maximum C-rate of 7.6C, which is the maximum charging current provided by the manufacturer. Once the terminal voltage reaches the cutoff voltage, the charging current is reduced to a lower level, according to the given ΔSOC as shown in Figure 23.

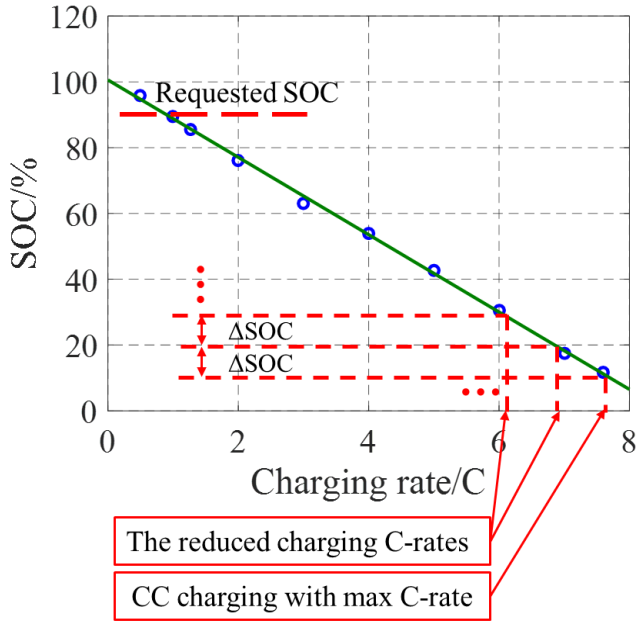

Figure 23. C-rate and SOC limited by the cutoff voltage of 4.15V.

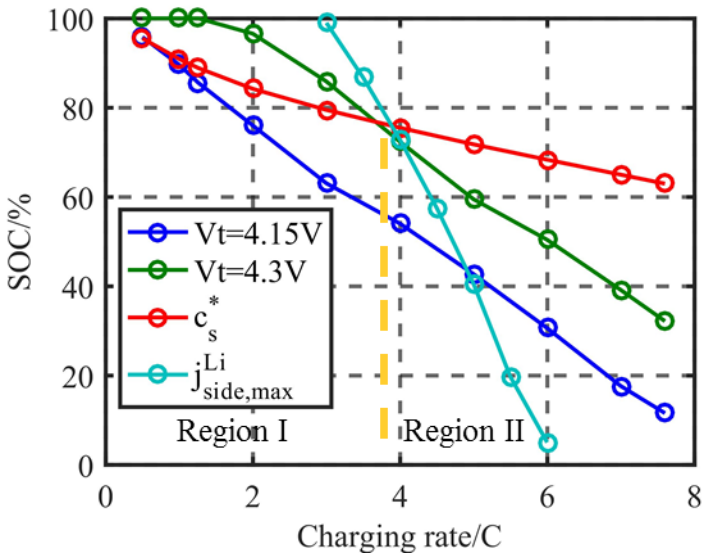

Figure 24. Four limitations to C-rates as a function of SOC (sim).

The charging protocol is optimized by considering other limitations that prevent degradation. The first limitation is the cutoff voltage. The manufacturer of the cell recommends

4.3V at the maximum charging C-rate instead of the normal 4.15V. These effects are investigated later. The second limitation is the calculated maximum surface ion concentration as explained in the previous section. The final limitation is the maximum side reaction rate selected at 40% SOC based on the result of analysis as shown in Figure 24, where the lithium-ion loss does not significantly increase. In consideration of these limitations, SOC as a function of C-rates is simulated and plotted in Figure 24, which provides an important guideline on how the C-rate at different SOC should be determined for an optimal charging protocol that reduces charging time and at the same time alleviates degradation.

Under the consideration of the limitations, several possible protocols are designed by combining the different limitations listed in Table 3. As the results have shown in Figure 24, charging currents can be limited as SOC increases. At a low SOC range, the maximum side reaction rate is the primary limiting factor of the charging current and then the cutoff voltage of 4.15V is applied up to a middle range of SOC and continuously up to 100% SOC. In CV mode with the cutoff voltage of 4.15V at high SOC ranges, the surface ion concentration can exceed the maximum value and an overshoot occurs. Thus, the limitations are divided into two regions. In region I, the maximum concentration, c_s^*, is the first limitation that should prevent the concentration overshoot. In region II, the other three limitations are used to limit the charging current. Since the overshoot of the surface ion concentration of particles is caused by the mismatch of ions between those transported and those diffused, adding extra resting periods helps reduce the numbers of ions transported and gives the ions extra time to diffuse throughout the particles and to be intercalated. Therefore, the duration of the resting period is determined by considering the gradient of ion concentration in the composite anode. Additionally, high charging currents larger than 5C can

make the anode potential negative even at low SOC, which creates favorable conditions for lithium plating. Thus, 5C is selected as the highest C-rate of charging current.

As an example, simulated results of the charging protocol considering $j_{side,max}^{Li}$ and c_s^* are plotted in Figure 25 a-d), which includes the current, terminal voltage, surface ion concentration, and the side reaction rate. The surface ion concentration is limited below the maximum allowed saturation concentration, and the side reaction are also limited up until the ion concentration reaches the upper limitation.

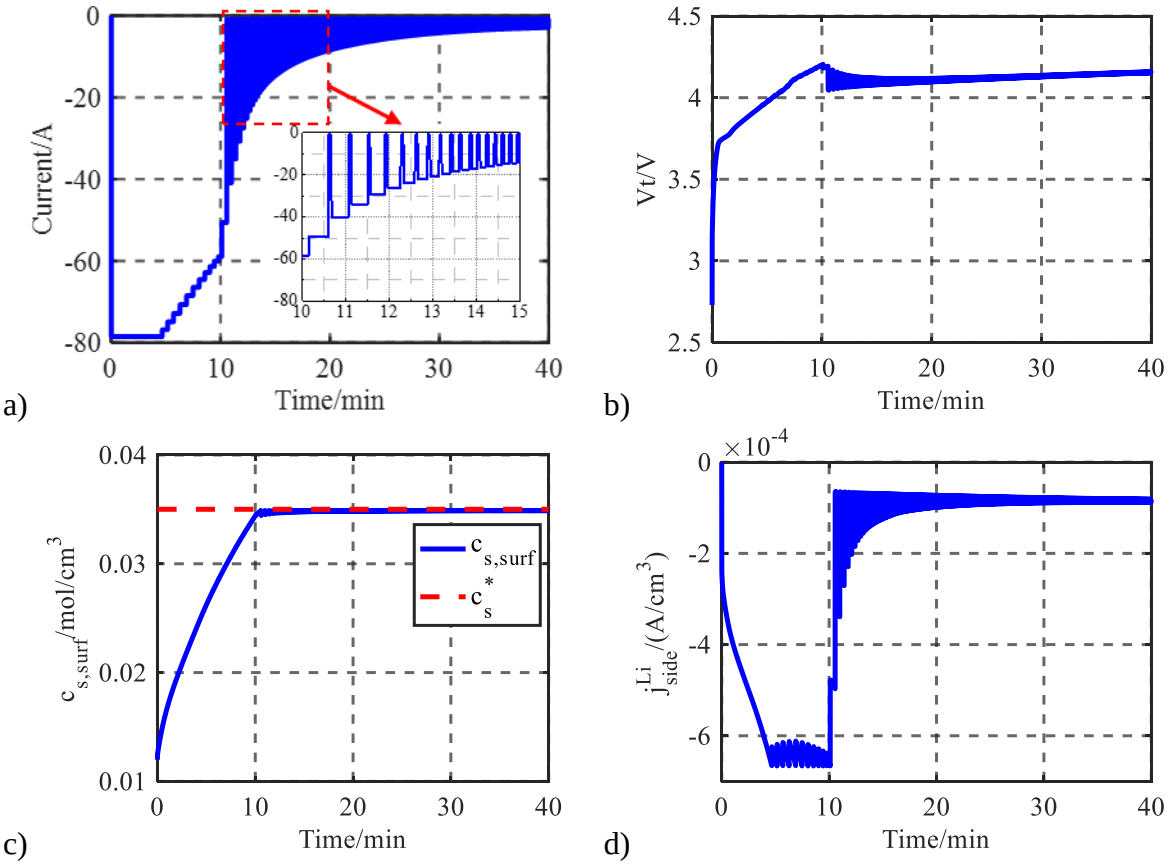

Figure 25. Simulation results of proposing charging protocol considering maximum side reaction rate and surface ion concentration, a) current; b) voltage; c) surface ion concentration; d) side reaction rate. The duration of the resting period is determined by considering the gradient of ion concentration in anode.

Five charging protocols are simulated, and the resulting charging times are summarized in Table 3, where the two classical charging protocols with 1C and 5C CC charging and CV charging by the cutoff voltage of 4.15V are compared. The charging time of 1C CC/CV protocol takes about 71 minutes to fully charge the battery from 0% to 100% SOC. The designed charging protocols considering a cutoff voltage of 4.3V and 4.15V and the maximum surface ion concentration, FC-4.3V and FC-4.15V, reduce the charging time to 44% and 52% of that by the 1C CC/CV charging protocol, respectively, where increased cutoff voltage has contributed to reduce the charging time. The charging time by FC-4.15V is comparable to that of the CC/CV (5C) protocol. The charging time of the protocol that considers side reaction and surface ion concentration takes longer than others because it reduces the total time spent in the CC mode.

Table 3. Charging time of different charging protocols.

Charging protocol	CC/CV (1C)	CC/CV(5C)	FC-4.3V	FC-4.15V	FC-SR
Limitation	4.15V	4.15V	4.3V and c_s^*	4.15V and c_s^*	Side reaction and c_s^*
Charging time	71min	38min	31.5min	37.5min	40min

Simulation results of the side reaction rate and consumed lithium ions of four charging protocols are plotted in Figure 26 and Figure 27, where, for brevity, results with 1C are not shown. The area enclosed by the side reaction rate represents the total amount of consumed lithium ions. When the cutoff voltage increases, the CC charging periods become extended, but the magnitude of the side reaction rate becomes higher and the duration is longer. Consequently, the consumed lithium-ion loss increases. If the side reaction rate is further limited, the area becomes smaller and the ion loss becomes significantly reduced, but the charging time is increased.

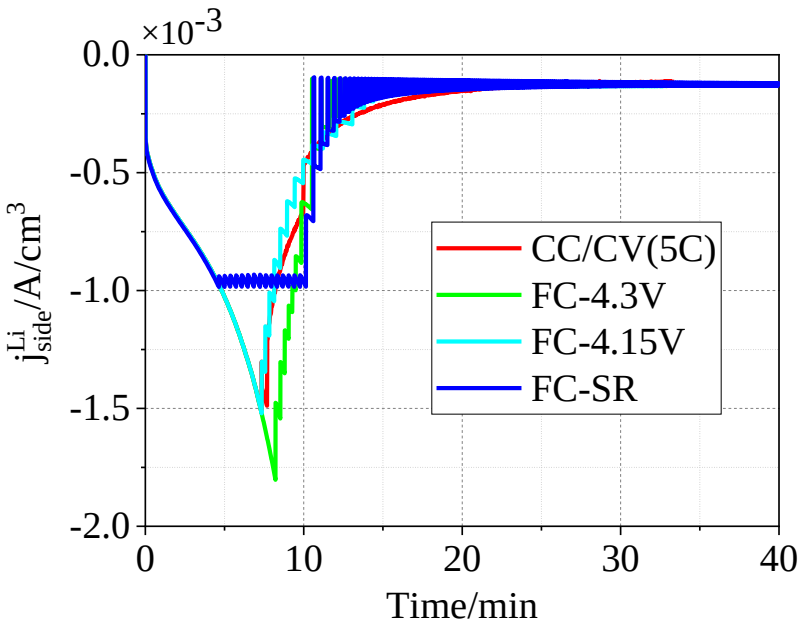

Figure 26. Side reaction rates of four charging protocols (sim).

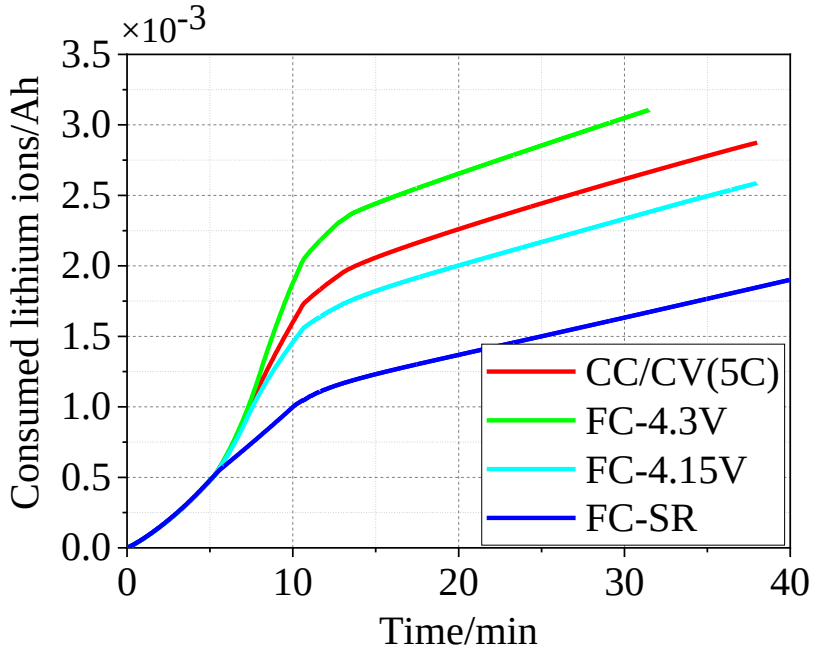

Figure 27. Consumed lithium ions of four charging protocols (sim).

2.2.5 Experimental assessment of the protocols and analysis

The different charging protocols were implemented and experimentally evaluated using BIL that facilitates the operation of a test station with the designed controls in real time. The test station was designed to charge and discharge the battery using a DC power supply and an electronic load that are connected in parallel to the battery and controlled by LabVIEW embedded in a PC. In addition, the battery was placed in a designed thermostat system that dynamically rejects the heat generated by the battery. The thermostat system consists of two thermal electric modules (TEMs), a bipolar power supply, and a control algorithm that determines both magnitude and direction of the current flowing into the TEMs. The TEMs have both cooling and heating functions, so the thermostat system can regulate the battery temperature. In this research, the thermostat system is only used to regulate the surface temperature of the battery at a set value. The maximum temperature variation becomes less than $1^{o}C$ even at a 120A charging current. Thus, this thermostat system allows for a minimization of the effects of the temperature on degradation.

The proposed charging method is implemented in the test station by integrating the ROM-EKF into LabVIEW using a MATLAB script. The ROM-EKF facilitates estimation of the internal variables like SOC, ion concentrations, and the side reaction rate based on the current and terminal voltage, which is used to constrain the charging current and generate the charging protocol for the requested SOC.

The battery used for the experiments is a pouch-type large format lithium-ion cell, whose dimension is about 200mm×150mm×5mm. The capacity is 15.7Ah and the operating voltage is in the range of 2.5V to 4.15V.

After the implementation of the ROM-EKF in the test station, different charging methods were tested under the same test conditions that were also used for the simulations and then repeated for 100 cycles, where the cell was charged up to 100% SOC and then discharged at a rate of 1C to 0% SOC at 25^{o}C. The charging time of the five charging protocols in different SOC ranges is summarized in Figure 28. The measured charging times are almost the same as those in the simulations. Compared with the normally recommended 1C CC/CV charging protocol, the other protocols can reduce the charging time by more than half in the low and middle SOC ranges. However, in the high SOC range, the designed charging methods cannot reduce the charging time further. The charging time of the designed charging protocols is almost the same in the low SOC range but differs in the middle SOC range because different limitations are applied. The FC-SR protocol, which limits side reaction, takes the longest of all the designed protocols.

The capacity of the cells is measured after every 10 cycles using the 1C CC/CV charging and discharging method. A dimensionless capacity, Q^{*}, defined as the ratio of capacity of the aged cell to that of the fresh cell is introduced;

$$Q^{*} = \frac{Q_{aged}}{Q_{fresh}}. \tag{9}$$

The dimensionless capacities of the five charging protocols are plotted in Figure 29.The comparison between FC-4.3V and FC-4.15V shows that an increase in the cutoff voltage accelerates the aging speed substantially. The limitation of the charging current by surface ion concentration helps prevent the capacity fade, which is proved by the comparison between FC-4.15V and CC/CV(5C). The capacity fade of the FC-SR protocol is the least of the designed charging protocols and the closest to that of the CC/CV(1C). Thus, the designed charging methods reduce the charging time and degradation speed. However, the degradation speed of the FC-SR

protocol is still slightly higher than that of CC/CV(1C), which is caused by two different factors. Firstly, the lithium-ion loss by the FC-SR protocol is slightly larger than that by CC/CV(1C) in the low SOC range. Secondly, the internal temperature of the battery by the FC-SR protocol is slightly higher than that by CC/CV(1C) because of more heat generated although the surface temperature is kept constant by the thermostat system.

Additionally, the impedances at different charging protocols measured by the Electrochemical Impedance Spectroscopy (EIS) are plotted in Figure 30 and Figure 31. The left intercept between the impedance spectra and the x-axis at high frequency represents the ohmic resistance and the radius of the first semi-circle represents the SEI resistance. Both of them were extracted using an EIS equivalent circuit model [28]. The growth of both resistances is directly related to power fade. The ohmic resistance of different charging protocols is almost the same as that of the fresh cell, which implies that the side reaction do not contribute to an increase of the ohmic resistance at the BOL. The growth of the SEI resistance after 100 cycles was dependent upon protocols, where the SEI resistance by the FC-SR is comparable to that of CC/CV(1C).

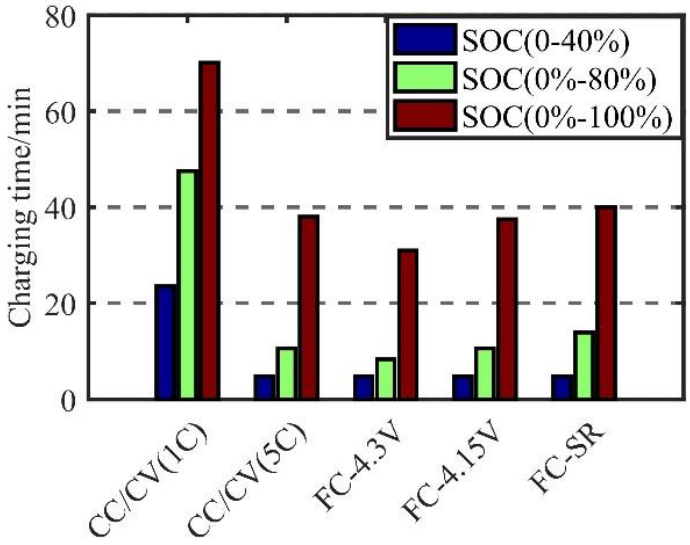

Figure 28. Comparison of charging time of five charging protocols (exp).

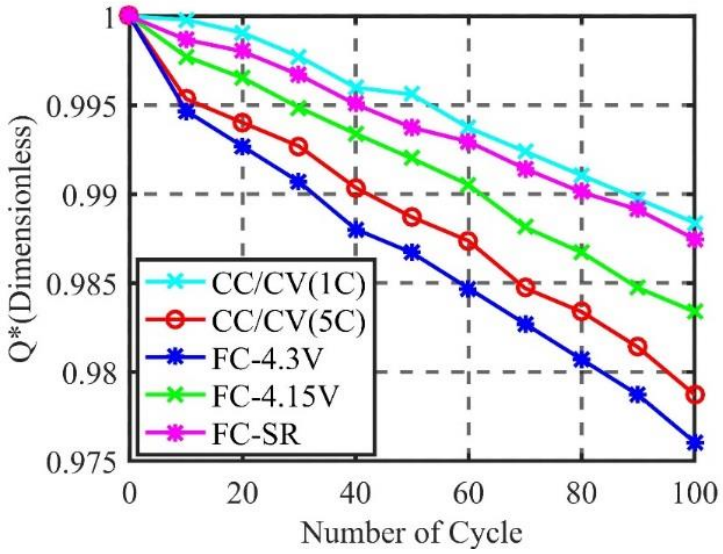

Figure 29. Comparison of capacity fade of five charging protocols (exp).

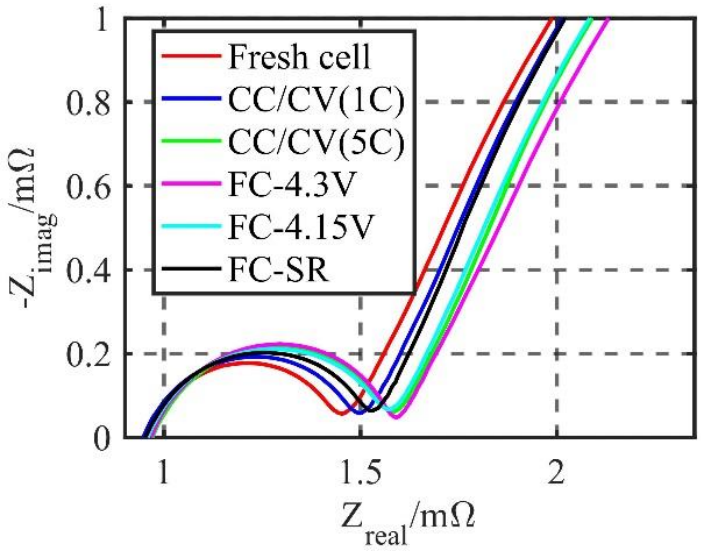

Figure 30. The impedance spectra of five charging protocols measured by EIS (exp).

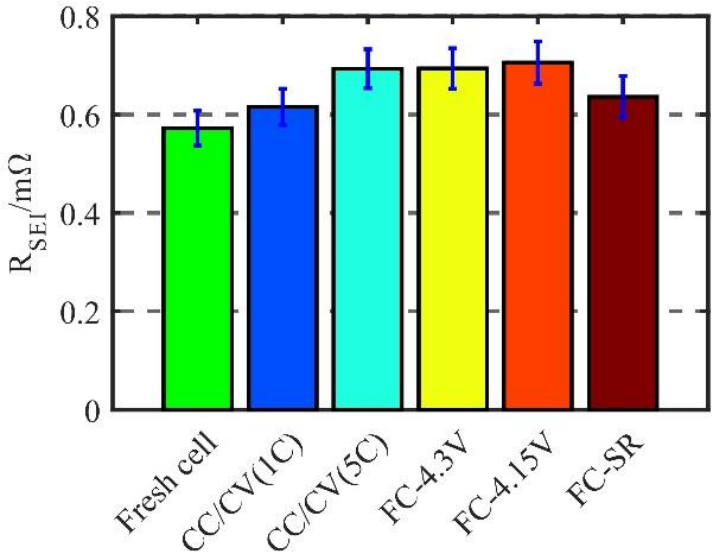

Figure 31. The estimated SEI resistance of five charging protocols (exp).

2.3 Conclusion

An optimization of a FC method was proposed that considered charging time and degradation at the beginning of life of battery. Effects of an increase in C-rates, cutoff voltages and internal variables on degradation were identified and analyzed. In order to find an optimal charging protocol, the two internal variables, surface ion concentration and side reaction rate, were estimated by using a ROM along with an extended Kalman filter. The maximum surface ion concentration and side reaction rate were used to limit the charging currents. The method was implemented in a BIL system and tested for 100 cycles, which verified the protocol with the least capacity and power fade.

Here is a summary of major findings.

- Effects of different amplitudes of charging C-rates on the charging time and side reaction in CC/CV charging are different depending upon SOC ranges. In the low SOC range, high

charging C-rates increase the side reaction, but reduce the charging time, so that the contribution of the amplitude of charging C-rates on aging speed is not significant. In middle and high SOC ranges, the charging C-rate has a significantly greater influence on aging speed.

- The proposed charging method was designed using ROM-EKF with a side reaction rate model, where cutoff voltage, saturation of ion concentration, and maximum side reaction rate are used to limit the charging currents. The method reduces about half of the charging time compared with the normal 1C CC/CV charging protocol. Increased cutoff voltage decreases the charging time but increases the capacity and power fade substantially. The limitation of charging current by surface ion concentration helps prevent the capacity and power fade. The charging method limited by surface ion concentration and side reaction rate has shown the best performances with respect to charging time and degradation.

Chapter 3 Optimal FC method considering side reaction and lithium plating at a constant temperature

3.1 Literature review

Currently, there are variously suggested charging methods without use of battery models, which includes multi-stage CC and CV [45][46], neural networks[47], fuzzy logic [48] and to name a few. These methods are based on heuristic knowledge or empirical observations of battery dynamics. Thus substantial improvements are limited because the models fail to provide fundamental information for degradation. There are many other suggestions for charging method to improve the performances using electric equivalent circuit models (EECM) [16][49], or electrochemical models [24][27] with respect to charging time, degradation, heat generation and safety. These methods generate a charging protocol based on the estimated states of the battery. However, these methods only consider a few charging features or constraints and do provide neither mathematical guarantee for optimal performance of the FC method, nor satisfy constraints

Those two challenging issues such as charging time, safety and aging constraints have been attempted to solve. These approaches can be grouped into offline and online ones. The offline one refers to as a global optimization approach, which optimizes the charging protocol by simulations using battery models. The employed optimization techniques are Legendre-Gauss-Radau pseudo-spectral method [50], Pontryagin's principle [26], dynamic programming technique [51], Interior Point OPTimizer [52] and etc. Hence, charging time [26][50] and degradation by side reaction rate and lithium plating rate [51] [52] are used in the objective function, where the constraints are set to guarantee safety and limit the degradation speed. The safety is secured by

three basic constraints including charging current, terminal voltage and temperature. The degradation speed by the lithium plating is limited by the anode potential [26][50] [52].

All the charging methods above have shown improved charging performances, but the charging protocols are obtained only though offline simulations using the battery models. This offline approach neglects the effects of model-plant mismatch and disturbances that are present in real world applications. These real world problems can be better handled by employing MPC for the optimization of charging method, which reduces the charging time, limits the degradation speed and secures the safety of battery. For ECM, the constraints are input current, output terminal voltage, and SOC [53]. However, no aging effects are considered.

For electrochemical models, physics-based degradation models are incorporated that take lithium plating and side reaction into account. The formation of the lithium plating can be suppressed when the anode overpotential of lithium plating is kept to be larger than 0V [21][54] [55]. In addition, side reaction is included in the objective function [56]. These methods accomplished reduction of the charging time and limit the degradation speed. However, since the overpotential as the constraint is larger than 0V, the maximum charging current is limited accordingly and consequently the charging time gets increased.

Because of the concerns on computational time of the optimization, there are other attempts of using a linear time-varying MPC employed single particle model (SPM) [55], where the input of state space equations for the internal variables is charging current. However, the single particle in anode impedes integration of physics based degradation model because SPM ignores the gradient of concentration and potential over the anode [33], so the pseudo-two-dimensional electrochemical model (P2D) is chosen as a frame model, but makes it difficult to obtain the matrix of state space equations for internal variables with input of charging current because main chemical

reaction rates are the input of state space equation of the ion concentrations in particles rather than input charging current.

Therefore, NMPC is selected for design of an optimal FC method based on a hybrid ROM that consists of P2D model for anode and SPM for cathode (ROM-P2D+SPM), respectively. In addition, pulse discharging current is employed in the charging protocol to promote the lithium stripping, which ultimately slows down the capacity fade [57][58].

3.2 ROM with degradation effects

Design of an optimal FC method considering degradation requires information of internal physical variables of battery in real time such as ion concentrations, anode potential and side reaction rate. These variables are directly immeasurable, but can be estimated by an electrochemical model that runs in real time. Due to the constraints of computational time, a ROM is developed to estimate the variables that include those related to degradation as well.

3.2.1 ROM

A pouch-type LiB is made of stacked single microcells that are connected in parallel by current collectors. The micro cell has a sandwich structure in the thickness direction that is composed of two composite electrodes and a separator in between, as depicted in Figure 32. The charging and discharging of batteries involves several processes that can be mathematically described using a FOM. In order to reduce the computational time, a ROM is used. The detailed descriptions of the model reduction approaches can be found in references [43][59].

The ROMs can be categorized into Pseudo-two-Dimensional (P2D) model and Single Particle Model (SPM). The P2D model considers several particles in the electrodes, which allows for relatively accurate predictions and representation of real behaviors [43]. In addition, gradients of ion concentrations and the associated potentials can be predicted, which allows for taking degradation effects into account including the side reaction and lithium plating that take place in the anode. However, the P2D model still consumes high computational time and requires large memories due to its high order matrices resulted from calculations in each grid and its complex code structure.

The ROM-P2D can be further simplified under assumptions that the current in electrodes are uniformly distributed and the size of the particles in each electrode is identical, which results in ROM-SPM. On the other hand, ROM-SPM cannot provide any gradients of inner states in both electrodes, which impedes the incorporation of the degradation effects. Therefore, a new ROM is constructed that consists of SPM on the cathode electrode and P2D on anode electrode to incorporate the side reaction and lithium plating. As a result, both of the computational time and the aging effects are traded off, which is called ROM-P2D+SPM. A schematic diagram for the resulting ROM is depicted in Figure 32, where *n* spherical particles in anode through the plane are considered, while a single particle represents the cathode electrode.

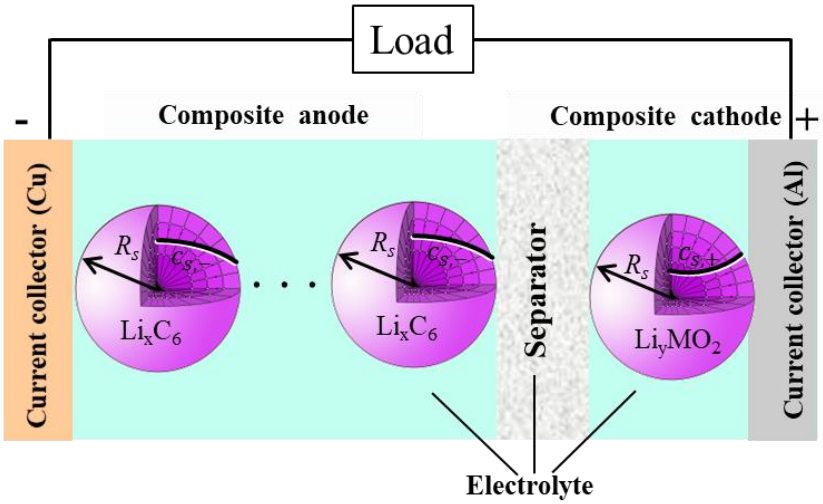

Figure 32. Schematic diagram of ROM-P2D+SPM.

3.2.2 Degradation submodels

According to the investigations on degradation mechanisms conducted with a large format LiB with NMC/Carbon or LFP/carbon, the most dominant causes for degradation are side reaction and lithium deposition reaction that take place at the surface of anode graphite particles [33][29].

Side reactions are a reduction process between electrolyte solvent and lithium ions that occurs at the anode particle surface. The products of the side reaction form a thin film layer that adheres to the surface of anode particles, which is called solid electrolyte interphase (SEI). This layer is permeable for lithium ions but rather impermeable for electrons [34]. Therefore, the initial formation of SEI layer prevents electrons from flowing to the surface and as a result the reaction becomes less. However, SEI layer gradually grows during cycling because electrolyte solvents diffuse to the particle surface and take part in the side reaction, although the growth of SEI layer is not nearly as great as the amount during the initial formation. Lithium ions consumed by side reaction cannot take part in the main chemical reactions, which leads to loss of ions and capacity

fade. In addition, some particles may be completely covered by the SEI layer and become electrically isolated. The isolated particles cannot participate in the main reactions, which leads to loss of active materials and capacity fade. Since SEI layer has relatively low ionic conductivity, grown SEI layer leads to increase of impedance and thus power fade. The degradation model for side reaction are summarized in Table 4. The details of degradation model for side reaction can be found in [33][39].

Table 4. Degradation model for side reaction.

Aging effects	Equations
Side reaction rate	$j_{side}^{Li} = -i_{0,side} a_s \exp\left(-\frac{\alpha_{c,side} n_{side} F}{RT} \eta_{side}\right)$
The amount of ion loss caused by side reaction	$q_{loss}^{SR}(\tau) = \int_{x=0}^{\delta_-} \left(\int_{t=0}^{\tau} \left| j_{side}^{Li}(l,t) \right| dt \right) A dl$
The change of volume fraction of electrolyte	$\Delta\varepsilon_{e,side}(\tau) = -\frac{\alpha \tilde{V}_e q_{\text{loss}}^{SR}(\tau)}{A\delta_- F}$
Increase of thickness of SEI layer	$\frac{\partial \delta_{SEI}}{\partial t} = -\frac{\tilde{V}_{SEI}}{2 a_s F} j_{side}^{Li}$
Increase of thickness of deposit layer	$\frac{\partial \delta_{DL}}{\partial t} = -\frac{R_s \tilde{V}_{DL}}{2F} j_{side,x=\delta_-}^{Li}$
Increase of resistance of SEI layer	$\Delta R_{SEI} = \delta_{SEI} / \kappa_{SEI}$
Increase of resistance of deposit layer	$\Delta R_{DL} = \delta_{DL} / \kappa_{DL}$
Decrease of active material volume fraction	$\Delta\varepsilon_s = -k_s a_s \delta_{SEI}$

Under charging, lithium ions are inclined to form metallic lithium that is deposited on the particle surface instead of intercalating into the negative electrode, which is called “lithium plating”, also known as “lithium deposition reaction”. This lithium deposition reaction is induced

by the lithium ions and electrons and forms a metallic layer that consumes lithium ions. The reaction is kinetically promoted when the anode potential is close to that of metallic Li deposition (0V vs Li^+/Li). So, lithium plating predominantly occurs under extreme charging conditions, such as high current [30], low temperatures [60], and overcharging [32]. The plated lithium covers the surface of particles of the anode, which results in reduction of the active area. In addition, the plated lithium metal reacts with solvents of electrolyte to form an additional SEI layer that is called the secondary SEI layer [61]. More importantly, the continuous growth of the lithium plating forms dendritic aggregation that may trigger an internal short when piercing through the separator that leads to thermal runaway and safety accidents. During discharging process, the plated lithium can be partially dissolved and extra lithium ions are released, which is called lithium dissolution reaction also known as lithium stripping [62]. This reaction promotes recovery of ions that are lost during the lithium plating reaction, so a certain amount of capacity can be recovered.

The lithium plating and stripping rate is described using B-V equation as follows;

$$j_{P/S}^{Li} = a_s i_{0,Li}\left[\exp\left(\frac{\alpha_{a,Li}F}{RT}\eta_{P/S}\right) - \exp\left(-\frac{\alpha_{c,Li}F}{RT}\eta_{P/S}\right)\right], \tag{10}$$

where $i_{0,Li}$ is the exchange current density of the reaction. $\alpha_{a,Li}$ and $\alpha_{c,Li}$ are the dimensionless anodic and cathodic charge transfer coefficient, which are assumed to be a value of 0.33 and 0.67, respectively, because the lithium plating and stripping are semi-reversible [61][62].

The reaction rate of lithium plating and stripping are denoted as the j_P^{Li} and j_S^{Li}, respectively. The activation overpotential of the lithium plating and stripping, $\eta_{P/S}$, is calculated using

$$\eta_{P/S} = \varphi_{s-} - \varphi_{e-} - U_{eq,Li} - \frac{R_{SEI}}{a_s} j_{total}^{Li} \ , \tag{11}$$

where $U_{eq,Li}$ is the equilibrium potential for lithium plating and stripping, which is equal to 0V [62]. When the overpotential, $\eta_{P/S}$, becomes negative, the lithium ions prefer to deposit on the surface of particles rather than intercalate into the electrode. The degradation models for lithium plating and stripping are summarized in Table 5. The details of the degradation model for side reaction can be found in [58][62].

Table 5. Degradation model for lithium plating and stripping.

Aging effects	Equations
Ion loss by lithium plating	$q_{\text{loss}}^{LiP}(\tau) = \int_{x=0}^{\delta_-} \left(\int_{t=0}^{\tau} (1-\lambda) \left| j_P^{Li}(x,t) \right| dt \right) A dx$
Ion loss by formation of secondary SEI	$q_{\text{loss}}^{SEI,\text{sec}}(\tau) = \int_{x=0}^{\delta_-} \left(\int_{\tau=0}^{\tau} \lambda \left| j_P^{Li}(x,t) \right| dt \right) A dx$
Amount of recovered lithium ions by lithium stripping	$q_{\text{recovery}}^{LiS}(\tau) = \int_{x=0}^{\delta_-} \left(\int_{\tau=0}^{\tau} j_S^{Li}(x,t) dt \right) A dx$
Increase of thickness of plated lithium	$\frac{\partial \delta_P}{\partial t} = -\frac{\tilde{V}_{Li}}{a_s F} \left((1-\lambda) j_P^{Li}(x,t) + j_S^{Li}(x,t) \right)$
Increase of thickness of secondary SEI	$\frac{\partial \delta_{SEI,sec}}{\partial t} = -\frac{\tilde{V}_{SEI}}{a_s n_{side} F} \lambda j_P^{Li}(x,t)$
Reduction of volume fraction of active material	$\Delta \varepsilon_{s,LiP} = -a_s \left(\Delta \delta_P + \Delta \delta_{SEI,\text{sec}} \right)$
Decrease of volume fraction of electrolyte	$\frac{\partial \varepsilon_e}{\partial t} = -\frac{\alpha \tilde{V}_e q_{loss}^{SEI,\text{sec}}}{A \delta_- F}$

3.2.3 Validation of ROM-P2D+SPM with degradation submodels

The designed ROM-P2D+SPM embedding side reaction and lithium plating is validated using a pouch-type battery, whose capacity is 40Ah. The active material of the anode and cathode for the battery is carbon and NMC ($Li[MnNiCo]O_2$), respectively. The values of the model parameters for the battery is listed in Table 6. The ROM with degradation model is validated against the experimental cycling data with different charging currents and protocols from 0% to 100% SOC, where the surface temperature of the battery is controlled to be constant using a designed thermostat system. As a result, effects of temperature on the charging and discharging characteristics are minimized. A dimensionless capacity, Q^* is defined as the ratio between the capacity of an aged cell to that of the fresh cell. The simulated and experimental dimensionless capacities obtained by cycling with 2C CC/CV charging and 1C discharging are plotted in Figure 33, where the prediction error of the capacity over cycles is negligible. In addition, the simulated terminal voltages at different cycles compared with the experimental results, as shown in Figure 34, which shows that the predicted terminal voltages of ROM-P2D+SPM with degradation model match well with those of experiments.

When the cell is cycled with 2C CC/CV charging, the capacity drops linearly until 120 cycles, which is mainly caused by the side reaction. After 120 cycles, the capacity drops rapidly because of lithium plating. In order to promote lithium plating, 5C CC charging with the same discharging condition for 100 cycles is applied. Similarly, lithium stripping is promoted by applying an extra 2C pulse discharging current for 160 cycles. The experimental data of the capacity is compared with that by simulation, as shown in Figure 35, where the model can predict the capacity fade well. At the beginning of cycling, the capacity decreases linearly, but after 60

cycles rapidly, where a transition from a linear to a nonlinear range is observed. As shown in Figure 36, the ion loss caused by side reaction increases linearly, but the ion loss by the lithium plating starts after 60 cycles and then increases rapidly, which results in a rapid drop of the capacity fade.

Table 6. List of model parameters (a: manufacturers; b: tuning with the model; c: literature).

Category	Parameter	Negative electrode	Separator	Positive electrode	Source
Design specifications	Thickness, δ (cm)	$94.5*10^{-4}$	$9.5*10^{-4}$	$72.0*10^{-4}$	a
Lithium-ion concentration	Maximum solid phase concentration, $c_{s,\,max}$ (mol cm^{-3})	$52.5*10^{-3}$		$67.2*10^{-3}$	b
	Stoichiometry at 0% SOC: *Stoi*0	0.3421		0.8764	b
	Stoichiometry at 100% SOC: *Stoi*100	0.8562		0.3268	b
	Charge-transfer coefficient, α_a, α_c	0.5, 0.5		0.5, 0.5	c[22]
	Solid phase conductivity, σ (S cm^{-1})	1		0.01	c[22]
	Electrolyte phase Li^+ diffusion coefficient, D_e (cm^2 s^{-1})	$2.6*10^{-6}$	$2.6*10^{-6}$	$2.6*10^{-6}$	b
	Solid phase Li^+ diffusion coefficient, $D_{s,0}$ (cm^2 s^{-1})	$1.08*10^{-10}$		$1.08*10^{-10}$	b
	Bruggeman's porosity exponent, p	1.5	1.5	1.5	c[22]
	Electrolyte phase ionic conductivity, κ (S cm^{-1})	$15.8c_{e*}\exp(-13472c_e^{1.4})$			c[22]
	Li^+ transference number, t_+^0	0.363	0.363	0.363	c[22]
Side reactions	Equilibrium potential of side reactions, $U_{eq,\,side}$ (V)		0.4		c[39]
	Kinetic rate constant for side reactions, k_{side} (A cm mol^{-1})		$8.28*10^{-9}$		b
	Cathodic symmetric factor of side reactions, $\alpha_{c,side}$		0.7		c[33]
Lithium plating/stripping	Equilibrium potential of lithium plating, $U_{eq,\,Li}$ (V)		0		c[63]
	Exchange current density for lithium plating, $i_{0,Li}$ (A cm mol^{-1})		$3.37*10^{-8}$		b
	Cathodic factor of lithium plating, $\alpha_{c,Li}$		0.7		c[63]
	Anodic factor of lithium plating, $\alpha_{c,Li}$		0.3		c[63]

When cycled with 5C CC charging at 25°C, the terminal voltage does not show any plateau because of lithium stripping at the beginning of discharging. Since no lithium stripping takes

places, the most plated lithium reacts with electrolytes and forms the secondary SEI. As shown in Figure 35, the capacity fade of 5C CC charging with 2C pulse discharging current is less than that of 5C CC charging, which is contributed by lithium stripping during the 2C pulse discharging. Ion loss caused by the side reaction and the lithium plating and ions recovered by lithium stripping are calculated using the validated model and plotted in Figure 36. Even though a large number of ions are lost by the lithium plating, the pulse discharging current enables to recover most of them, so the total ion loss becomes much less than that by simple CC charging.

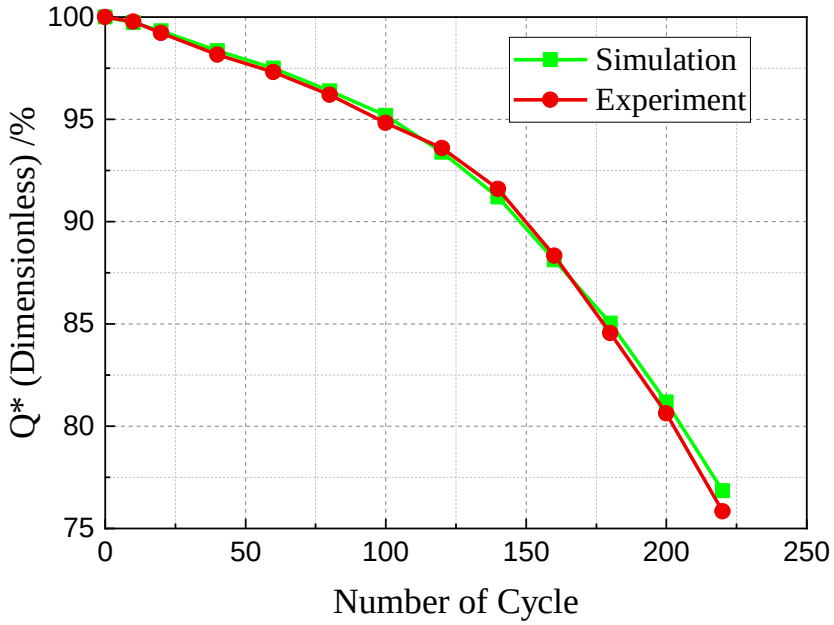

Figure 33. Comparison between measured and simulated capacities.

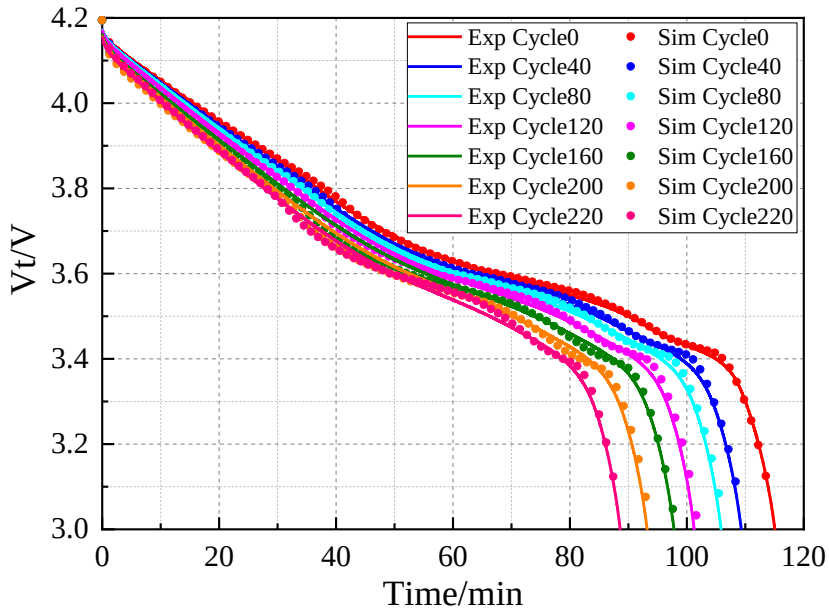

Figure 34. Validation of discharge behaviors.

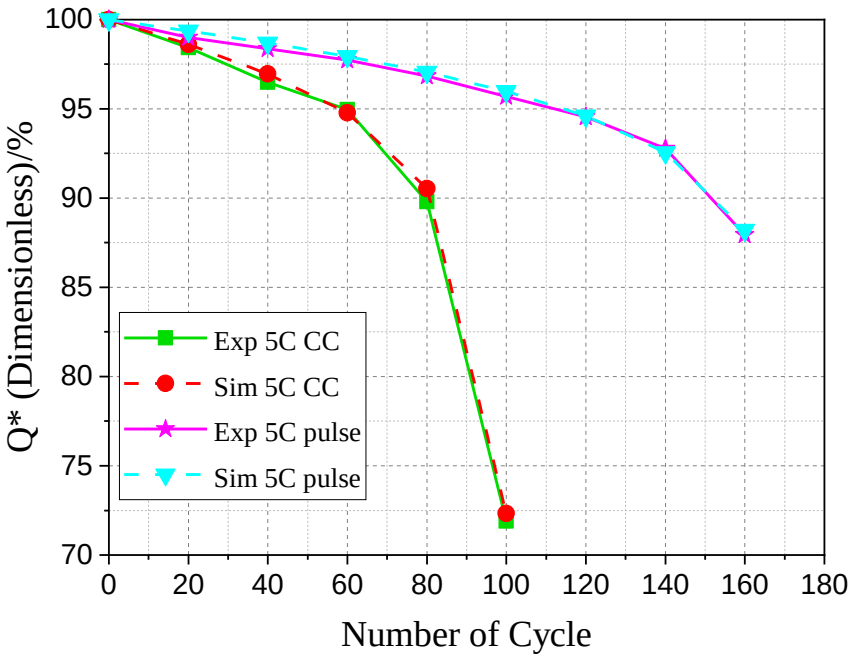

Figure 35. Capacity fade at 5C CC charging and 5C CC charging with pulse discharging

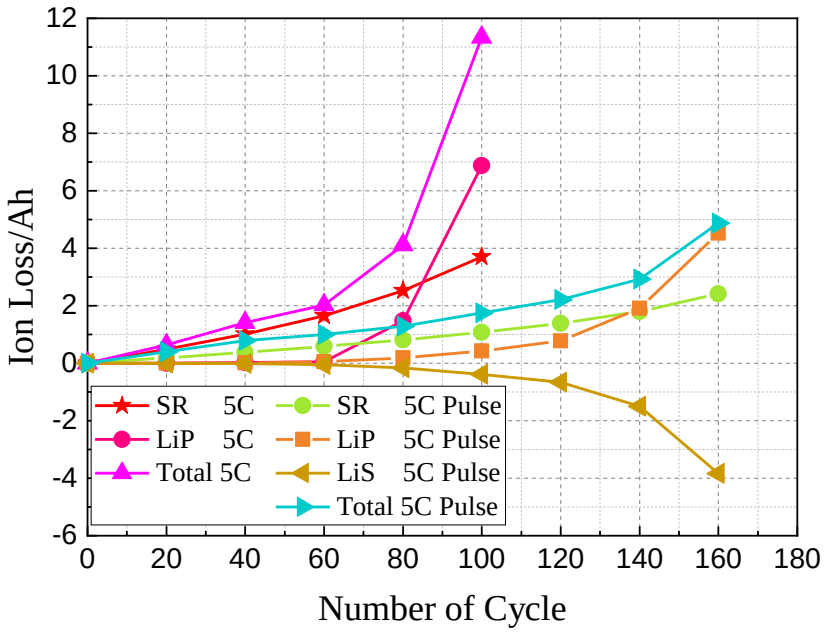

Figure 36. Ion loss and recovery from side reaction and lithium plating and stripping at 5C CC charging and 5C CC charging with pulse discharging (sim).

3.3 Design of optimal FC method

Reduction of charging time and suppression of degradation are the two goals for optimal design of a charging protocol. The following two steps have been taken for the design: Firstly, the optimization is carried out without considering lithium plating and effects of weighting factors on the design are analyzed, which results in finding a weighting factor for the optimal design. Then, the lithium plating is considered and pulse discharging current is added to promote lithium stripping, which is called optimal FC with pulse discharging currents (OFCPD).

3.3.1 Design of optimal FC method without considering lithium plating

NMPC is a widely used online optimal control method that finds optimal control input under consideration of constraints. In the application of optimal charging of battery, the external constraints such as terminal voltage and temperature can be measured directly. Internal constraints can be derived from the ROM, whose accuracy is improved by estimation method like Sigma-Point Kalman Filter (SPKF) [64]. The block diagram for the concept is depicted in Figure 37. When the objective (y^r , e.g. target SOC) is set at time step *k*, NMPC predicts states and outputs of the plant over the prediction horizon *N* and then determines the charging current as control efforts over the control horizon *N*. This is accomplished by solving an open-loop optimal control problem in order to minimize the objective function. In order to simplify the design of optimal charging method, the control horizon is assumed to be equal to the prediction horizon [65]. The first part of the optimal charging current, $I^*(k)$ is applied to the battery for charging. At the next time step, *k*+1, the states are updated based on the measured output and then the whole procedure (prediction and optimization) is repeated.

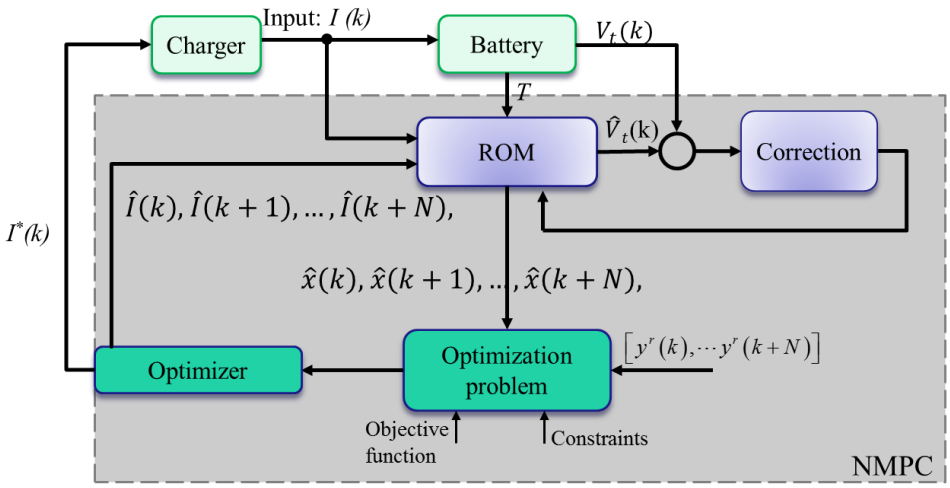

Figure 37. Schematic block diagram of proposed optimal charging method.

3.3.1.1 Formulation of optimal charging problem

The charging method pursued by this research aims to charge the battery as fast as possible without significantly accelerating the degradation speed. Thus, the objective function, J is set by

$$J = \min_{I(t)} \left(\int_{t_0}^{t_f} \left(\alpha \cdot 1 + \beta \dot{q}_{loss}^{SR}(t) \right) dt \right), \tag{12}$$

where α and β are weighting factors that adjust the trade-off between fast charging and aging processes. $\dot{q}_{loss}^{SR}$ is the ion loss rate over the volume of the composite anode, which is calculated using

$$\dot{q}_{loss}^{SR}(t) = \int_{x=0}^{\delta_-} \left(\left| j_{side}^{Li}(l,t) \right| \right) A dl \,. \tag{13}$$

The objective function is very useful for the offline global optimization, however, it has to be rewritten for online local optimization. In short charging period (N several sampling times), higher charging current leads to higher increase rate of SOC. In addition, the value of charging current is negative. So, the objective function is finally rewritten in a discrete form as follows:

$$J = \min_{I(k)} \sum_{k=1}^{k=N} \left(\alpha \cdot I(k) + \beta \dot{q}_{loss}^{SR}(k) \right), \tag{14}$$

where N is the control horizon.

In fact, chargers have limited capabilities that can be considered with maximum and minimum allowable currents, I_{max} and I_{min}.

$$I_{\min} \le I(k) \le I_{\max} \,. \tag{15}$$

In addition, the following three constraints are introduced to prevent operations out of safe range by limiting the maximum SOC, terminal voltage and surface concentration:

$$SOC(k) \le SOC_{\max} \,, \tag{16}$$

$$V(k) \le V_{\max}, \tag{17}$$

$$c_{s,surf}^{-} \le c_{s,\max}^{-}, \tag{18}$$

The constraint (16) is used as the condition for stopping charging. Constraint (17) enforces to avoid overcharge and constraint (18) prevents the anode particles from being oversaturated. Since the ion concentration of the particles next to the separator becomes higher during charging process, only this ion concentration is used as the constraint obtained by the reference[66].

The formulated optimal control problem can be solved by different techniques such as Sequential Quadratic Programming (SQP), Interior-Point Methods, Genetic Algorithm and others. SQP is one of the most efficient methods used for nonlinearly constrained optimization problems because of the excellent performance in robustness and constraint handling [67]. Therefore, SQP is generally computational intensive, but is selected because of the limited number of constraints considered in this research.

The model equations are implemented in Matlab and the build-in function "*fmincon"* with SQP algorithm is used to solve the problem, which provides an optimal charging protocols.

3.3.1.2 Simulation results

The prediction horizon is set to be equal to the control horizon that is tuned to make a tradeoff between control performance and computation time. When N is equal to be 5, all constraints are satisfied and the maximum and average time required to solve the optimization problem are 0.5s and 0.064s, respectively, by a desktop computer with a 3.10 GHz processor. So, it is decided to be 5. Considering the running time of LabVIEW code in test station, the sampling time interval is chosen as Δt=1s, which allows for the implementation of the designed charging

method in real time. The minimum charging current I_{min} is set to be 5C. It is noted that the sign of current during charging is negative based on the definition of direction of current. The weighting factor α is set to be constant and equal to 1, while the weighting factor β is varied to get different charging protocols.

The charging performances consisting of charging time and degradation speed are traded off and optimized by varying the weighting factors. The simulated results including charging protocols, output terminal voltages, side reaction rates and surface ion concentrations are plotted in Figure 38~Figure 41 with black dashed lines that indicate the constraints of maximum charging current, cutoff voltage and $c_{s,\max}^{-}$. As shown in Figure 38, Figure 39 and Figure 41, all constraints are satisfied. When β=0, the penalty on the side reaction rate is not imposed. Therefore, the optimized charging method achieves the shortest charging time. The charging operation starts from the maximum allowed charging current limited by the constraint of charging current until the constraint of surface ion concentration becomes active. When the constraint of surface ion concentration becomes active, the charging current starts to decrease and the surface ion concentration of particles next to the separator is kept as constant. In addition, when the terminal voltage reaches the cutoff voltage, the constraint of terminal voltage becomes active and the battery is charged in CV mode.

In the previous designed FC method [66], the charging current is limited by the preset value of surface ion concentration, so resting is needed to limit the surface ion concentration below the maximum allowed saturation concentration. However, the constraint of the surface ion concentration is still kept although resting is not considered because NMPC decides the charging current based on prediction with prediction horizon N.

With β increases, more penalty is imposed on side reaction rate, which decreases the amplitude of charging current. When β increases to 25000, it takes 62min to fully charge the battery, while total ion loss is much lower. The effects of weighting factor on charging time and ion loss are shown in Figure 42 and Figure 43.

When β is less than 10000, charging times at different SOC intervals are not significantly affected by the change of β, but ion loss significantly decreases with the increased β. When β is larger than 10000, the charging time significantly increases with increased β, while the ion loss does not significantly decrease. Therefore, the weighting factors are set as α=1 and β=10000. However, β can be adapted dependent upon some charging conditions. If EVs should be charged at night, a large value of β can be used to continuously decrease the ion loss.

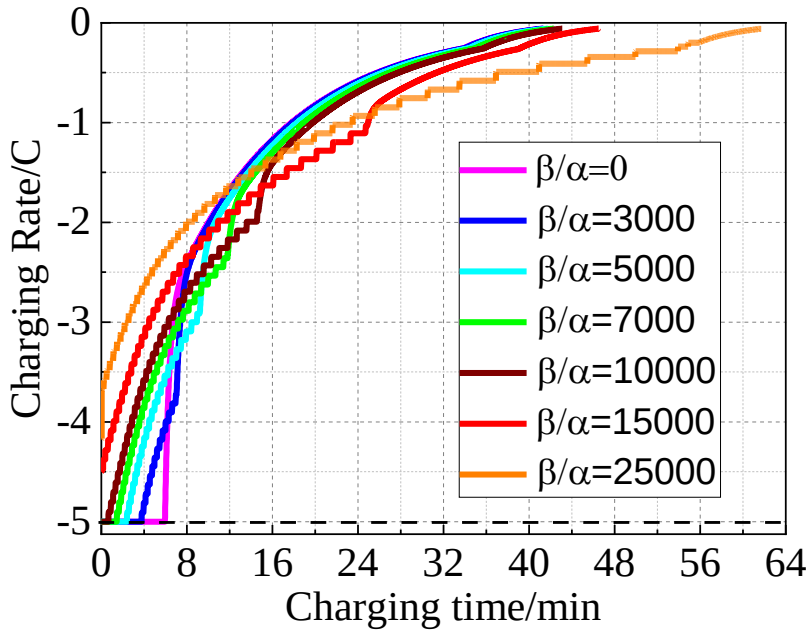

Figure 38. Optimal FC protocols at different weighting factors (sim).

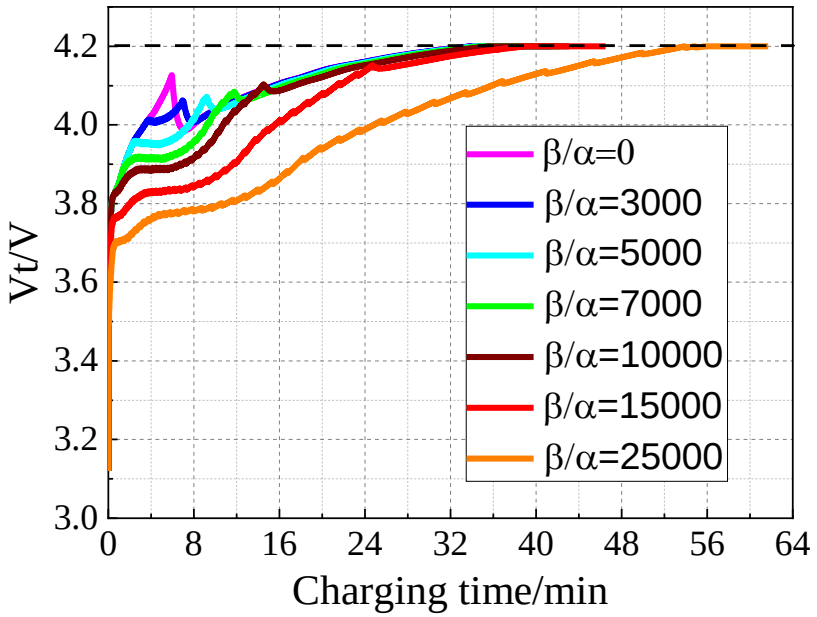

Figure 39. Output voltages at different weighting factors (sim).

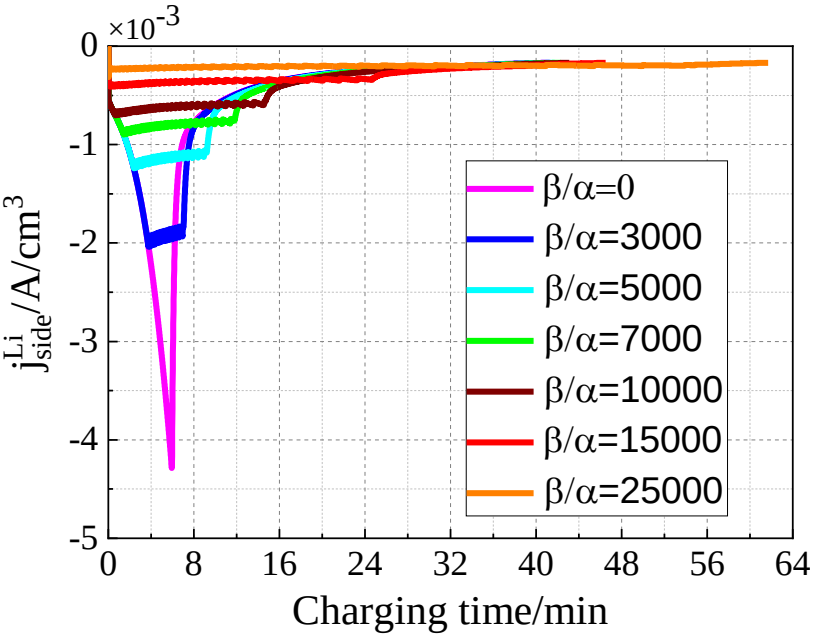

Figure 40. Side reaction rates at different weighting factors (sim).

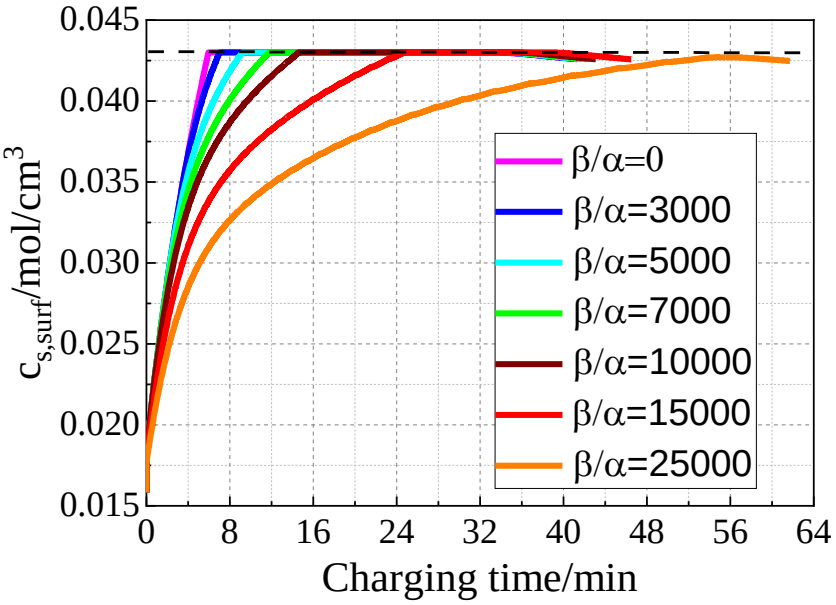

Figure 41. Surface ion concentrations at different weighting factors (sim).

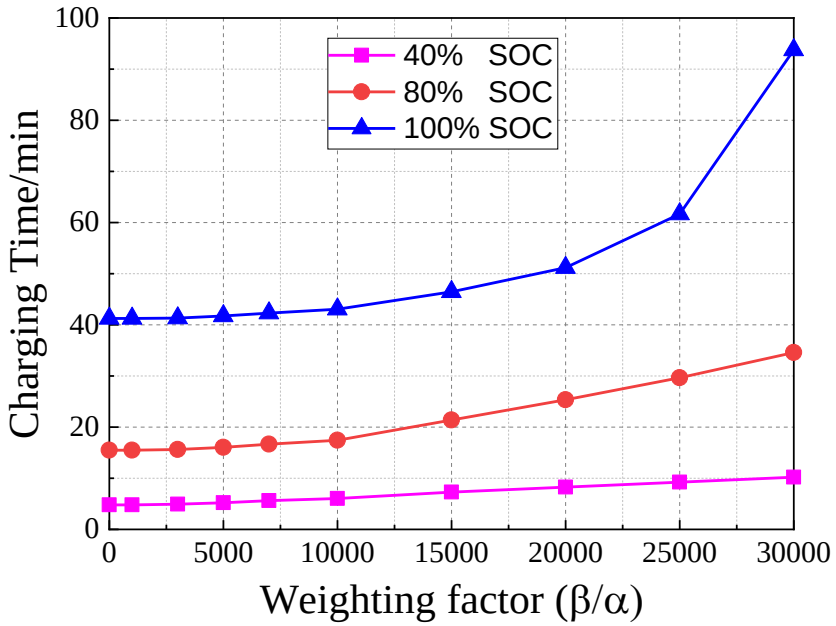

Figure 42. Effects of weighting factors on the charging time at different SOC intervals (sim).

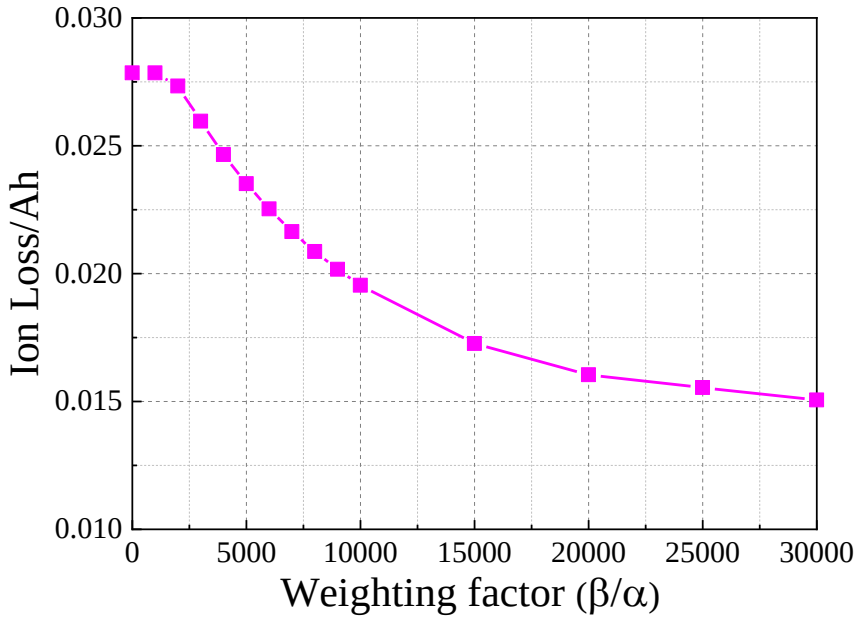

Figure 43. Effects of weighting factors on consumed lithium ions by side reaction (sim).

3.3.2 Pulse discharging to promote lithium stripping

The previous theoretical analysis by simulation assumes that no lithium plating takes place. However, according to the results shown in Figure 35 and Figure 36, lithium plating is the severe cause for degradation, particularly during high charging currents. The ions in the plated lithium can be recovered by pulse discharging current that promotes lithium stripping. The cycling test results as shown in Figure 35 reveals that pulse discharging current is capable of significantly recovering the ions in the plated lithium. As a result, the capacity fades by 14% less than that by CC charging. Therefore, adding extra pulse discharging currents in the charging protocol allows for minimization of degradation without increasing extra charging time. The magnitude and frequency of the pulse discharging current are 2C and 20mHz [58][68].

Finally, the new FC method is born by combining the optimal FC charging protocol and pulse discharging currents, which is called the optimal FC with pulse discharging currents (OFCPD).

Possibly, the pulse charging currents can be used during all the charging process until the battery is fully charged. In fact, lithium plating is favorably formed when the lithium plating overpotential, given by equation (11) becomes negative. Thus, the pulse discharging current is only considered during this favorite condition. For simplicity, the lithium plating overpotential can be simply replaced by anode potential, which is given as $\varphi_{s-} - \varphi_{e-}$.

When a battery is being charged, the requested SOC is one of the conditions that stop charging. A flowchart for the designed charging method is depicted in Figure 44. At the beginning, the initialization is finished, which includes the update of battery parameters using the degradation model and estimation of initial SOC. After initialization, the charging starts. Based on the measurement of current and voltage, the states of the battery are updated and then a charging current is determined by the NMPC. After the battery has been charged for 50s, if the anode potential is less than 0V, 2C discharging current is applied to the battery for 5s. The above process is repeated until the conditions of stopping charging are fulfilled. The simulation results for the fresh cell are shown in Figure 45, which includes the current, terminal voltage, surface ion concentration and anode potential. The constraints for the surface ion concentration and terminal voltage are satisfied. The pulse discharging currents are only considered when the anode potential is negative.

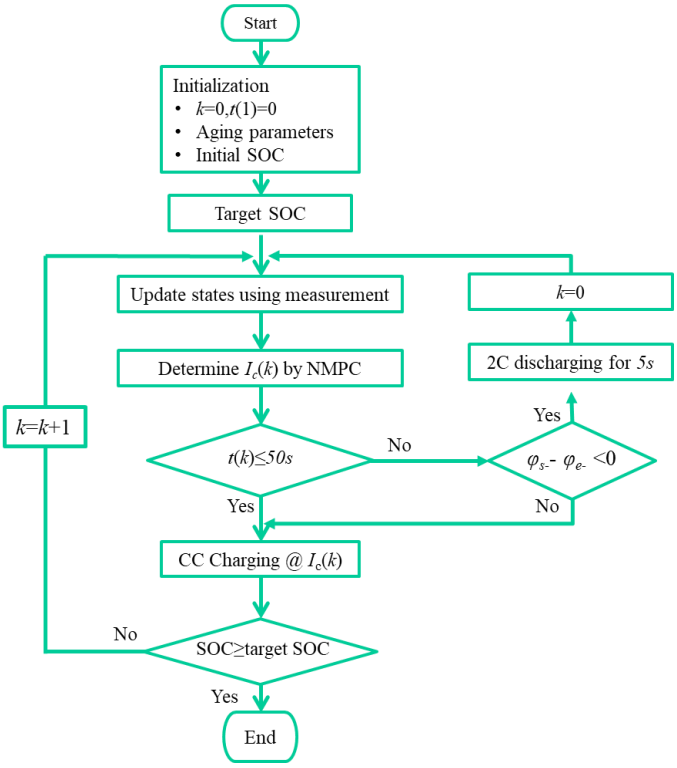

Figure 44. Flow chart for the proposed charging method (OFCPD).

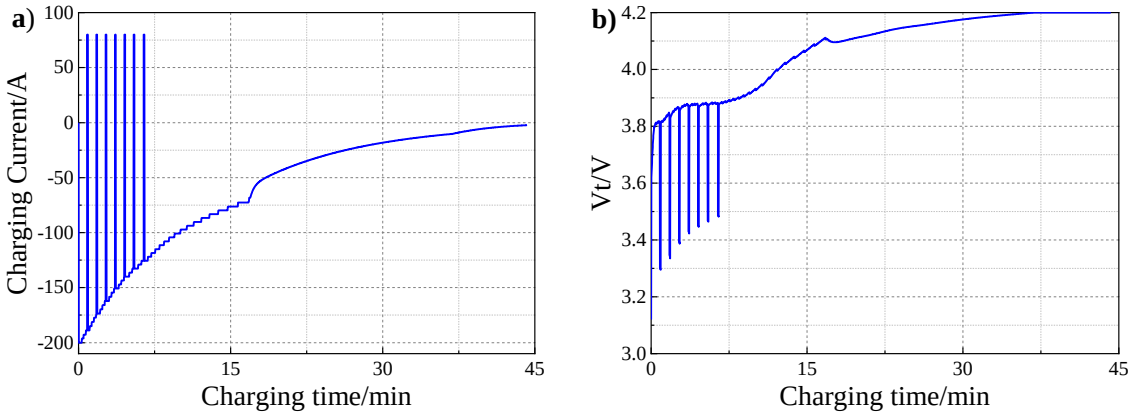

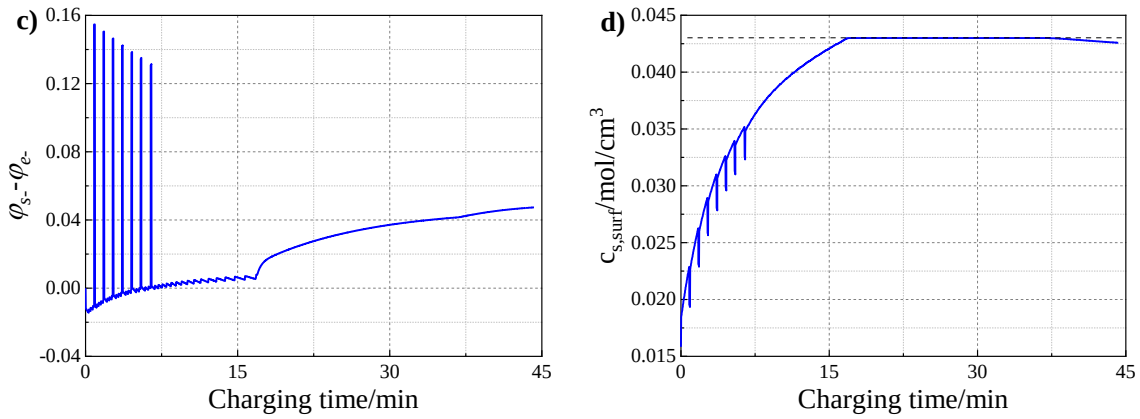

Figure 45. Simulation results of proposed charging method (OFCPD). a) charging current; b) terminal voltage; c) anode potential; d) surface ion concentration.

3.3.3 Experimental results and analysis

The optimal charging protocol was implemented and experimentally evaluated using BIL system that runs in real time. The proposed charging method includes the ROM with SPKF and NMPC coded with Matlab, which is integrated into LabVIEW using a MATLAB script. The battery was placed in a designed thermostat system that dynamically rejects the heat generated by the battery, so the battery temperature was kept to be constant.

The charging time and capacity fade of the proposed method are compared with those of CC/CV charging at 1C, 2C, 2.7C and 3C. The charging protocols up to 100% SOC and their charging time and capacities from experiments are shown in Figure 46, Figure 47 and Figure 48. Compared with the 1C CC/CV charging protocol, the other charging protocols can reduce the charging time by more than half in low and middle SOC ranges but accelerate the capacity fade. In the high SOC range, the OFCPD cannot reduce the charging time further because the charging current is limited by the constraints of surface ion concentration and cutoff voltage. Charging time

by OFCPD up to 40% SOC becomes less than 48% than that by 2C CC/CV and 21% less than that by 3C CC/CV because of the high charging current at low SOC range. When charging up to 80% SOC, the charging time by OFCPD becomes 25% less than that by 2C CC/CV charging. The capacity fade of OFCPD protocol is the closest to that of 2C CC/CV charging until 160 cycles. But after 160 cycles, the capacity fade of OFCPD protocol becomes slower than that of 2C CC/CV charging. The charging time up to 80% SOC by OFCPD is larger than that by 3C CC/CV charging and the same as that by 2.7C CC/CV charging, but capacity fade is significantly reduced.

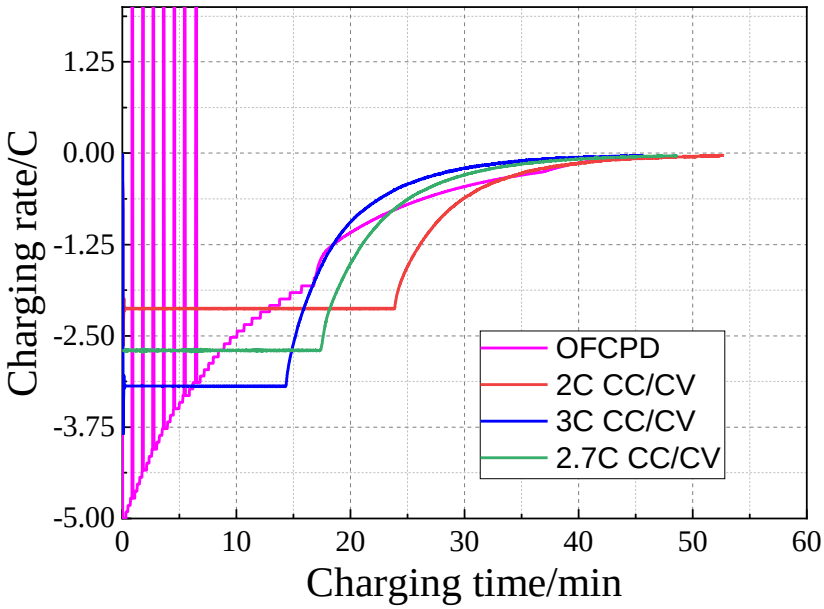

Figure 46. Comparison of different charging protocols (exp).

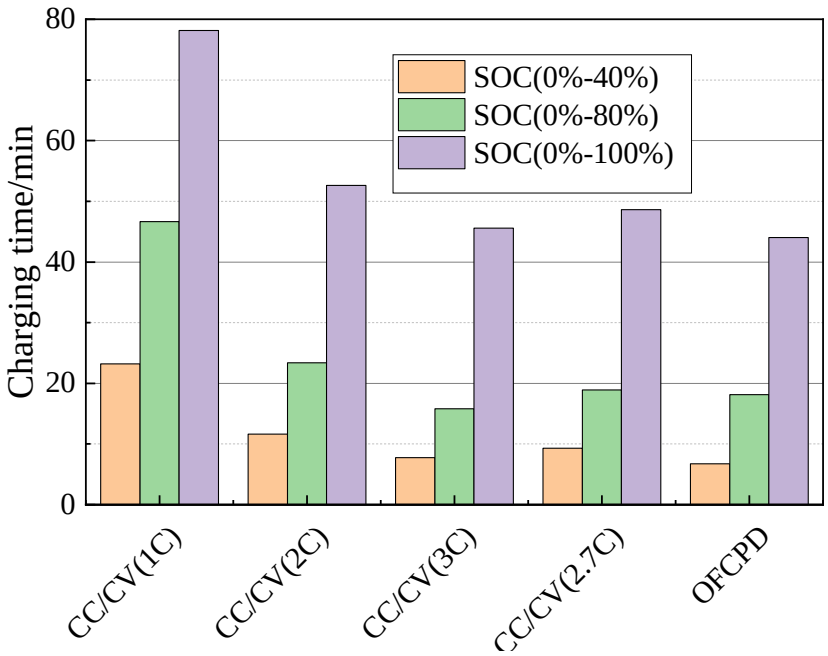

Figure 47. Charging time of different charging protocols (exp).

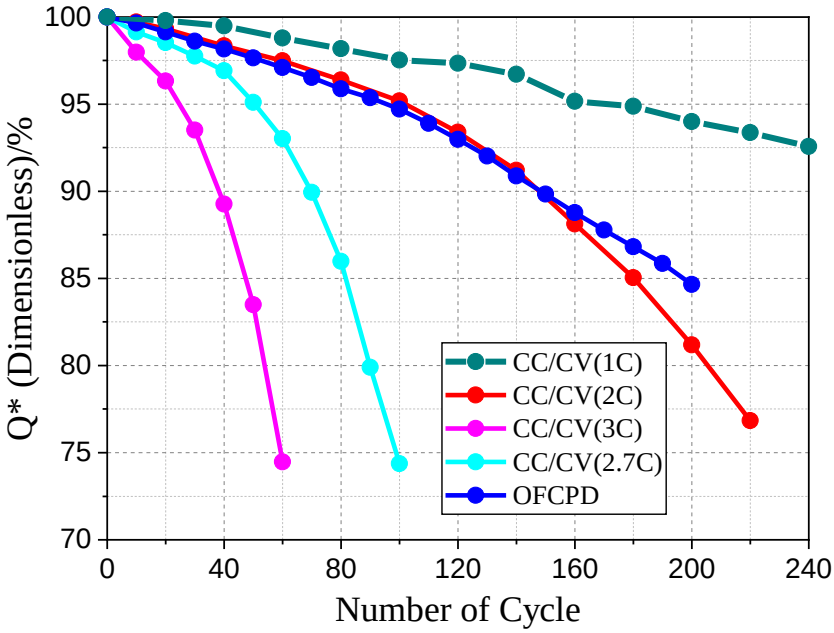

Figure 48. Capacity fade of different charging protocols (exp)

3.4 Conclusion

A fast charging method is designed based on ROM-P2D+SPM with degradation submodels along with nonlinear Kalman filter and then optimized using NMPC considering constraints, which allows for significant reduction of charging time and suppression of degradation effects. The optimization of the charging protocol was carried out by considering the objective function where the charging time and ion loss caused by side reaction were traded off by varying weighting factors. In addition, pulse discharging currents were added to the charging protocol in order to recover ions out of the plated lithium. The experimental results have shown that the proposed charging method (OFCPD) significantly reduces the charging time and the capacity loss compared with CC/CV charging.

Major accomplishments are summarized as follows;

- Development of new hybrid ROM (ROM-P2D+SPM) considering computational time and degradation effects.
- Optimization of charging protocol using NMPC under consideration of the charging time and ion loss.
- Inclusion of pulse discharging currents to recover the ions out of the plated lithium.
- Experimental verification of the protocol in BIL test station.
- Reduction of charging time and extension of cycle life.

Compared with 2C CC/CV charging, the charging time is reduced 32% and 25% up to 80% and 100% SOC respectively and the capacity fade becomes less after 160 cycles.

Chapter 4 Optimal FC method considering side reaction and lithium plating at varying temperatures

4.1 Literature review

During charging, degradation of LiB is mainly caused by side reaction and lithium plating [29][33], which are further governed by charging current and battery temperature.

Side reaction is accelerated when the battery is operated at the working conditions of high charging current and elevated temperatures. At high charging current, the overpotential of side reaction becomes larger, which leads to high reaction rate of side reaction according to B-V equation. In addition, increased charging current generates more heat that elevates the temperature of battery. When temperature rises, side reaction increases because of increased kinetics of lithium ions and electrolyte solvents and more ions passing through the SEI layer to the surface of particles [34].

For lithium plating, its rate is accelerated at the working condition of high charging current and low temperature. When charging battery at high currents, a large amount of lithium ions accumulate at the interface of graphite because of limited diffusion rate in solid, which leads to high concentration gradient of lithium ions at the interface of graphite [69]. If lithium ions are saturated at the interface, lithium plating is promoted. At low temperature, especially below 20^{o}C, battery has sluggish lithium ion diffusion in electrolyte and particles [70], high SEI resistance and low main reaction rate, which all drives the anode potential to drop below 0V referring to Li^{+}/Li. As a result, lithium plating is prone to occur at low temperatures[31]. Although the exchange current density of lithium plating decreases with the decreased temperature, the potential of anode

particles becomes lower with the decreased temperature, which finally leads to increase of the reaction rate of lithium plating.

Effects of charging current and temperature on degradation are usually coupled during cycling, whose correlations were experimentally analyzed in previous studies. Temperature effects on degradation show different behaviors at different ranges of applied C-rates. At low C-rate (C/5, C/40), degradation rate shows a monotonic increase from 10^{o}C to 60^{o}C, which is mainly caused by the side reaction [71]. As the C-rate increases to around 1C, similar tendency is found at high temperature range (25^{o}C~ 70^{o}C), but when the temperature decreases to be lower than 25^{o}C, the degradation rate becomes inversely related to the temperature due to the effect of lithium plating [72]. When the cell is charged to a higher C-rate (2C), lithium plating dominates the degradation at 25^{o}C, which results in a larger degradation rate than that at 45^{o}C [73]. As a result, at a given charging C-rate, there is an optimal temperature, under which the battery has the longest cycle life. In addition, the optimal temperature varies with the charging C-rate.

There are suggestions for charging method to improve the charging performances using electric equivalent circuit models (EECM) [16][49], or electrochemical models [24][27] with respect to charging time, degradation, heat generation and safety. In order to obtain the optimal charging protocols that guarantee the optimal performances of the FC method while satisfying constraints such as maximum temperature rise, cutoff voltage, researchers also proposed offline [26] [51] [74] and online [55] optimal charging methods. In these methods, the temperature effects on the degradation and safety of battery are only qualitatively analyzed and considered by limiting maximum temperature [50], or temperature rise [18] of battery. However, these methods lacks a systematic and quantitative analysis on the relationship between temperature, C-rate and degradation.

Therefore, an optimal FC method is proposed by optimizing the charging time and degradation considering the effects of temperature and C-rates on degradation. At first, the degradation model based on a ROM is validated and utilized to find the optimal temperatures at different charging C-rates. In the designed optimal FC method, NMPC is used to solve the optimal control problem and determine the charging protocol, where both the charging C-rates and temperature are controlled to vary at different SOCs, in order to reduce the reaction rates of lithium plating and side reaction.

4.2 Model development and its validation

The design of optimal FC method requires a ROM and degradation model that work at different temperatures. Some parameters in the models are temperature dependent, such as diffusion coefficient of lithium ions, resistance of SEI layer and kinetic reaction rate of side reaction. The relationships between these parameters and temperature can be expressed using the Arrhenius-type equations.

At first, the resistances of SEI layer for fresh cell at different temperatures are measured by EIS tests. And then, charging and discharging data for fresh cell at different temperatures is collected and used to tune the rest of parameters in ROM. In addition, experimental cycling data is used to obtain the parameters related to degradation. After obtaining the values of these parameters at different temperatures, the relationships between parameters and temperature are fitted and calculated using Arrhenius-type equations. Finally, simulations of cycling at different temperatures and C-rates are conducted at a series of C-rates and temperatures to determine the optimal temperatures.

4.2.1 Development and validation of the models at different temperatures

The designed models including ROM and degradation model used in this chapter are the same as those in Chapter 3. A key feature of the degradation model is that it considers both the side reaction and lithium plating. A brief summary of the model is given below and further details can be found in our previous work [33][39] [58][62].

In addition, the battery used is also the same as that in Chapter 3, which is a pouch-type battery with a capacity of 40Ah. The active materials of the anode and cathode for the battery are carbon and NMC ($Li[MnNiCo]O_2$), respectively. During testing, the temperature of the battery is controlled to be constant by a designed thermostat system that minimizes the effects of heat generated during cycling on the charging, discharging and degradation characteristics.

At first, the resistance of SEI layer is estimated with help of EIS equivalent circuit model after the impedance of the fresh cell is measured at different temperatures by EIS [3]. And then, the four other unknown parameters such as solid phase diffusion coefficients are tuned by comparing the simulation results with the experimentally collected charging and discharging data of fresh cells at different temperatures. Other parameters of the ROM for fresh cell are listed in Table 6.

Then, the experimental cycling data is collected at different charging currents and temperatures from 0% to 100% SOC, which are used to obtain the parameters related to degradation. These parameters are tuned by comparing the simulated with experimental responses. The capacities measured at 2C and 3C CC/CV charging and 1C discharging are plotted in Figure 49 and Figure 50, where the capacity is dimensionless and defined as the ratio between the

capacities of an aged cell to that of the fresh cell. The results show that the prediction error of the capacity over cycles is negligible.

After obtaining the parameters at different temperatures, the relationships between the parameters and temperatures are fitted using Arrhenius-type correlation [75];

$$\psi = \psi_{ref} \exp\left(\frac{E_{act}}{R}\left(\frac{1}{T_{ref}} - \frac{1}{T}\right)\right), \tag{19}$$

where ψ indicates a parameter, ψ_{ref} is its reference value at 25°C, E_{act} is the activation energy, R is the universal gas constant and T is the cell temperature. The reference values, and activation energy for different parameters are listed in Table 7.

Table 7. Key temperature-dependent parameters.

	Value @25°C	E_{act} (kJ/mol)
Film resistance of SEI layer, R_{SEI} (Ω/cm^2)	88.5	-5.2×10^4
Solid phase Li^+ diffusion coefficient for anode, D_S (cm^2/s)	1.3×10^{-10}	3.0×10^4
Solid phase Li^+ diffusion coefficient for cathod, D_S (cm^2/s)	3.1×10^{-10}	3.0×10^4
Kinetic rate constant for the side reaction, k_{side} (A.cm/mol)	8.21×10^{-9}	9.1×10^4
Exchange current density of lithium plating, $i_{0,Li}$ (A/cm^2)	3.39×10^{-8}	8.9×10^4

When the cell is cycled with 2C CC/CV charging at 35 and 45°C, capacity of LiB drops almost linearly until 80% of capacity of the fresh cell, which is mainly caused by the side reaction, as shown in Figure 49. However, the capacity fade at 15 and 25°C shows a nonlinear behavior, which is caused by lithium plating. The capacity drop is analyzed using the validated degradation model, where ion losses by side reaction and lithium plating are plotted in Figure 51. The loss of

ions by the side reaction increases linearly, while that by lithium plating increases with a hyperbolic function.

When the C-rate for charging increases to 3C, the capacity fade, as plotted in Figure 50 shows a similar trend at 15, 25 and 35^{o}C with a nonlinear curve. However, the capacity drop at 45^{o}C is almost linear, which indicates a minimum occurrence of lithium plating. In addition, the capacity fade with 3C CC/CV charging at 15 and 25^{o}C is larger than that at 35^{o}C because the amount of lithium plating gets decreased by the increased temperature. Compared the capacities of 3C CC/CV charging at 25 and 35^{o}C, the degradation fade is almost same until 40 cycles, but after 40 cycles, the capacity fade at 25^{o}C becomes faster than that at 35^{o}C, which can be explained by calculation of the ion loss, as shown in Figure 52. The ion loss caused by the side reaction at 25^{o}C is less than that at 35^{o}C, while that caused by lithium plating at 25^{o}C is larger than that at 35^{o}C. The difference of ion loss caused by lithium plating exponentially increases with the cycling number. During the reaction of lithium plating, the solid lithium metal deposits blocks the pores of the anode, which decreases the electrode volume fraction and then increases the overpotential of lithium plating [76]. As a result, this positive feedback results in the exponential increase of lithium plating rate with the cycling number and therefore a rapid drop of capacity.

The experimental results show that there is an optimal temperature for each charging C-rate that suppresses both causes of degradation. In order to find the optimal temperature at different C-rates, simulations using the degradation model are conducted to study the aging behaviors of LiB at various temperatures and different charging C-rates. At the simulation, only the charging behavior of battery is of interest. Thus the battery is charged to 4.2V using constant current from 0% SOC and then charged at constant voltage until the current drops below 1/30C.

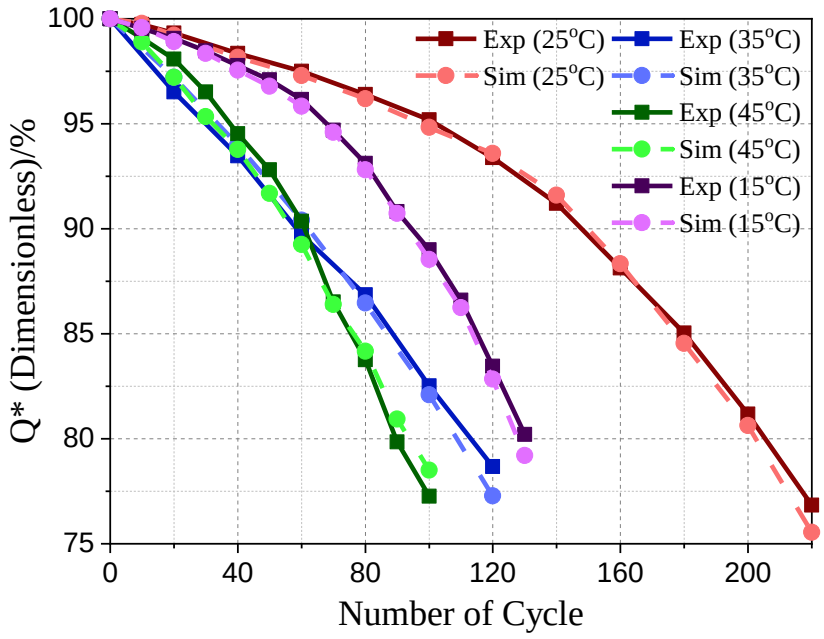

Figure 49. Comparison of measured and simulated capacities by 2C CC/CV charging at different temperatures.

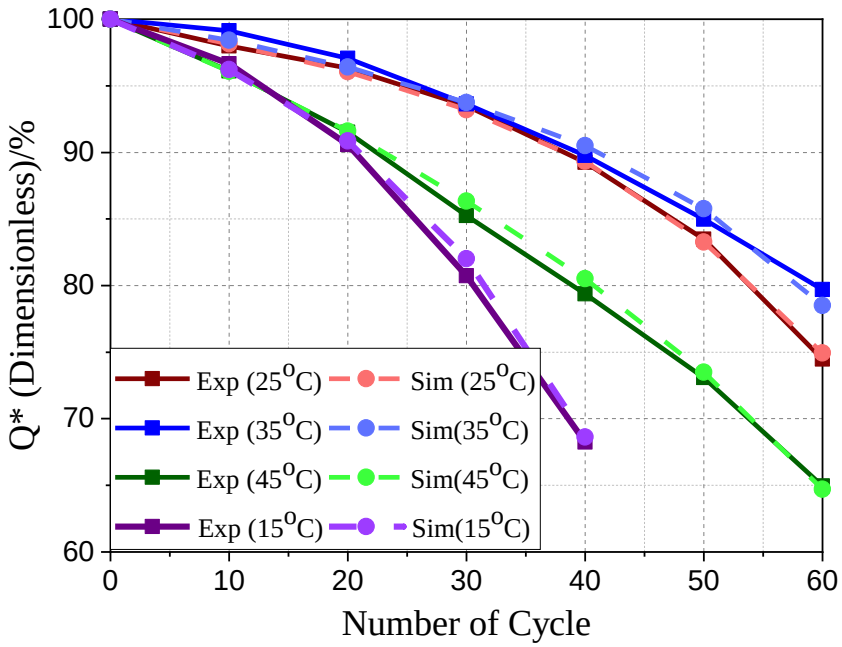

Figure 50. Comparison of measured and simulated capacities by 3C CC/CV charging at different temperatures.

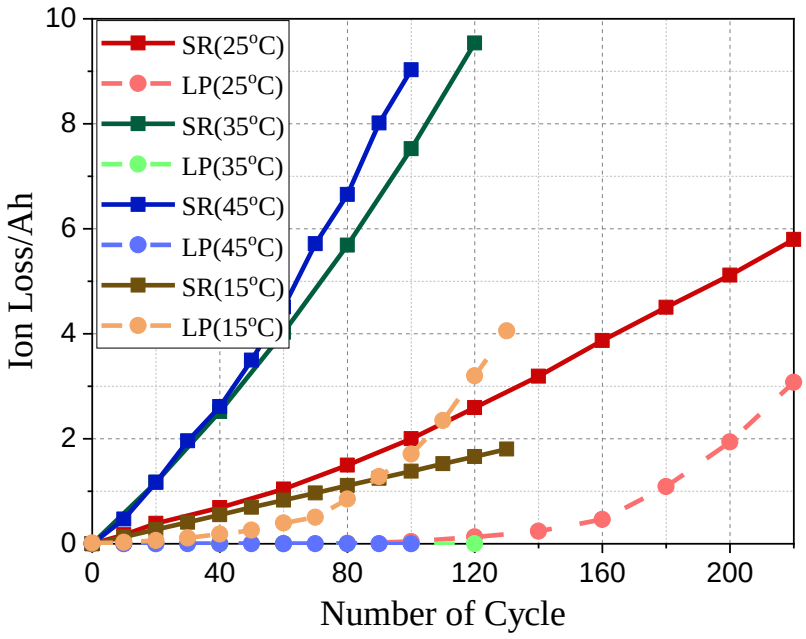

Figure 51. Ion loss by 2C CC/CV charging at different temperatures (sim).

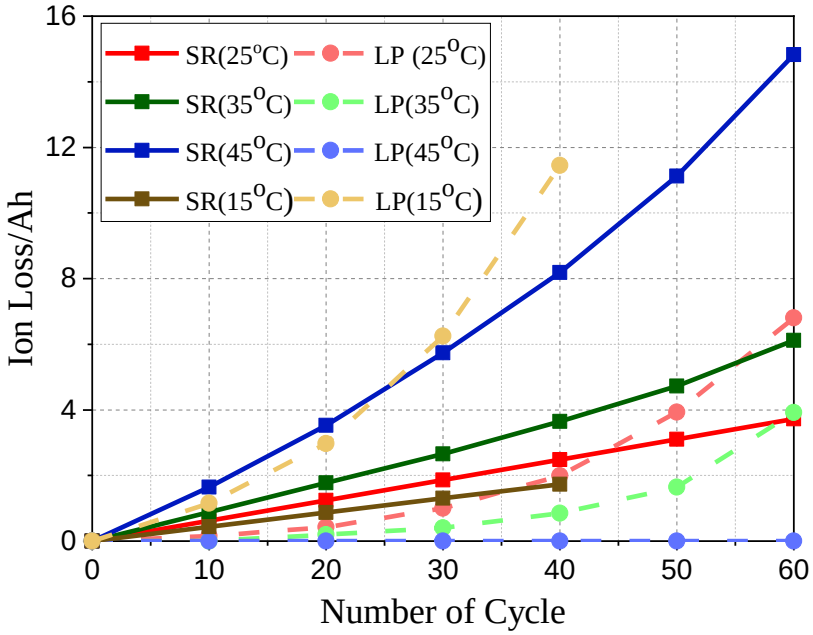

Figure 52. Ion loss by 3C CC/CV charging at different temperatures (sim).

4.2.2 Determination of optimal temperatures at different charging C-rates

Figure 53 and Figure 54 show the capacity loss caused by side reaction and lithium plating at the end of life (20% total capacity loss) with 2C and 3C charging current, respectively, where, the lithium plating occurs either at T<30^{o}C for 2C charging, or occurs at T<40^{o}C for 3C charging. The fraction of capacity loss caused by lithium plating increases when the temperature decreases. At the same temperature, lithium plating leads to more capacity loss at a higher C-rate. At 10^{o}C, about 13.6% capacity loss is caused by lithium plating at 2C, however, the value at 3C becomes 17%.

This phenomenon can be explained by the overpotential of lithium plating (or the potential of anode particles) at different temperatures shown in Figure 55 and Figure 56. During CC charging, the overpotential becomes lower with the increased SOC, which is caused by the decreased equilibrium potential. During CV discharging, the overpotential increases with the decreased charging current, although the equilibrium potential continuously decreases. When the overpotential becomes negative, the favorable condition for lithium plating is formed. The overpotential is affected by both the temperature and charging C-rate. When the temperature decreases, the potential becomes lower. As a result, the capacity loss caused by lithium plating increases with the decreased temperature. Compared with the potential of 2C and 3C at 25 and 35^{o}C, the higher charging current is, the lower becomes the potential of lithium plating. Thus, the capacity loss caused by lithium plating increases as the charging C-rate increases.

In summary, the existence of an optimal temperature with the longest cycle life is a result of the competition between side reaction and lithium plating. At higher temperatures, the rate of lithium plating becomes lower or zero because of high overpotential and the degradation speed is

mainly caused by side reaction, the rate of which increases with temperature. At low temperatures, the exchange current density of side reaction becomes small, however the decreased temperature leads to a lower overpotential, which accelerates the rate of lithium plating.

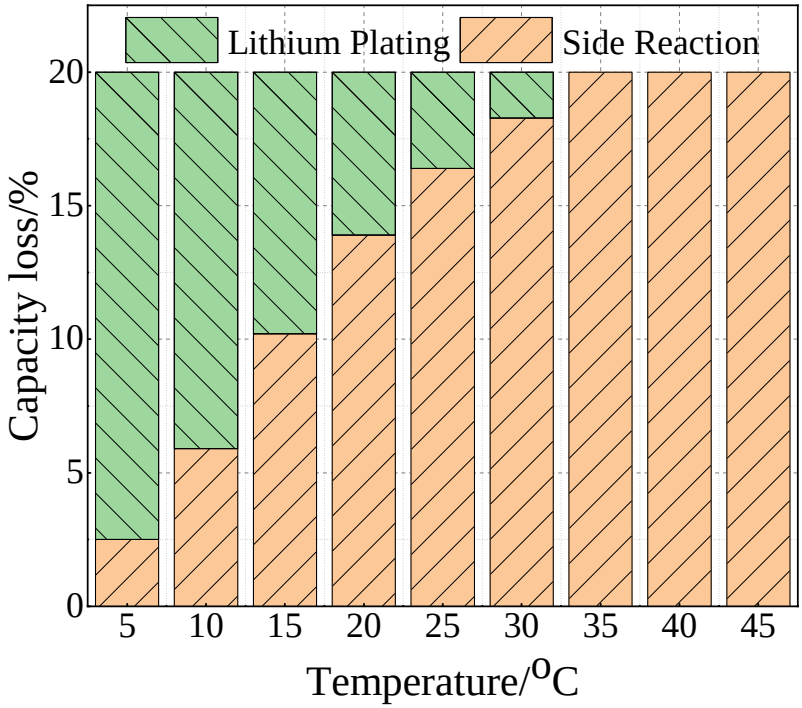

Figure 53. Capacity loss by 2C charging at the end of life (sim).

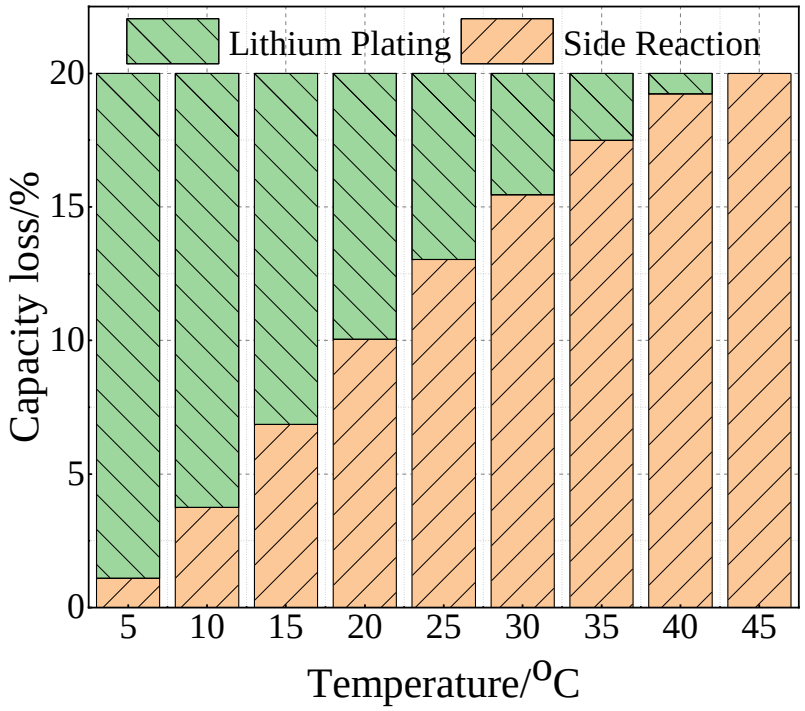

Figure 54. Capacity loss by 3C charging at the end of life (sim).

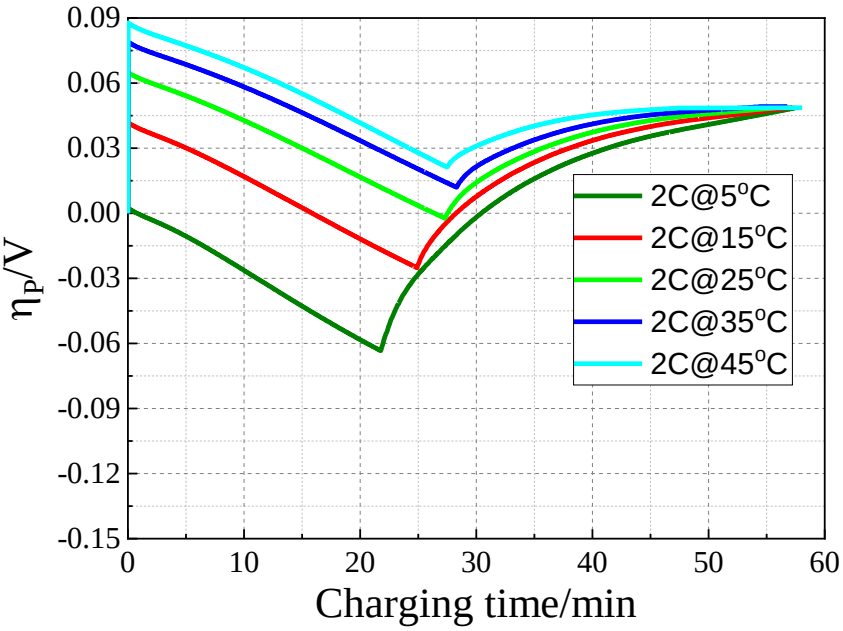

Figure 55. The overpotential of lithium plating in the charging process by 2C charging (sim).

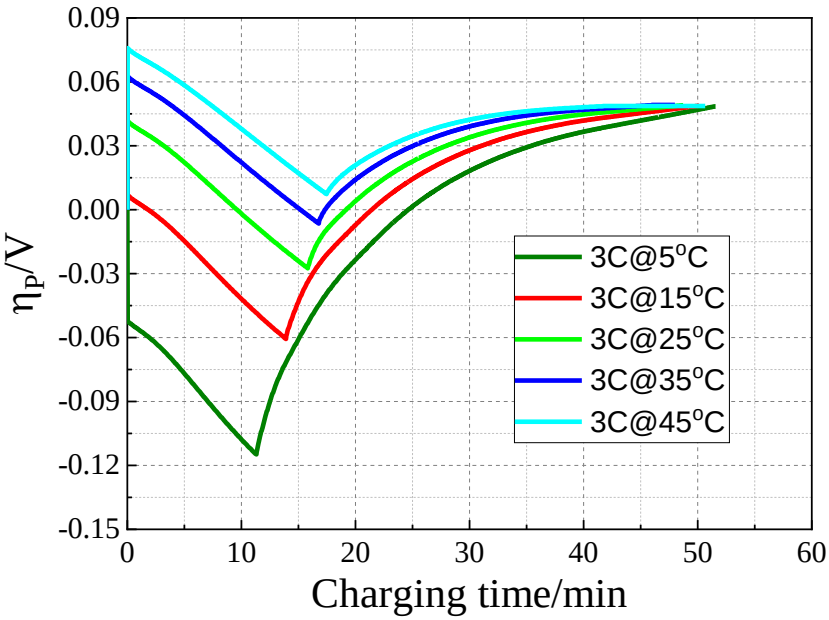

Figure 56. The overpotential of lithium plating in the charging process by 3C charging (sim).

Figure 57 shows the degradation speed vs temperature at different charging C-rates. As discussed above, the aging rate depends on the competition between side reaction and lithium plating, both of which are a function of temperature and charging C-rate. If charging time is not an important requirement (e.g. overnight charging of EVs at home), the battery can be charged using a very small charging C-rate. So, lithium plating is not significant and it is beneficial to charge the battery at lower temperatures to slow down the side reaction. However, if the charging time is demanding (e.g. charging of EVs at a charge station), the battery has to be charged at a high C-rate, which makes the lithium plating to be a major cause of degradation. So, the battery should be charged at an elevated temperature in order to suppress the lithium plating. The optimal temperatures at different charging C-rates are summarized in Figure 58. This relationship is used in the proposed FC method to change the temperature as a function of C-rate.

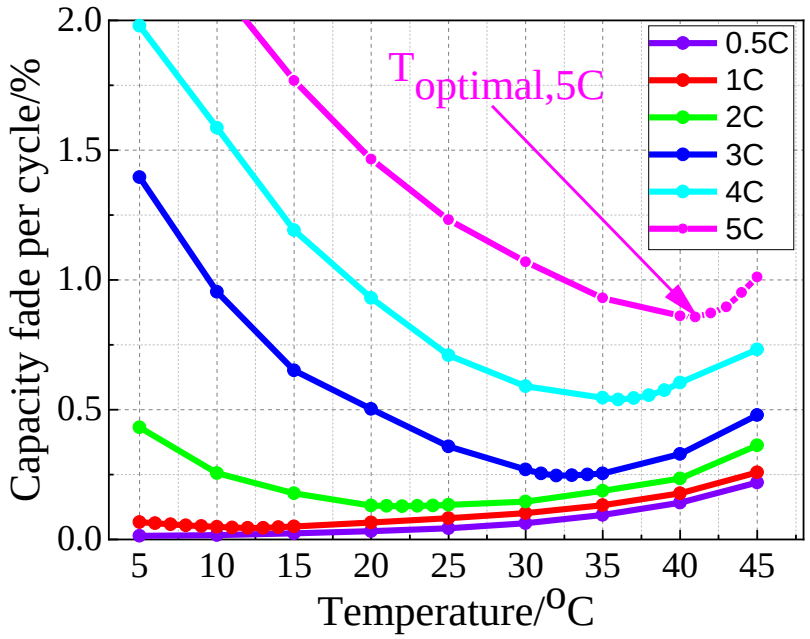

Figure 57. Comparison of aging rate vs temperature at different charging C-rates (sim).

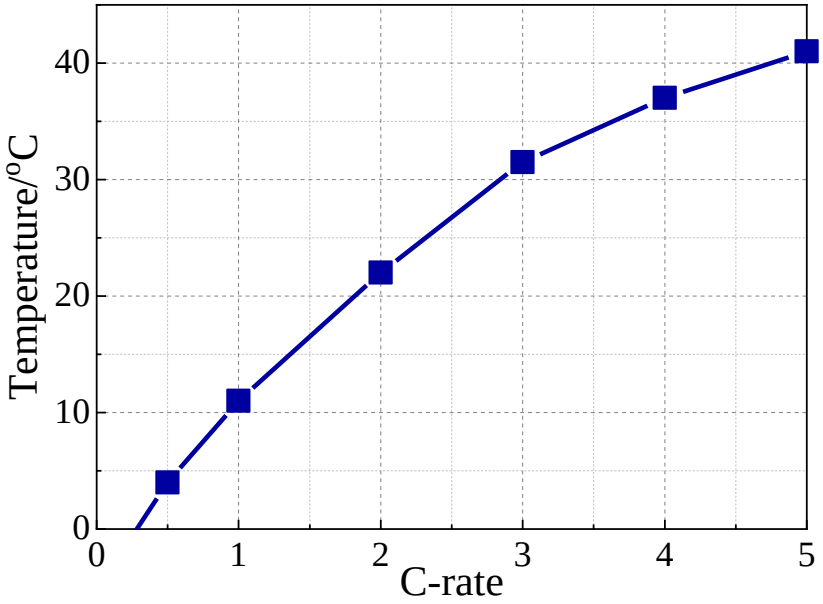

Figure 58. The optimal temperature at different charging C-rates (sim).

4.3 Design of an optimal FC method considering temperature effects

An optimal FC method is proposed that is based on the ROM with a degradation model. The model also includes effects of temperature on degradation and charging time. The ROM is used to estimate the immeasurable internal physical variables of battery such as ion concentrations, anode potential, side reaction rate, and lithium plating rate. The estimation accuracy of SOC is improved by the Sigma-Point Kalman filter (SPKF). The proposed charging method combines the optimal FC charging protocol with pulse discharging currents under consideration of temperature effects, which is called optimal FC under varying temperatures (OFC-T).

The design process of OFC-T is separated into three steps, as shown in Figure 59. In the first step, the offline optimization is carried out only considering the degradation caused by side reaction and effects of weighting factors on the design are analyzed, which results in determination of an optimal weighting factor that can be used for generating a charging protocol I. The temperature is being varied according to the curve shown in Figure 58 to continuously suppress the degradation.

In the second step, the lithium plating is considered. Extra pulse discharging current is added to the charging protocol I to promote the lithium stripping. The pulse amplitude and frequency are optimized in order to reduce the total discharging capacity while making sure that the plated lithium is completely recovered. In order to optimize the pulse discharging current, the control horizon of NMPC has to be larger than 20, which cannot be finished in one sampling time. Therefore, the optimization is carried out offline.

In the last step, the final charging protocol is decided by online optimization based on previous steps. The objective function, constraints and method to solve the optimal control

problem in this step are same as these in the first step using the tuned weighting factors. Only the charging current is optimized, while the discharging current is determined according to the results provided in the second step. With feedback of measured voltage and temperature, the generation of charging protocol is more accurate and optimal performances for the FC method is guaranteed.

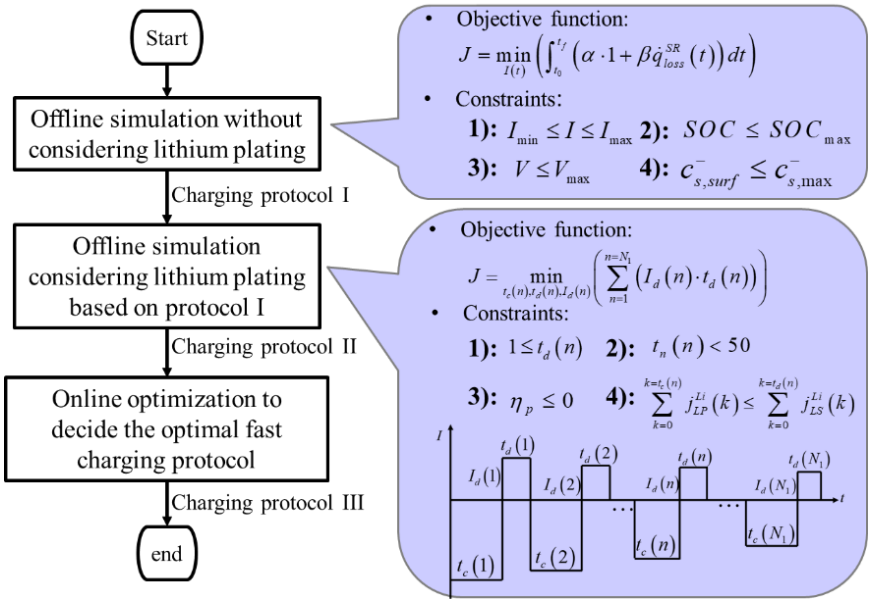

Figure 59. Flow chart to determine the optimal FC protocol.

4.3.1 Design of optimal FC method consider side reaction

Optimization of the charging protocol is performed using NMPC under the constraints of terminal voltage, temperature and internal variables. The terminal voltage and temperature can be measured directly, while the internal variables such as SOC and ion concentration are obtained from the ROM, whose errors are corrected by the SPKF. The block diagram for the concept is depicted in Figure 60. When a target SOC is set as the objective at a time step *k*, NMPC predicts states and outputs of the plant over the prediction horizon *N* and then determines the charging current as control efforts over the control horizon *N*. This is accomplished by solving an open-loop

optimal control problem that minimizes the objective function. In order to simplify the design of optimal charging method, the control horizon is assumed to be equal to the prediction horizon [65]. The first part of the optimal charging current, $I^*(k)$ is applied to the battery for charging. The optimal temperature is determined according to the curve shown in Figure 58 by interpolation using $I^*(k)$ as the input. At the next time step, k+1, the states are updated based on the measured terminal voltage. Then, the whole procedure for prediction and optimization is repeated.

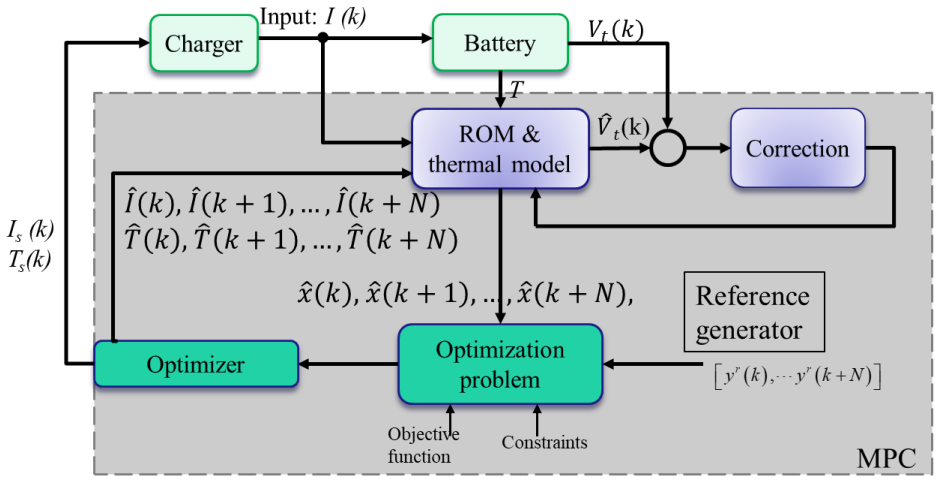

Figure 60. Schematic block diagram of proposed optimal charging method.

The optimal charging problem is formulated with the objective function given by

$$J = \min_{I(k)} \sum_{k=1}^{k=N} \left(\alpha \cdot I(k) + \beta \dot{q}_{loss}^{SR}(k) \right), \tag{20}$$

where α and β are the weighting factors that adjust the trade-off between fast charging and aging processes. N is the control horizon. $\dot{q}_{loss}^{SR}$ is the rate of ion loss over the volume of the composite anode, which is calculated using

$$\dot{q}_{loss}^{SR}(k) = \int_{x=0}^{\delta_-} \left(\left| j_{side}^{Li}(l,k) \right| \right) A dl \,. \tag{21}$$

The constraints for input, states and output as follows:

$$I_{\min} \le I(k) \le I_{\max}, \tag{22}$$

$$SOC(k) \le SOC_{\max}, \tag{23}$$

$$V(k) \le V_{\max}, \tag{24}$$

$$c_{s,surf}^{-} \le c_{s,\max}^{-}. \tag{25}$$

The $SOC_{\max}$ is the constraint to stop chargin. The $c_{s,\max}^{-}$ is the maximum allowed surface ion concentration that prevents the oversaturation at anode particles next to the separator [66]. The optimal control problem is solved using the Sequential Quadratic Programming (SQP) due to its excellent performance in robustness and constraint handling [67].

The proposed method was simulated in a desktop computer with a 3.10 GHz processor to find out the optimal control horizon and weighting factors at different temperatures. By comparison of the control performance and computation time, the control horizon was decided to be 5, which requires the maximum and average time required to solve the optimization problem were 0.5s and 0.064s, respectively. For testing of the designed charging method in real-time, the sampling time interval is chosen to be Δt=1s, which allows the LabVIEW to have enough time to execute other tasks that includes controlling equipment and collecting data.

On the other hand, the charging performances consisting of degradation speed and charging time are traded off and optimized by varying the weighting factors. The simulated results including charging protocols, output terminal voltages, surface ion concentrations and reference temperatures are plotted in Figure 61~Figure 64 with black dashed lines that indicate the constraints of maximum charging current, cutoff voltage and $c_{s,\max}^{-}$. As shown in Figure 61, Figure 62 and Figure 63, all constraints are satisfied. As shown in Figure 64, the reference temperature is

varied with the charging current, where the maximum and minimum reference temperature is 38.9^{o}C and -1.5^{o}C. At high charging current, an elevated temperature is used to slow down the lithium plating rate, while at low charging current, low temperature is required to slow down the side reaction rate.

When β=0, the penalty on the side reaction rate is not imposed and the charging current is only limited by the constraints. When β increases, more penalty is imposed on side reaction, which decreases the amplitude of charging current before the constraint of surface ion concentration becomes active.

The effects of the weighting factors on charging time and ion loss are plotted in Figure 65 and Figure 66. When β is less than 7000, the charging times at different SOC intervals are not significantly affected by the change of β, but ion loss significantly decreases with the increased β. When β is larger than 7000, the charging time significantly increases with increased β, while the ion loss does not significantly decrease. Therefore, the weighting factors are set as α=1 and β=7000.

The maximum and minimum reference temperatures should be limited after considering the energy required by the cooling system. If the reference temperature is the same as the environment temperature (25^{o}C considered in this study), no energy is required by the cooling system. The higher difference between the reference and environment temperatures is, the more energy the cooling system requires to increase or decrease and keep battery temperature to the reference value. In addition, since high temperature significantly increases the side reaction, the maximum temperature should be limited. The simulation results show that the reference temperature is kept larger than 35^{o}C for only 2.7minutes. Considering energy efficiency of cooling

system [77] and effects of temperature on side reaction, the maximum temperature is set to be 35ºC.

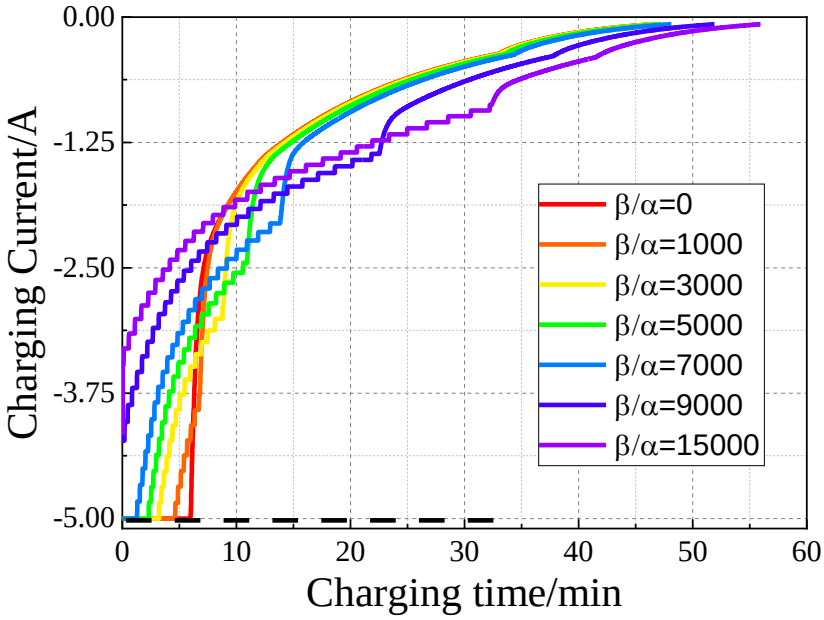

Figure 61. Optimal FC protocols at different weighting factors (sim).

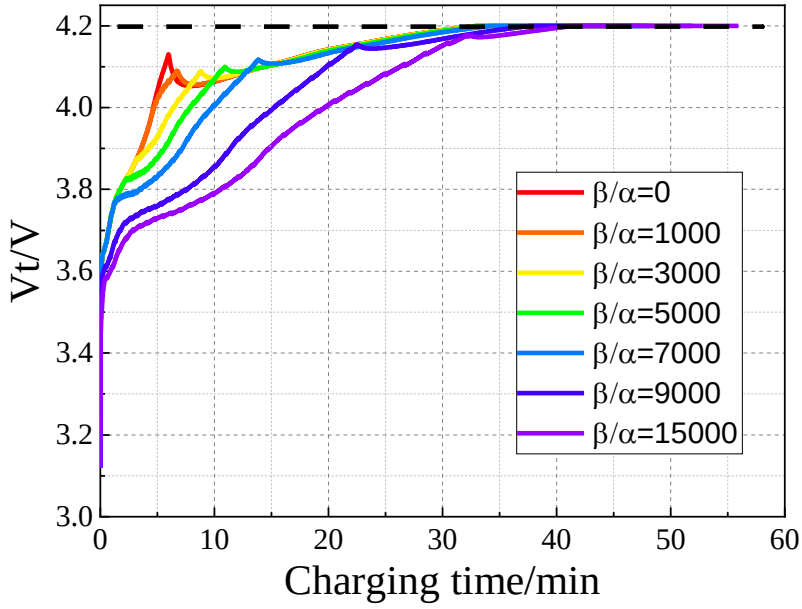

Figure 62. Output voltage at different weighting factors (sim).

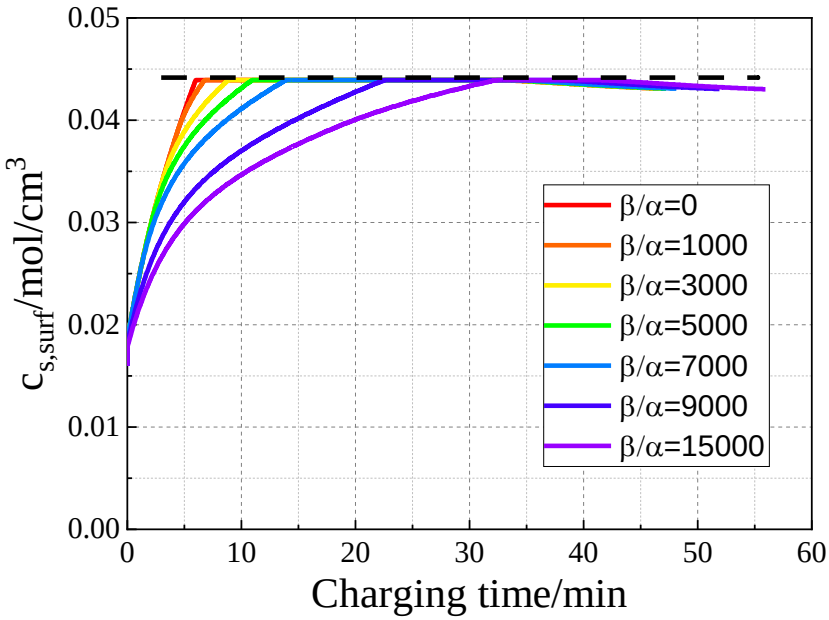

Figure 63. Surface ion concentrations at different weighting factors (sim).

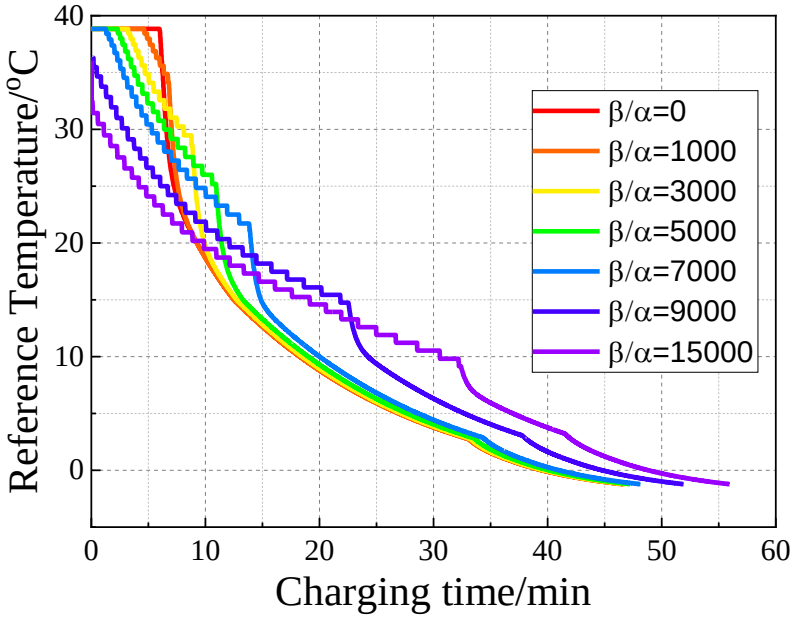

Figure 64. Reference temperatures at different weighting factors (sim).

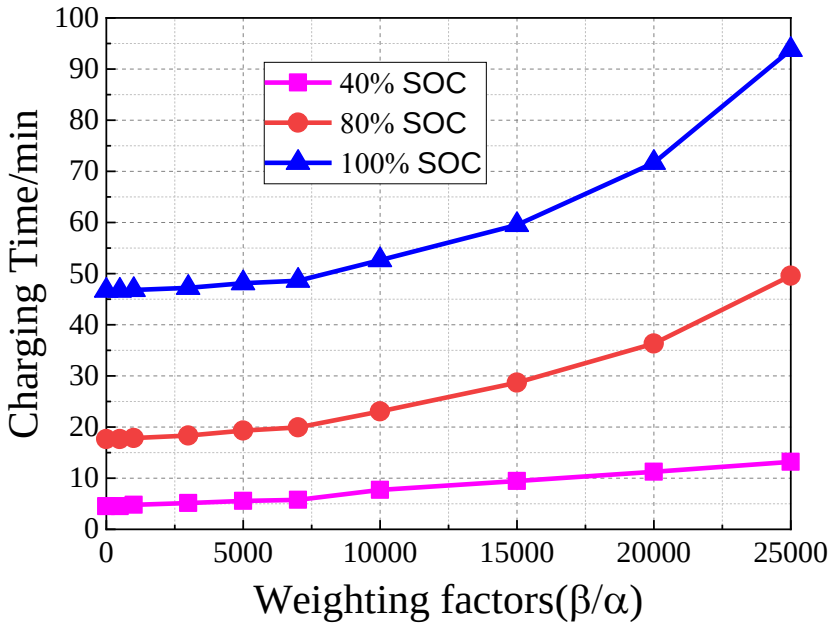

Figure 65. Charging time at different SOC intervals (sim).

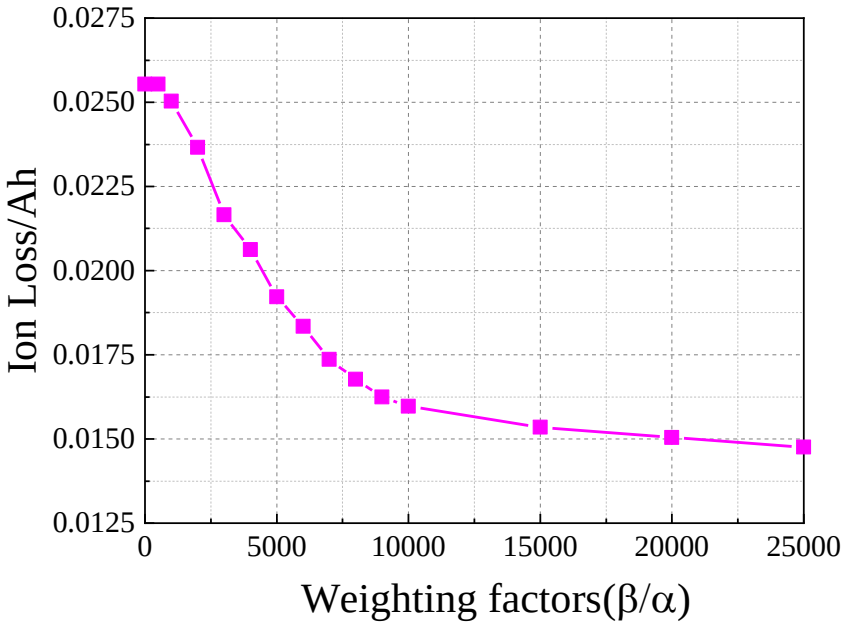

Figure 66. Consumed lithium ions by side reaction (sim).

At high SOC, the charging current becomes lower and the reference temperature also decreases to slow down the side reaction, however, the charging time becomes increased because of higher resistance of SEI layer and lower diffusion rate of lithium ion at a lower temperature. As shown in Figure 67, the ion loss becomes less at the low temperatures, but the charging time get increased. Considering the ion loss, charging time and energy required from cooling system, the minimum temperature is set to be 15^{o}C.

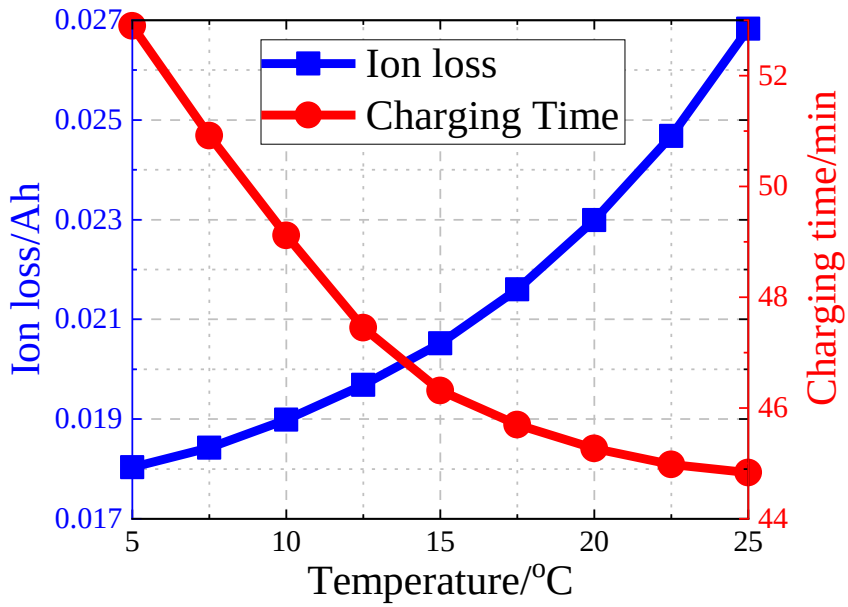

Figure 67. Effect of minimum temperature on charging time and ion loss (sim).

4.3.2 Optimization of the pulse discharging current

The pulse discharging current can promote the lithium stripping. In [58] and [68], 2C discharging current with a frequency of 20mHz is experimentally demonstrated to be the optimal. The amplitude and frequency are constant at different SOCs and the testing temperature is also constant. However, the temperature in the proposed method is varying. In addition, during CC

charging, the overpotential of lithium plating becomes lower, which leads to an increase of plating rate. So, the discharging amplitude and frequency should be optimized at different SOCs in order to better promote the lithium stripping. In this design step, the plated lithium is assumed to be recovered completely and the formation of dead lithium and secondary SEI is ignored.

The purpose of optimizing the pulse discharging current is to completely recover the plated lithium while minimizing the discharged capacity that is equal to the integral of discharging current with respective to time. The objective function, J is set by

$$J = \min_{t_c(n),t_d(n),I_d(n)} \left(\sum_{n=1}^{n=N_1} \left(I_d(n) \cdot t_d(n) \right) \right), \tag{26}$$

where $t_c(n)$ and $t_d(n)$ are the charging discharging time of the n^{th} pulse, as shown in Figure 68. $I_d(n)$ is the amplitude of the discharging current of the n^{th} pulse. N_1 is the total number of pulses.

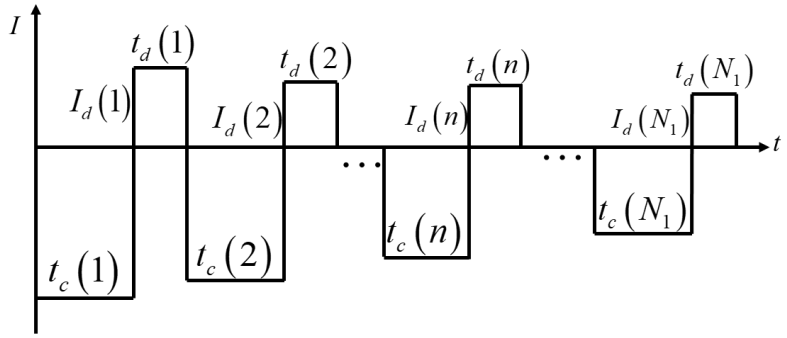

Figure 68. Timing diagram of pulse currents.

The first constraint for the optimization is the amount of the lithium ions recovered during discharging that should be larger than that of the plated lithium, which is expressed as follows;

$$\sum_{k=0}^{k=t_c(n)} j_{LP}^{Li}(m) \le \sum_{k=0}^{k=t_d(n)} j_{LS}^{Li}(m), \tag{27}$$

where m denotes the particles in anode next to the separator.

The second constraint is the minimum discharging time considering the response time of chargers that is set to 1 second;

$$1 \le t_d(n), \tag{28}$$

The third constraint is the overpotential that creates a favorable condition for lithium plating if the overpotential of lithium plating is less than 0V;

$$\eta_p \le 0. \tag{29}$$

The final fourth constraint is the maximum charging time in each pulse considering lithium plating caused by some unknown reasons (e.g. unevenly compressed electrodes [78], uneven distribution of current in the current collector [79]). That plated lithium cannot be described by the lithium plating model. In order to make sure plated lithium can be recovered by the lithium stripping, the minimum frequency should be limited. Based on the previous research [58] and [68], the frequency of 20mHz is experimentally demonstrated to be the optimal, so the constraint is given by;

$$t_c(n) < 50. \tag{30}$$

Similar to the previous case, this optimal control problem that consists of the objective function and constraints is also solved using the SQP. The simulation result of the charging protocols is plotted in Figure 69, where Figure 69 a) is zoomed in Figure 69 b). The change of frequency can be explained with the help of Figure 55 and Figure 56. During CC charging, the absolute value of overpotential of lithium plating increases, which leads to a larger lithium plating rate, so the frequency increases during CC charging at 200A. However, when the charging current decreases, the absolute value of overpotential of lithium plating becomes smaller, which leads to a smaller lithium plating rate. Thus, the frequency becomes smaller at lower charging current. The

total discharging time is 65s and the total charging time required to fully charge the battery is about 2856s, so the total charging time is not significantly affected by the introducing pulse discharging.

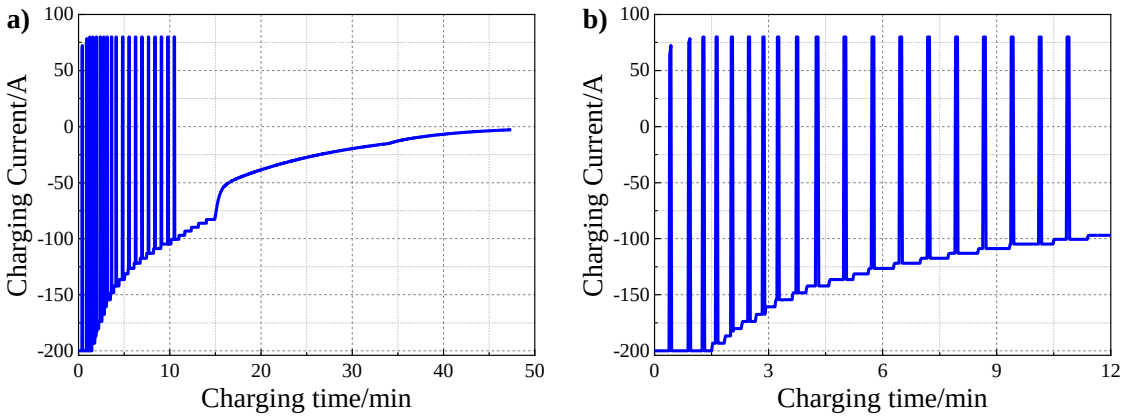

Figure 69. a) Optimal charging protocol with pulse discharging current (sim). b) Zoom-in plot of optimal charging protocol.

4.3.3 Experimental test and results

After the amplitude and frequency of pulse discharging current are determined, the determined t_c, t_d and I_d are stored in the charging system and will be used to decide the startup time, the time period and the amplitude of discharging current. A flowchart for the designed charging method is depicted in Figure 70. At first, the initialization is finished, which includes update of aging parameters based on previous cycling data and estimation of initial SOC. When a target SOC is entered, a charging process starts. Based on the measured current and voltage, the states of the model are updated and then a charging current, $I_c(k)$, is determined by the NMPC, which is used to charge the battery until next sampling time. The charging process is repeated until the end of this charging pulse ($t(k) \leq t_c(n)$). If $t(k) > t_c(n)$ and the overpotential of lithium plating, η_p is less than 0V, the battery is discharged using current $I_d(n)$ for $t_d(n)$. After discharging, the pulse

including charging and discharging is finished and then the charging in next pulse starts. All the procedure is repeated until battery SOC is larger than the target SOC.

The proposed charging method was implemented and experimentally evaluated using the BIL system that runs in real-time. The algorithm consists of ROM with SPKF and NMPC coded with MATLAB that is integrated into LabVIEW using a MATLAB script. The temperature for battery is controlled by the thermostat system that is designed with two thermoelectric modules (TEMs). Its tracking performance is shown in Figure 71.

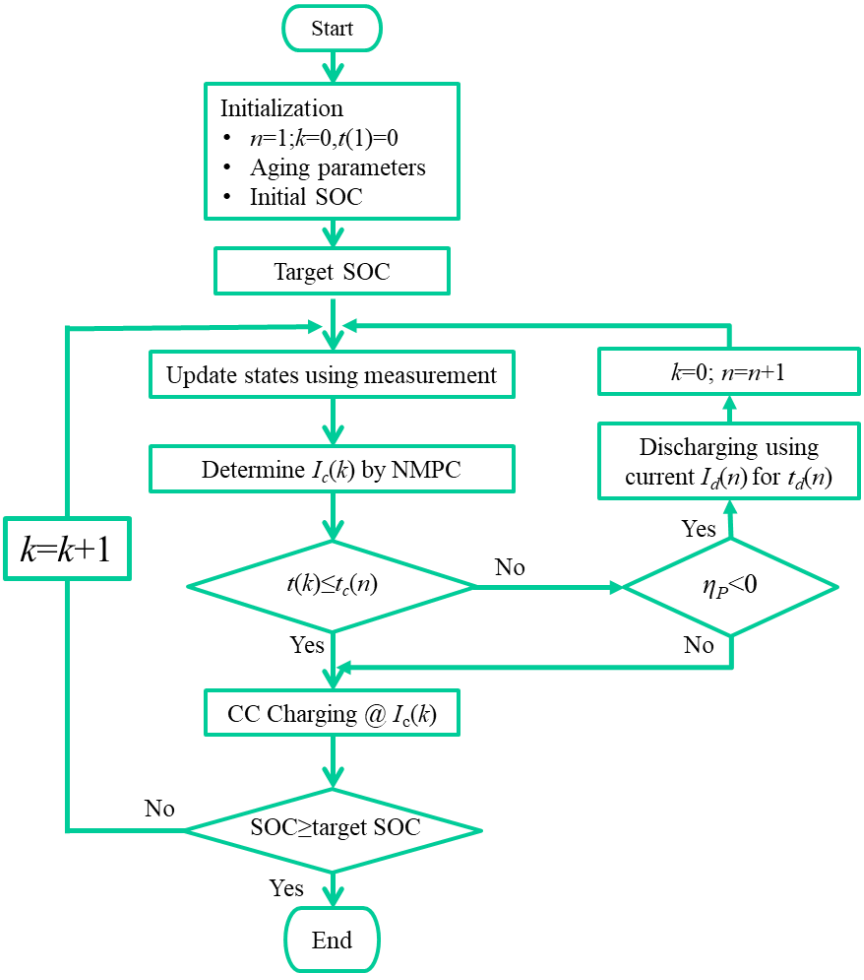

Figure 70. Flow chart for the proposed charging method.

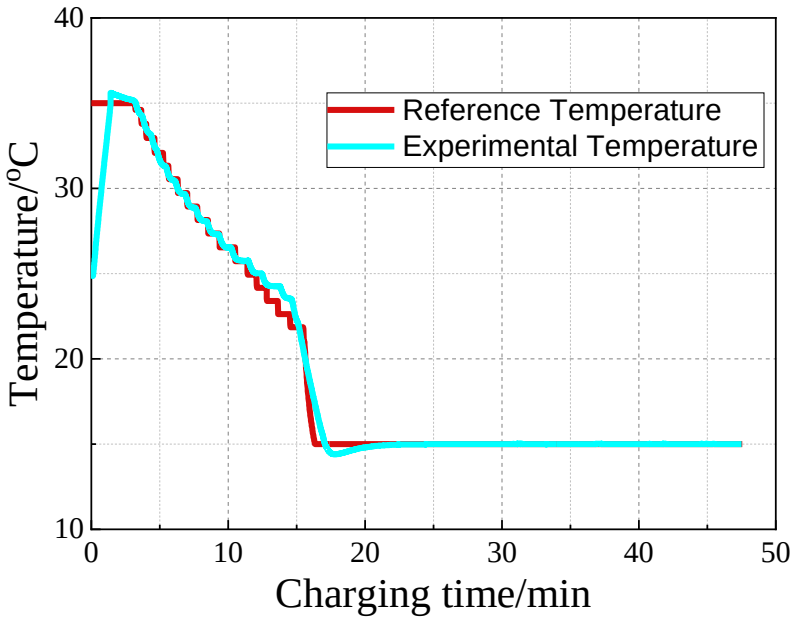

Figure 71. Tracking performance of the thermostat system.

The charging time and capacity fade of the proposed method are compared with those of CC/CV charging at 1C, 2C, 2.7C and 3C. The charging profiles up to 100% SOC and their charging time and capacities from experiments are shown in Figure 72 and Figure 73. Compared with the 1C CC/CV charging protocol, the other charging protocols can reduce the charging time by more than 50% in low and middle SOC ranges, but accelerate the capacity fade. In the high SOC range, the OFC-T cannot reduce the charging time further because the charging current is limited by the constraints of the surface ion concentration and cutoff voltage. Charging time by OFC-T up to 40% SOC becomes less than 48% than that by 2C CC/CV and 21% less than that by 3C CC/CV because of the high charging current at low SOC range. When charging up to 80% SOC, the charging time by OFC-T becomes 25% less than that by 2C CC/CV charging and is almost equal to that by 2.7C CC/CV charging, but the capacity fade is significantly reduced. Compared with

charging protocol OFCPD, the charging protocol OFC-T reduces the charging time up to 40% SOC and increases the charging time 11% and 8.14% up to 80% and 100% SOC, respectively, but the capacity loss of OFC-T is 47% less than that of OFCPD. The capacity fade of OFC-T is the closest to that of 1C CC/CV charging. The above analysis show that the design FC protocol (OFC-T) significantly reduces the charging time and degradation speed.

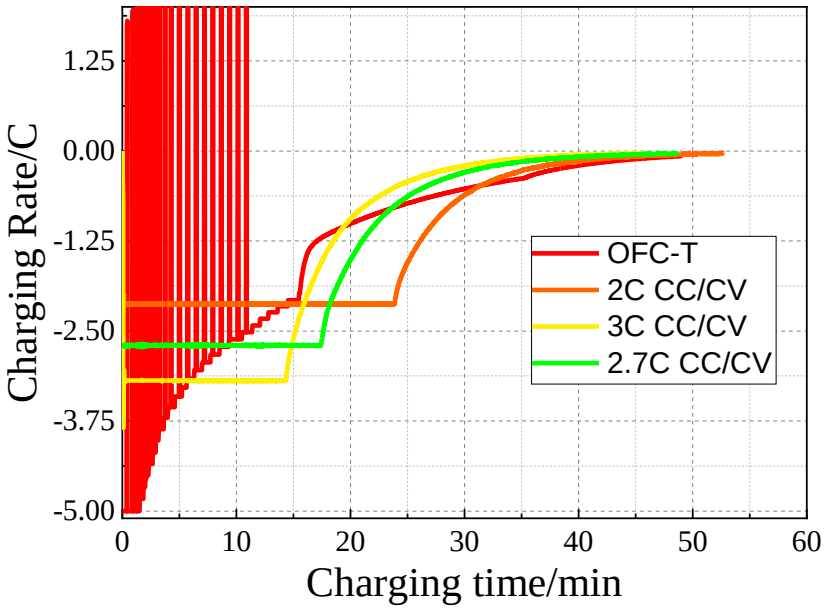

Figure 72. Comparison of different charging protocols (exp).

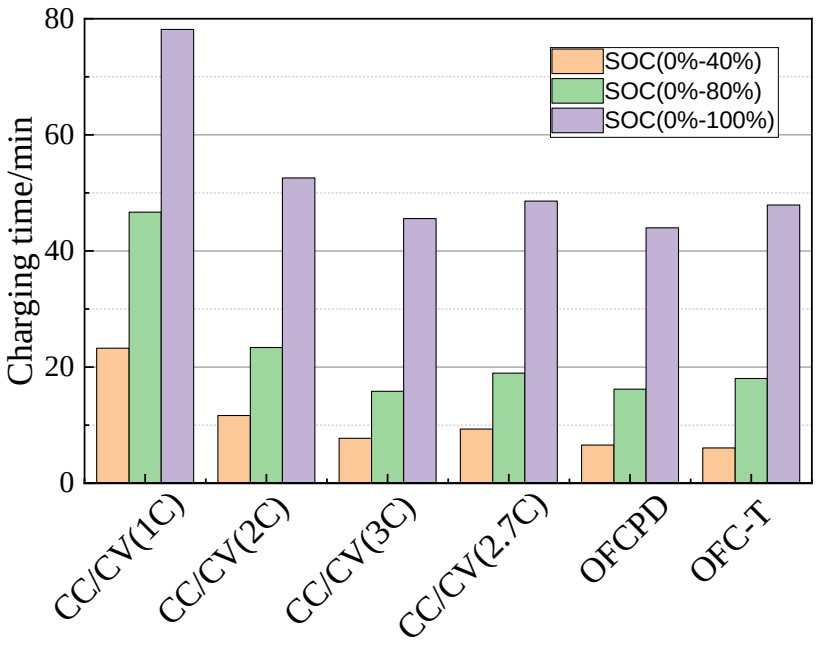

Figure 73. Charging time of different charging protocols (exp).

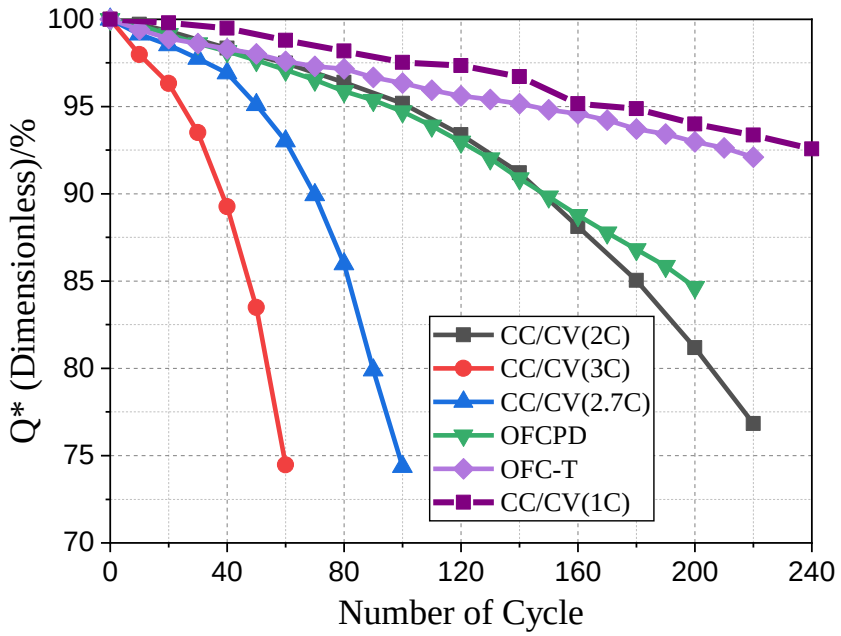

Figure 74. Capacity fade of different charging protocols (exp).

4.4 Conclusion

An optimal FC method was proposed based on a reduced electrochemical model that embeds side reaction, lithium plating and stripping as a function of temperature. The model is validated with pouch type large format lithium ion cells that have a capacity of 40Ah. Based on the validated model, the effects of C-rates and temperature on the side reaction and lithium plating are analyzed and then optimal temperatures with the longest cycling life are determined at different C-rates. The method was implemented in a BIL system, where the temperature was controlled by a designed thermostat system to track the optimal temperatures. The test results verified that the protocol can reduce the charging time without increasing the capacity fade significantly.

Here is a summary of major findings.

- There is an existence of an optimal temperature that reaches the longest cycling life. The optimal temperature depends on the competition between side reaction and lithium plating and therefore is a strong function of charging C-rate. High temperatures can slow down the lithium plating, while low temperatures reduce the reaction rate of side reaction. In addition, lithium plating rate increases with the increased charging C-rates, so the optimal temperature becomes higher at a larger C-rate.
- NMPC is used to solve the optimal control problem. In order to further reduce the ion loss caused by lithium plating, pulse discharging current are added to the FC protocol in order to promote the lithium stripping. The method significantly reduces the charging time and degradation rate compared with the 2C CC/CV charging at 25^{o}C.

Chapter 5 Conclusion and future work

This work has focused on optimal design of a FC method that minimizes the charging time and suppresses the degradation. Firstly, a FC method is proposed for the BOL based on a ROM considering side reaction. After the development of ROM, the ROM was validated against experimental data collected from fresh cells. Inaccuracy of the model and estimation of SOC were improved by EKF. The proposed charging method reduced the ion loss caused by side reaction by limiting different factors such as surface ion concentrations, state of charge, cutoff voltage, and side reaction rate. The designed protocols were implemented and tested in real time using BIL system. Experimental results have shown that the proposed charging method considering the limitations of side reaction rate and ion concentration can reduce about half of the charging time compared with 1C CC/CV normal charging method recommended by manufacturer while the degradation remains comparably.

In addition, the ROM was simplified to a ROM-P2D+SPM that considers several particles in the anode, but a single particle in the cathode, which allows for integration of effects of side reactions and lithium plating. Optimization of the charging time and degradation at a constant temperature was performed by solving the optimal control problem in one sampling time. Since the ROM is strongly nonlinear, NMPC was used to decide the optimal charging current with respect to charging time and side reaction rate with different weighting factors. In addition, the ion loss caused by lithium plating at high charging current were reduced by adding pulse discharging currents to the FC protocols, which promotes the lithium stripping. Consequently, the capacity loss becomes less and cycle life is extended.

In order to further reduce the degradation rate, the temperature effects on side reaction, lithium plating/stripping were investigated using the validated model. Analysis has shown that there is an optimal temperature with the longest cycling life at each charging C-rate. Variation of temperature at different C-rates can further reduce side reaction and lithium plating rate, which results in the extension of cycling life of LiB. The method was verified in the BIL system, where the temperature was controlled by a designed thermostat system to track the optimal temperatures. The experimental results have shown that the designed protocol can further reduce the capacity fade while the charging time can be maintained as before.

Future work will include fundamental exploration of the mechanisms between the frequency and amplitude of the pulse current and the associated lithium plating/stripping, and the relationship between charging protocol and other degradation mechanisms, e.g. mechanical stress and strain. In addition, the working performances of cooling system of battery pack should be considered in order to further optimize the FC method in real time applications. Since the battery pack has a large thermal capacity, feasibility of a real cooling system should be examined.

References

[1] US Electric Vehicle Sales Increased by 81% in 2018 | Greentech Media, (n.d.). https://www.greentechmedia.com/articles/read/us-electric-vehicle-sales-increase-by-81-in-2018#gs.xe9wqp (accessed August 21, 2019).

[2] R. Fu, Modeling, Validation and Analysis of Degradation Processes of Lithium Ion Polymer Batteries, 2014.

[3] X. Li, M. Xiao, S.-Y. Choe, Electrochimica Acta Reduced order model (ROM) of a pouch type lithium polymer battery based on electrochemical thermal principles for real time applications, Electrochim. Acta. 97 (2013) 66–78. doi:10.1016/j.electacta.2013.02.134.

[4] N. Nitta, F. Wu, J.T. Lee, G. Yushin, Li-ion battery materials: present and future, Mater. Today. 18 (2015) 252–264. doi:10.1016/j.mattod.2014.10.040.

[5] A. Du Pasquier, I. Plitz, S. Menocal, G. Amatucci, A comparative study of Li-ion battery, supercapacitor and nonaqueous asymmetric hybrid devices for automotive applications, J. Power Sources. 115 (2003) 171–178. doi:10.1016/S0378-7753(02)00718-8.

[6] X. Feng, M. Ouyang, X. Liu, L. Lu, Y. Xia, X. He, Thermal runaway mechanism of lithium ion battery for electric vehicles: A review, Energy Storage Mater. 10 (2018) 246–267. doi:10.1016/j.ensm.2017.05.013.

[7] M. Gu, I. Belharouak, J. Zheng, H. Wu, J. Xiao, A. Genc, K. Amine, S. Thevuthasan, D.R. Baer, J.-G. Zhang, N.D. Browning, J. Liu, C. Wang, Formation of the Spinel Phase in the Layered Composite Cathode Used in Li-Ion Batteries, ACS Nano. 07 (2013) 760–767. doi:10.1021/nn305065u.

[8] I. Bloom, S.A. Jones, V.S. Battaglia, G.L. Henriksen, J.P. Christophersen, R.B. Wright, C.D. Ho, J.R. Belt, C.G. Motloch, Effect of cathode composition on capacity fade, impedance rise and power fade in high-power, lithium-ion cells, J. Power Sources. 124 (2003) 538–550. doi:10.1016/S0378-7753(03)00806-1.

[9] S.I. Nishimura, G. Kobayashi, K. Ohoyama, R. Kanno, M. Yashima, A. Yamada, Experimental visualization of lithium diffusion in LixFePO 4, Nat. Mater. 7 (2008) 707. doi:10.1038/nmat2251.

[10] Y.K. Sun, S.T. Myung, B.C. Park, J. Prakash, I. Belharouak, K. Amine, High-energy cathode material for long-life and safe lithium batteries, Nat. Mater. 8 (2009) 320–324. doi:10.1038/nmat2418.

[11] M. Xiao, Quasi 3D electrochemical and thermal modeling of lithium ion polymer battery in time and frequency domain and its validation, 2013.

[12] Pump up the Charge with Extreme Fast Charging | Department of Energy, (n.d.). https://www.energy.gov/eere/articles/pump-charge-extreme-fast-charging (accessed August 21, 2019).

[13] S.S. Zhang, The effect of the charging protocol on the cycle life of a Li-ion battery, J. Power Sources. 161 (2006) 1385–1391. doi:10.1016/j.jpowsour.2006.06.040.

[14] J.S. Moon, J.H. Lee, I.Y. Ha, T.K. Lee, C.Y. Won, An efficient battery charging algorithm based on state-of-charge estimation for electric vehicle, in: 2011 Int. Conf. Electr. Mach. Syst., IEEE, 2011: pp. 1–6. doi:10.1109/ICEMS.2011.6073783.

[15] W. Tiezhou, C. Quan, L. Lunan, X. Qing, W. Xieyang, Research on the fast charging of VRLA, TELKOMNIKA Indones. J. Electr. Eng. 10 (2012) 1660–1666. doi:10.11591/telkomnika.v10i7.1560.

[16] T.T. Vo, X. Chen, W. Shen, A. Kapoor, New charging strategy for lithium-ion batteries based on the integration of Taguchi method and state of charge estimation, J. Power Sources. 273 (2015) 413–422. doi:10.1016/j.jpowsour.2014.09.108.

[17] T.C. Hung, S.J. Huang, F.S. Pai, C.W. Ku, Design of lithium-ion battery charging system enhanced with wolf pack algorithm, in: Proc. - 3rd Int. Conf. Innov. Bio-Inspired Comput. Appl. IBICA 2012, 2012: pp. 195–200. doi:10.1109/IBICA.2012.63.

[18] C. Zhang, J. Jiang, Y. Gao, W. Zhang, Q. Liu, X. Hu, Charging optimization in lithium-ion batteries based on temperature rise and charge time, Appl. Energy. 194 (2017) 569–577. doi:10.1016/j.apenergy.2016.10.059.

[19] B.J. Huang, P.C. Hsu, M.S. Wu, P.Y. Ho, System dynamic model and charging control of lead-acid battery for stand-alone solar PV system, Sol. Energy. 84 (2010) 822–830. doi:10.1016/j.solener.2010.02.007.

[20] M. Doyle, J. Newman, The use of mathematical modeling in the design of lithium/polymer battery systems, Electrochim. Acta. 40 (1995) 2191–2196. doi:10.1016/0013-4686(95)00162-8.

[21] R. Klein, N.A. Chaturvedi, J. Christensen, J. Ahmed, R. Findeisen, A. Kojic, Optimal charging strategies in lithium-ion battery, in: Am. Control Conf., Institute of Electrical and Electronics Engineers (IEEE), 2011: pp. 382–387. doi:10.1109/acc.2011.5991497.

[22] K.A. Smith, C.D. Rahn, C.Y. Wang, Control oriented 1D electrochemical model of lithium ion battery, Energy Convers. Manag. 48 (2007) 2565–2578. doi:10.1016/j.enconman.2007.03.015.

[23] J. Li, N. Lotfi, R.G. Landers, J. Park, A single particle model for lithium-ion batteries with electrolyte and stress-enhanced diffusion physics, J. Electrochem. Soc. 164 (2017) A874–

A883. doi:10.1149/2.1541704jes.

[24] S.K. Rahimian, S.C. Rayman, R.E. White, Maximizing the life of a lithium-ion cell by optimization of charging rates, J. Electrochem. Soc. 157 (2010) A1302–A1308. doi:10.1149/1.3491367.

[25] J. Liu, G. Li, H.K. Fathy, A Computationally Efficient Approach for Optimizing Lithium-Ion Battery Charging, J. Dyn. Syst. Meas. Control. Trans. ASME. 138 (2016) 1–8. doi:10.1115/1.4032066.

[26] S. Pramanik, S. Anwar, Electrochemical model based charge optimization for lithium-ion batteries, J. Power Sources. 313 (2016) 164–177. doi:10.1016/j.jpowsour.2016.01.096.

[27] Z. Chu, X. Feng, L. Lu, J. Li, X. Han, M. Ouyang, Non-destructive fast charging algorithm of lithium-ion batteries based on the control-oriented electrochemical model, Appl. Energy. 204 (2017) 1240–1250. doi:10.1016/j.apenergy.2017.03.111.

[28] R. Fu, S.Y. Choe, V. Agubra, J. Fergus, Development of a physics-based degradation model for lithium ion polymer batteries considering side reactions, J. Power Sources. 278 (2015) 506–521. doi:10.1016/j.jpowsour.2014.12.059.

[29] D. Aurbach, M.D. Levi, E. Levi, A. Schechter, Failure and stabilization mechanisms of graphite electrodes, J. Phys. Chem. B. 101 (1997) 2195–2206. doi:10.1021/jp962815t.

[30] X.G. Yang, Y. Leng, G. Zhang, S. Ge, C.Y. Wang, Modeling of lithium plating induced aging of lithium-ion batteries: Transition from linear to nonlinear aging, J. Power Sources. 360 (2017) 28–40. doi:10.1016/j.jpowsour.2017.05.110.

[31] H. Ge, T. Aoki, N. Ikeda, S. Suga, T. Isobe, Z. Li, Y. Tabuchi, J. Zhang, Investigating Lithium Plating in Lithium-Ion Batteries at Low Temperatures Using Electrochemical Model with NMR Assisted Parameterization, J. Electrochem. Soc. 164 (2017) 1050–1060.

doi:10.1149/2.0461706jes.

[32] W. Lu, C.M. López, N. Liu, J.T. Vaughey, A. Jansen, D.W. Dees, Overcharge effect on morphology and structure of carbon electrodes for lithium-ion batteries, J. Electrochem. Soc. 159 (2012) A566–A570. doi:10.1149/2.jes035205.

[33] R. Fu, S.Y. Choe, V. Agubra, J. Fergus, Development of a physics-based degradation model for lithium ion polymer batteries considering side reactions, J. Power Sources. 278 (2015) 506–521. doi:10.1016/j.jpowsour.2014.12.059.

[34] P. Verma, P. Maire, P. Novák, A review of the features and analyses of the solid electrolyte interphase in Li-ion batteries, Electrochim. Acta. 55 (2010) 6332–6341. doi:10.1016/j.electacta.2010.05.072.

[35] G. Sikha, B.N. Popov, R.E. White, Effect of Porosity on the Capacity Fade of a Lithium-Ion Battery, J. Electrochem. Soc. 151 (2004) A1104–A1114. doi:10.1149/1.1759972.

[36] P. Ramadass, B. Haran, P.M. Gomadam, R. White, B.N. Popov, Development of First Principles Capacity Fade Model for Li-Ion Cells, J. Electrochem. Soc. 151 (2004) A196–A203. doi:10.1149/1.1634273.

[37] H.J. Ploehn, P. Ramadass, R.E. White, Solvent Diffusion Model for aging of Lithium-Ion Battery Cells, J. Electrochem. Soc. 151 (2004) A456–A462. doi:10.1149/1.1644601.

[38] M. Safari, M. Morcrette, A. Teyssot, C. Delacourt, Multimodal physics-based aging model for life prediction of Li-Ion batteries, J. Electrochem. Soc. 156 (2009) A145–A153. doi:10.1149/1.3043429.

[39] Y. Zhao, S.Y. Choe, J. Kee, Modeling of degradation effects and its integration into electrochemical reduced order model for Li(MnNiCo)O2/Graphite polymer battery for real time applications, Electrochim. Acta. 270 (2018) 440–452.

doi:10.1016/j.electacta.2018.02.086.

[40] M.B. Pinsona, M.Z. Bazant, Theory of SEI formation in rechargeable batteries: Capacity fade, accelerated aging and lifetime prediction, J. Electrochem. Soc. 160 (2013) A243–A250. doi:10.1149/2.044302jes.

[41] Xueyan Li, Song-Yul Choe, State-of-charge (SOC) estimation based on a reduced order electrochemical thermal model and extended Kalman filter, in: 2013 Am. Control Conf., 2013: pp. 1100–1105. doi:10.1109/acc.2013.6579983.

[42] K.D. Stetzel, L.L. Aldrich, M.S. Trimboli, G.L. Plett, Electrochemical state and internal variables estimation using a reduced-order physics-based model of a lithium-ion cell and an extended Kalman filter, J. Power Sources. 278 (2015) 490–505. doi:10.1016/j.jpowsour.2014.11.135.

[43] X. Li, M. Xiao, S.Y. Choe, Reduced order model (ROM) of a pouch type lithium polymer battery based on electrochemical thermal principles for real time applications, Electrochim. Acta. 97 (2013) 66–78. doi:10.1016/j.electacta.2013.02.134.

[44] Y. Yin, Z. Zheng, S.-Y. Choe, Design of a Calorimeter for Measurement of Heat Generation Rate of Lithium Ion Battery Using Thermoelectric Device, SAE Int. J. Altern. Powertrains. 6 (2017) 252–260. doi:10.4271/2017-01-1213.

[45] D. Anseán, M. González, J.C. Viera, V.M. García, C. Blanco, M. Valledor, Fast charging technique for high power lithium iron phosphate batteries: A cycle life analysis, J. Power Sources. 239 (2013) 9–15. doi:10.1016/j.jpowsour.2013.03.044.

[46] T. Ikeya, N. Sawada, J. Murakami, K. Kobayashi, M. Hattori, N. Murotani, S. Ujiie, K. Kajiyama, H. Nasu, H. Narisoko, Y. Tomaki, K. Adachi, Y. Mita, K. Ishihara, Multi-step constant-current charging method for an electric vehicle nickel/metal hydride battery with

high-energy efficiency and long cycle life, J. Power Sources. 105 (2002) 6–12. doi:10.1016/S0378-7753(01)00907-7.

[47] Z. Ullah, B. Burford, S. Dillip, Fast intelligent battery charging: neural-fuzzy approach, IEEE Aerosp. Electron. Syst. Mag. 11 (1996) 26–34.

[48] Y.H. Liu, Y.F. Luo, Search for an optimal rapid-charging pattern for li-ion batteries using the Taguchi approach, IEEE Trans. Ind. Electron. 57 (2010) 3963–3971. doi:10.1109/TIE.2009.2036020.

[49] W. Li, D. Huang, D. Feng, D. Dai, F. Lin, The research on lithium-ion battery's rapid charging strategy with ant-cycle system, in: 2012 IEEE Int. Conf. Mechatronics Autom. ICMA 2012, 2012: pp. 2170–2174. doi:10.1109/ICMA.2012.6285679.

[50] H.E. Perez, S. Dey, X. Hu, S.J. Moura, Optimal charging of Li-ion batteries via a single particle model with electrolyte and thermal dynamics, J. Electrochem. Soc. 164 (2017) A1679–A1687. doi:10.1149/2.1301707jes.

[51] X. Lin, X. Hao, Z. Liu, W. Jia, Health conscious fast charging of Li-ion batteries via a single particle model with aging mechanisms, J. Power Sources. 400 (2018) 305–316. doi:10.1016/j.jpowsour.2018.08.030.

[52] A. Pozzi, M. Torchio, D.M. Raimondo, Film growth minimization in a Li-ion cell: A Pseudo Two Dimensional model-based optimal charging approach, in: 2018 Eur. Control Conf. ECC 2018, Institute of Electrical and Electronics Engineers Inc., 2018: pp. 1753–1758. doi:10.23919/ECC.2018.8550404.

[53] M.A. Xavier, M.S. Trimboli, Lithium-ion battery cell-level control using constrained model predictive control and equivalent circuit models, J. Power Sources. 285 (2015) 374–384. doi:10.1016/j.jpowsour.2015.03.074.

[54] J. Liu, G. Li, H.K. Fathy, An Extended Differential Flatness Approach for the Health-Conscious Nonlinear Model Predictive Control of Lithium-Ion Batteries, IEEE Trans. Control Syst. Technol. 25 (2017) 1882–1889. doi:10.1109/TCST.2016.2624143.

[55] C. Zou, X. Hu, Z. Wei, T. Wik, B. Egardt, Electrochemical Estimation and Control for Lithium-Ion Battery Health-Aware Fast Charging, IEEE Trans. Ind. Electron. 65 (2018) 6635–6645. doi:10.1109/TIE.2017.2772154.

[56] S. Lucia, M. Torchio, D.M. Raimondo, R. Klein, R.D. Braatz, R. Findeisen, Towards adaptive health-aware charging of Li-ion batteries: A real-time predictive control approach using first-principles models, in: Am. Control Conf., Institute of Electrical and Electronics Engineers Inc., 2017: pp. 4717–4722. doi:10.23919/ACC.2017.7963684.

[57] M.Z. Mayers, J.W. Kaminski, T.F. Miller, Suppression of dendrite formation via pulse charging in rechargeable lithium metal batteries, J. Phys. Chem. C. 116 (2012) 26214–26221. doi:10.1021/jp309321w.

[58] M. Song, S.-Y. Choe, Fast and safe charging method suppressing side reaction and lithium deposition reaction in lithium ion battery, J. Power Sources. 436 (2019) 226835. doi:10.1016/j.jpowsour.2019.226835.

[59] Y. Zhao, S.-Y. Choe, A highly efficient reduced order electrochemical model for a large format LiMn2O4/Carbon polymer battery for real time applications, Electrochim. Acta. 164 (2015) 97–107. doi:10.1016/j.electacta.2015.02.182.

[60] H. Ge, T. Aoki, N. Ikeda, S. Suga, T. Isobe, Z. Li, Y. Tabuchi, J. Zhang, Investigating Lithium Plating in Lithium-Ion Batteries at Low Temperatures Using Electrochemical Model with NMR Assisted Parameterization, J. Electrochem. Soc. 164 (2017) A1050–A1060. doi:10.1149/2.0461706jes.

[61] P. Arora, Mathematical Modeling of the Lithium Deposition Overcharge Reaction in Lithium-Ion Batteries Using Carbon-Based Negative Electrodes, J. Electrochem. Soc. 146 (1999) 3543. doi:10.1149/1.1392512.

[62] X. Zhao, Y. Yin, Y. Hu, S.-Y. Choe, Electrochemical-thermal modeling of lithium plating/stripping of Li(Ni0.6Mn0.2Co0.2)O2/Carbon lithium-ion batteries at subzero ambient temperatures, J. Power Sources. 418 (2019) 61–73. doi:10.1016/j.jpowsour.2019.02.001.

[63] X. Zhao, Y. Yin, Y. Hu, S.Y. Choe, Electrochemical-thermal modeling of lithium plating/stripping of Li(Ni 0.6 Mn 0.2 Co 0.2)O 2 /Carbon lithium-ion batteries at subzero ambient temperatures, J. Power Sources. (2019). doi:10.1016/j.jpowsour.2019.02.001.

[64] Y. Bi, S.-Y. Choe, An adaptive sigma-point Kalman filter with state equality constraints for online state-of-charge estimation of a Li(NiMnCo)O2/Carbon battery using a reduced-order electrochemical model, Appl. Energy. 258 (2020) 113925. doi:10.1016/j.apenergy.2019.113925.

[65] L. Grüne, J. Pannek, Nonlinear model predictive control, Springer, 2017. doi:10.1007/978-0-85729-501-9.

[66] Y. Yin, Y. Hu, S.Y. Choe, H. Cho, W.T. Joe, New fast charging method of lithium-ion batteries based on a reduced order electrochemical model considering side reaction, J. Power Sources. 423 (2019) 367–379. doi:10.1016/j.jpowsour.2019.03.007.

[67] Z. Liu, F. Forouzanfar, Y. Zhao, Comparison of SQP and AL algorithms for deterministic constrained production optimization of hydrocarbon reservoirs, J. Pet. Sci. Eng. 171 (2018) 542–557. doi:10.1016/j.petrol.2018.06.063.

[68] M. Abdel Monem, K. Trad, N. Omar, O. Hegazy, B. Mantels, G. Mulder, P. Van den

Bossche, J. Van Mierlo, Lithium-ion batteries: Evaluation study of different charging methodologies based on aging process, Appl. Energy. 152 (2015) 143–155. doi:10.1016/j.apenergy.2015.02.064.

[69] J. Marcicki, A.T. Conlisk, G. Rizzoni, A lithium-ion battery model including electrical double layer effects, J. Power Sources. 251 (2014) 157–169. doi:10.1016/j.jpowsour.2013.11.001.

[70] Q. Liu, C. Du, B. Shen, P. Zuo, X. Cheng, Y. Ma, G. Yin, Y. Gao, Understanding undesirable anode lithium plating issues in lithium-ion batteries, RSC Adv. 6 (2016) 88683–88700. doi:10.1039/c6ra19482f.

[71] W. Diao, S. Saxena, M. Pecht, Accelerated cycle life testing and capacity degradation modeling of LiCoO2-graphite cells, J. Power Sources. 435 (2019) 226830. doi:10.1016/j.jpowsour.2019.226830.

[72] T. Waldmann, M. Wilka, M. Kasper, M. Fleischhammer, M. Wohlfahrt-Mehrens, Temperature dependent ageing mechanisms in Lithium-ion batteries - A Post-Mortem study, J. Power Sources. 262 (2014) 129–135. doi:10.1016/j.jpowsour.2014.03.112.

[73] T. Matsuda, M. Myojin, K. Ando, D. Imamura, Degradation Analyses of Commercial Lithium-Ion Cells by Temperature/C-rate Controlled Cycle Test, (n.d.). doi:10.1149/06422.0069ecst.

[74] H.E. Perez, X. Hu, S.J. Moura, Optimal charging of batteries via a single particle model with electrolyte and thermal dynamics, in: Proc. Am. Control Conf., Institute of Electrical and Electronics Engineers Inc., 2016: pp. 4000–4005. doi:10.1109/ACC.2016.7525538.

[75] X.G. Yang, C.Y. Wang, Understanding the trilemma of fast charging, energy density and cycle life of lithium-ion batteries, J. Power Sources. 402 (2018) 489–498.

doi:10.1016/j.jpowsour.2018.09.069.

[76] X. Zhao, Y. Yin, Y. Hu, S.Y. Choe, Electrochemical-thermal modeling of lithium plating/stripping of Li(Ni 0.6 Mn 0.2 Co 0.2)O 2 /Carbon lithium-ion batteries at subzero ambient temperatures, J. Power Sources. 418 (2019) 61–73. doi:10.1016/j.jpowsour.2019.02.001.

[77] A. Pesaran, A. Vlahinos, T. Stuart, Cooling and Preheating of Batteries in Hybrid Electric Vehicles, n.d. http://www.ctts.nrel.gov/BTM. (accessed November 11, 2019).

[78] T.C. Bach, S.F. Schuster, E. Fleder, J. Müller, M.J. Brand, H. Lorrmann, A. Jossen, G. Sextl, Nonlinear aging of cylindrical lithium-ion cells linked to heterogeneous compression, J. Energy Storage. 5 (2016) 212–223. doi:10.1016/j.est.2016.01.003.

[79] B. Rieger, S. Schlueter, S. V. Erhard, J. Schmalz, G. Reinhart, A. Jossen, Multi-scale investigation of thickness changes in a commercial pouch type lithium-ion battery, J. Energy Storage. 6 (2016) 213–221. doi:10.1016/j.est.2016.01.006.